

Conformal Antenna-Based Wireless Telemetry System for Capsule Endoscopy

Julia Faerber

A thesis submitted for the degree of Doctor of Philosophy

Heriot-Watt University

School of Engineering and Physical Sciences

February 2018

The copyright in this thesis is owned by the author. Any quotation from the thesis or use of any of the information contained in it must acknowledge this thesis as the source of the quotation or information.

ABSTRACT

Capsule endoscopy for imaging the gastrointestinal tract is an innovative tool for carrying out medical diagnosis and therapy. Additional modalities beyond optical imaging would enhance current capabilities at the expense of denser integration, due to the limited space available within the capsule. We therefore need new designs and technologies to increase the smartness of the capsules for a given volume.

This thesis presents the design, manufacture and performance characterisation of a helical antenna placed conformally outside an endoscopic capsule, and the characterisation *in-silico*, *in-vitro* and *in-vivo* of the telemetry system in alive and euthanised pigs. This method does not use the internal volume of the capsule, but does use an extra coating to protect the antenna from the surrounding tissue and maintain biocompatibility for safe use inside the human body. The helical antenna, radiating at 433 MHz with a bandwidth of 20 MHz within a muscle-type tissue, presents a low gain and efficiency, which is typical for implantable and ingestible medical devices.

Telemetry capsule prototypes were simulated, manufactured and assembled with the necessary internal electronics, including a commercially available transceiver unit. Thermistors were embedded into each capsule shell, to record any temperature increase in the tissue surrounding the antenna during the experiments. A temperature increase of less than 1°C was detected for the tissue surrounding the antenna. The process of coating the biocompatible insulation layer over the full length of the capsule is described in detail. Data transmission programmes were established to send programmed data packets to an external receiver. The prototypes radiated at different power levels ranging from -10 to 10 dBm, and all capsules demonstrated a satisfactory performance at a data rate of 16 kbps during phantom and *in-vivo* experiments. Data transmission was achieved with low bit-error rates below 10^{-5} . A low signal strength of only -54 dBm still provided effective data transfer, irrespective of the orientation and location of the capsule, and this successfully demonstrated the feasibility of the system.

ACKNOWLEDGEMENTS

The completion of this thesis is not only the result of hard work, determination and some nervous breakdowns, but also due to the great support of colleagues, family and friends. The process of finishing this PhD has been a life changing experience and would not have been possible without the support of my supervisor, Professor Marc Desmulliez. I would like to thank him for his expert advice and support all the way through this PhD and for giving me the freedom for my way of working and pointing me into the right direction when needed.

I would like to thank my second supervisor Dr Paul Record for his mentoring and valuable technical advice.

My sincere thanks go to Dr Gerard Cummins, who deserves a medal for, despite already having a stressfully large work load, helping me to reach my goals and deadlines. His advice and scientific expertise are invaluable and I cannot thank him enough. I would also like to thank him for increasing my tolerance to high stress levels.

Special thanks go to Dr Sumanth K. Pavuluri for helping me throughout the course of the PhD, especially when it came to the manufacturing stage.

My particular gratitude goes to Maria who, although very busy herself, introduced me to the theory of antennas and simulations and patiently answered every single question I asked. Thanks are also extended to Dave, my cheeky desk neighbour, for the fun and serious discussions about donuts and Pascual, for the relaxing and never-ending lunches. For keeping me from total meltdowns and giving me some happy moments of normality over a tea and coffee, I would like to deeply thank the whole office EM 2.34 of PhD and Postgraduate students, especially the Spanish crew. I really enjoyed the banter and the solidarity and I am really going to miss the lunch breaks.

Special thanks go to the technicians in the electronic workshop for providing me with their technical expertise, a workplace and the tools for assembling my devices.

Huge thanks and big hugs also go to Lynn and Audrey, the heart and soul of the institute, who provided me always with a happy chat and help with all the event and travel bookings.

And I would like to thank the whole Sonopill Team for the constructive feedback, especially Professor Sandy Cochran for supporting this research and for giving me the opportunity to experience being part of such a big project.

I am grateful to my close friends Mela and Kiki, for being there, when I needed them and their understanding, when not hearing from me for weeks. Special thanks to my friends Helen, Markus, Stuart, Jan and Caro for the happy times spent at BBQs and dinners, helping me to relax in this stressful time.

This thesis would not have been finished without the patience, love and support of my long-term fiancé and best friend Keith. You helped me to get through this difficult process and to stay sane and motivated, especially during the low-points of the work. I will always be grateful for this.

Finally, my sincere appreciation goes to my family for their love and support despite the distance and my late grandmothers for watching over me all this time. I would like to thank my mum and dad, for their pride and trust in me. They were there, when I needed them and always had a calming word when nothing else helped.

Julia Faerber
February 2018

ACADEMIC REGISTRY

Research Thesis Submission

Name:			
School:			
Version: <i>(i.e. First, Resubmission, Final)</i>		Degree Sought:	

Declaration

In accordance with the appropriate regulations I hereby submit my thesis and I declare that:

- 1) the thesis embodies the results of my own work and has been composed by myself
- 2) where appropriate, I have made acknowledgement of the work of others and have made reference to work carried out in collaboration with other persons
- 3) the thesis is the correct version of the thesis for submission and is the same version as any electronic versions submitted*.
- 4) my thesis for the award referred to, deposited in the Heriot-Watt University Library, should be made available for loan or photocopying and be available via the Institutional Repository, subject to such conditions as the Librarian may require
- 5) I understand that as a student of the University I am required to abide by the Regulations of the University and to conform to its discipline.
- 6) I confirm that the thesis has been verified against plagiarism via an approved plagiarism detection application e.g. Turnitin.

* *Please note that it is the responsibility of the candidate to ensure that the correct version of the thesis is submitted.*

Signature of Candidate:		Date:	
-------------------------	--	-------	--

Submission

Submitted By <i>(name in capitals)</i> :	
Signature of Individual Submitting:	
Date Submitted:	

For Completion in the Student Service Centre (SSC)

Received in the SSC by <i>(name in capitals)</i> :			
<i>Method of Submission</i> <i>(Handed in to SSC; posted through internal/external mail):</i>			
<i>E-thesis Submitted (mandatory for final theses)</i>			
Signature:		Date:	

DECLARATION

I hereby declare that the work presented in this thesis was carried out by myself at Heriot-Watt University, Edinburgh, and has not been submitted for any other degree, at this, or any other university.

Julia Faerber
15th February 2018

TABLE OF CONTENTS

ABSTRACT	i
ACKNOWLEDGEMENTS	ii
DECLARATION	v
TABLE OF CONTENTS	vi
LIST OF FIGURES	x
LIST OF TABLES	xv
LIST OF ACRONYMS	xvi
LIST OF PUBLICATIONS BY THE CANDIDATE	xvii
CHAPTER 1 INTRODUCTION	1
1.1 Design elements	2
1.2 Thesis outlook	4
CHAPTER 2 LITERATURE REVIEW	6
2.1 Applications of ingestible medical devices	6
2.1.1 Ingestible MDs – Endoscopic capsules	6
2.1.1.1 Power	8
2.1.1.2 Imaging sensor technology	10
2.1.1.3 Image compression	10
2.1.1.4 Modalities	11
2.1.1.5 Locomotion systems	11
2.1.1.6 Localisation	12
2.1.1.7 Telemetry	12
2.1.2 Summary	13
2.2 Telemetry in implantable/ingestible devices	14
2.2.1 Frequency bands	14
2.2.2 Wireless telemetry in capsule endoscopy	15
2.2.2.1 Telemetry system requirements	16
2.2.2.2 ASIC design	16
2.3 Antennas in wireless capsule endoscopy	17
2.3.1 Antenna design process	19
2.3.2 Small, conformal antenna designs – state-of-the-art	21

2.3.3	Antenna fabrication	26
2.3.4	The helix	30
2.4	Summary	31
CHAPTER 3 CRITICAL PARAMETERS FOR THE CHARACTERISATION OF ANTENNAS IN THE HUMAN BODY		32
3.1	Constitutive material parameters: permittivity, permeability and conductivity	32
3.2	Near- and far-field	36
3.3	Radiation power, efficiency, gain, directivity	38
3.4	Radiation pattern	39
3.5	Bandwidth and quality factor	40
3.6	Specific absorption rate (SAR)	41
3.7	Insulation layers	45
3.8	Challenges/ limitations of ingestible antennas	45
3.9	Human body models	46
3.9.1	Geometry, composition and dimension	48
3.10	Conclusion	49
CHAPTER 4 ANTENNA SIMULATION		51
4.1	Antenna development	52
4.1.1	Initial conformal antenna design, simulation and measurements in free space	52
4.1.2	Human body phantom material	55
4.1.3	Optimised conformal antenna designs within lossy phantom material	56
4.1.3.1	Simulation and measurement	58
4.1.3.2	Cable effect	61
4.1.3.3	Summary of the antenna development	62
4.2	Final helix antenna design	63
4.2.1	Simulation set-up and optimisation	64
4.2.2	Simulation results	65
4.2.2.1	SAR	68
4.2.3	Summary	69
CHAPTER 5 PACKAGING		71
5.1	Telemetry system assembly	72

5.1.1	Transceiver	73
5.1.2	PCB design	75
5.1.2.1	Circuit assembly	76
5.1.2.2	Interconnection to User Interface	80
5.1.3	Base station	81
5.1.4	Programming	82
5.1.4.1	Thermistors	84
5.2	Insulation layer	86
5.2.1	Biocompatible coating – moulding process	86
5.3	Summary	89
CHAPTER 6 IN-VITRO EVALUATION		90
6.1	Phantom characterisation	90
6.1.1	<i>In-vitro</i> test set-up	91
6.2	Measurements	92
6.2.1	Data transmission set up	93
6.2.2	Distance measurements	94
6.2.3	Radiation pattern	95
6.3	Results and discussion	96
6.3.1	Data transmission	96
6.3.2	Distance	97
6.3.3	Radiation pattern	98
6.3.4	SAR/Temperature measurements	99
6.5	Summary	100
CHAPTER 7 IN-VIVO CHARACTERISATION		101
7.1	Pig preparation and trial procedure	102
7.1.1	Static power – Group I	103
7.1.2	Variable power – Group II	106
7.2	Results and discussion	106
7.2.1	Static power – Group I	106
7.2.1.1	Living pigs	109
7.2.1.2	Post-mortem pigs	110
7.2.1.3	Living and post-mortem pig comparison	110
7.2.1.4	Summary of static power level experiments	111
7.2.2	Variable power – Group II	112

7.2.2.1	Live pigs	114
7.2.2.2	Post-mortem pigs	115
7.2.2.3	Temperature measurements	115
7.2.2.4	Summary	116
7.3	Conclusions	117
7.3.1	Polarisation and radiation pattern	117
CHAPTER 8 CONCLUSIONS AND FUTURE WORK		119
8.1	Conclusions	119
8.2	Novel contributions	122
8.3	Future work	124
APPENDIX		126
A1	Link-budget analysis	126
REFERENCES		130

LIST OF FIGURES

Figure 1.1	Overview of the elements involved in the design of ingestible telemetry systems.....	2
Figure 2.1	Some commercially available endoscopic capsules: a) PillCam®SB3 (Given Imaging); b) PillCam®COLON2 (Given Imaging); c) PillCam®UGI (Given Imaging); d) PillCam®PATENCY (GivenImaging); e) EndoCapsule (Olympus); f) OMOM capsule (Chongqing Jinshan Science & Technology); g) MiroCam (Intromedic); h) CapsoCam (CapsoVision) [21].....	7
Figure 2.2	Top view of the capsules, with corresponding X-ray image. Left to right: PillCam SB2, EndoCapsule, CapsoCam, MiroCam, OMOM capsule, PillCam ESO2, PillCam COLON2 [41].....	13
Figure 2.3	External (left) and internal (middle) views of a PillCam® SB; Internal helix antenna of PillCam® (right)	19
Figure 2.4	Stack-up of a potential Sonopill with a conformal helix antenna.....	19
Figure 2.5	Flow chart of the antenna design process steps [11, 61-65]	20
Figure 2.6	Inductively loaded folded-patch antenna from Cheng <i>et al.</i> [67].....	22
Figure 2.7	Conformal trapezoid strip excited broadband hemispherical dielectric resonator antenna from Wang <i>et al.</i> [68].....	22
Figure 2.8	Outer wall loop antenna for ultra-wideband capsule endoscope system from Yun Sumin <i>et al.</i> [8].....	23
Figure 2.9	A novel chandelier meandered design from Izdebski <i>et al.</i> [65].....	23
Figure 2.10	A new small conformal antenna for capsule endoscopy [7] and a broadband flexible implantable loop antenna with complementary split ring resonators from Alrawashdeh <i>et al.</i> [71]	24
Figure 2.11	An UWB conformal loop antenna for an ingestible capsule endoscope system from Suzan <i>et al.</i> [72]	24
Figure 2.12	Small spiral antenna for a wideband capsule endoscope system by Kwak <i>et al.</i> [73]	25
Figure 2.13	Different types of spiral antennas suggested by Lee <i>et al.</i> [74-76].....	25
Figure 2.14	Multilayer miniaturised and circularly polarised helical antenna Liu <i>et al.</i> [77].....	26

Figure 2.15	Wireless smart sensor with small spiral antenna on Si-substrate [80].....	27
Figure 2.16	Printing of silver nanoparticle inks on curvilinear surface [84]	27
Figure 2.17	Electrically small folded ellipsoidal helix antenna fabricated using selective laser sintering based moulding process [86]....	28
Figure 2.18	Novel methods to analyse and fabricate electrically small antennas: printing metallic traces onto contoured substrates [88].....	29
Figure 2.19	Spherical helix antenna with direct transfer patterning by Pfeiffer <i>et al.</i> [88].....	29
Figure 2.20	Configuration of a helical antenna [90].....	30
Figure 3.1	Change of relative permittivity and conductivity over frequency [13].....	33
Figure 3.2	a) Variation of VSWR over conductivity of tissue; b) Variation of VSWR over permittivity [98].....	34
Figure 3.3	Log-log plot of penetration depth from 100 MHz to 40 GHz of dry skin, infiltrated fat, and muscle by Gabriel's Cole-Cole model [97].....	34
Figure 3.4	Frequency shift of a simulated antenna radiating in free-space versus into a lossless medium [10].....	36
Figure 3.5	Near- and far-field of an antenna.....	36
Figure 3.6	Increase in bandwidth for an antenna radiating into a lossy phantom compared with a lossless phantom [10].....	41
Figure 3.7	SAR over conductivity of tissue [98].....	42
Figure 3.8	Variation of SAR over permittivity [98].....	42
Figure 3.9	The virtual family provided by the IT'IS Foundation [136]....	48
Figure 4.1	a) Meander antenna configuration ($D=0.4$ mm, $W=3.4$ mm, $L=19.6$ mm, $R=0.8$ mm, $S=2.05$ mm); b) Conformal antenna system (CST simulation).....	52
Figure 4.2	Manufactured meander antenna prototype.....	53
Figure 4.3	Frequency response of antenna system in free-space: Simulation and VNA measurements of 5 fabricated antennas numbered 1 to 5	54
Figure 4.4	Radiation pattern, gain, radiation efficiency of meander in free-space simulation.....	55
Figure 4.5	Capsule antenna configurations of the helix (left) and meander (right) (CST simulation) ($D = 0.4$ mm; $H = 3$ mm; $W = 1.8$ mm; $R = 0.8$ mm).....	57

Figure 4.6	Manufactured prototypes (length = 30 mm; diameter = 10 mm) including insulation layer: meander (top); helix (bottom).....	58
Figure 4.7	Antenna configuration in a body phantom simulation and measurement setup. The antenna capsule was covered with a second semi-spherical part of the phantom once placed in the middle of the first half.....	59
Figure 4.8	Frequency response of simulated vs. experimental meander (top) and helix (bottom) antennas in tissue phantom with muscle properties. Each antenna configuration was manufactured 5 times, numbered 1 to 5, together with a coax cable, covered by an insulation layer.....	60
Figure 4.9	SAR simulation of helix (top) and meander (bottom) system, visualising the radiation along the attached cable. The cable is extending the length of the antenna and when removed, the resonance frequency will be higher.....	61
Figure 4.10	Simulation and optimisation process of the final antenna design.....	63
Figure 4.11	Simulation set up of the helix antenna system within a cubic muscle tissue model.....	64
Figure 4.12	Helix S_{11} simulation in free-space.....	65
Figure 4.13	Helix S_{11} simulation result in muscle tissue phantom.....	66
Figure 4.14	Radiation pattern of helix within phantom.....	66
Figure 4.15	Simulated S_{11} comparison of helix antenna in skin, fat, and muscle material as well as the phantom material used. A clear shift in frequencies is visible, which is depending on the surrounding tissue.....	67
Figure 4.16	Full antenna system with connected and disconnected internal GND plane, and the measured resonant frequency of the fabricated prototype within the phantom. When the GND is disconnected from the antenna, losses are increased and resonance frequency shifts.....	67
Figure 4.17	SAR distribution of the simulated antenna system embedded into phantom: max. SAR for 1 g of mass (left) and 10 g of mass (right) with 1 mW output power.....	69

Figure 5.1	Transceiver system design process: a) Simulation of antenna system; b) Selection of system components (transceiver chip and additional electronic components according to reference design, plus antenna and programmable interconnects); c) PCB design of RF and thermistor board with open source programme KiCad Electronic Design Automation (EDA); d) Manufacture of boards and connection of electronic components; e) Attachment of NTC thermistors to the designated holes; f) Linking of boards, NTC circuit and tether connection; g) Antenna assembly, followed by the epoxy and parylene coating process (described in Section 5.2) and the connection to the PC's User Interface (UI).....	71
Figure 5.2	Two internal PCBs were manufactured: RF board (left) has the MCU and transmission line embedded and the thermistor board (right) connects to the power supply and the on-board thermistors.....	72
Figure 5.3	Computer model of the 3D printed capsule shell.....	73
Figure 5.4	CC1310 RHB (5-mm × 5-mm) pinout, 0.5-mm pitch [152]....	74
Figure 5.5	System schematic of both PCB boards (left); manufactured and assembled PCB boards (right).....	76
Figure 5.6	Schematic of the circuit design for the CC1310 MCU	78
Figure 5.7	Interconnections of both PCBs and tether connections.....	79
Figure 5.8	Antenna connection via a micro SMA cable.....	80
Figure 5.9	Connection of capsule system via an adapter to the NI myRIO	81
Figure 5.10	Base station module.....	82
Figure 5.11	Programmer cable (top) and XDS100v3 debugger and emulator (bottom).....	83
Figure 5.12	Thermistor assembly inside capsule shell.....	84
Figure 5.13	LabVIEW UI for monitoring the temperature measured by the on-board thermistors.....	85
Figure 6.1	a) One semi-spherical mould with stamp placed on top; b) Stamp sheet; c) Imprinted phantom part; d) Finished phantom set-up.....	91

Figure 6.2	Experimental trolley set-up of the Tx/Rx system: The Rx is connected via an USB cable to the laptop and controlled through the SmartRF studio software from Labview, which records the received data packets. The capsule prototypes are connected to the adapter, which is connected to the NI myRIO. The NI myRIO supplies the power to the capsules and is controlled by the developed Labview UI, which is also monitoring the temperature data [154].....	92
Figure 6.3	Trolley set-up in anechoic chamber: The phantom with embedded prototypes and the Rx base station is placed on a chair behind the absorber. The laptop is placed on a trolley on the other side.....	93
Figure 6.4	Group I data transmission shows a steady signal strength.....	94
Figure 6.5	Signal strength of Group II with gradually increasing power output.....	94
Figure 6.6	Decreasing RSSI over increasing separation distance, with Group I capsules having a transmit power of 0 dBm and Group II capsules -10 dBm.....	95
Figure 6.7	Radiation pattern for Group I capsules (top) and Group II capsules (bottom). An average of the measured RSSI of each capsule group was taken in horizontal (H) and vertical (V) plane.....	96
Figure 6.8	Screenshot of the data (left) and temperature measurement UI (right): a) Thee textbox shows the received data packets, b) BER and PER data, c) visualisation of the temperature monitor.....	100
Figure 7.1	Porcine trial set-up - capsule (Tx) inserted via the created stoma; Rx, laptop for data recording and TI adapter placed on trolley next to pig.....	102
Figure 7.2	Pig set-up at the start of the experiments – The capsules are inserted and the distance markers next to the stoma and tape marker on the tubing to allow for a more repeatable withdrawal rate.....	104
Figure 7.3	Visualisation of the different distances involved in the measurements: The insertion depth shows how far the capsule is inserted; the distance from Rx to stoma is steady (PM1 = 55 cm, PigX = 62 cm, PigY/PM2 = 70 cm); the distance between Tx ad Rx is determined by the location of the capsule inside the pigs' body.....	104
Figure 7.4	Ultrasound image of capsule inserted in the small bowel and its surrounding body tissue layers.....	105

Figure 7.5	Endoscopy image of capsule within the small bowel of PM2...	105
Figure 7.6	RSSI of two Group I capsules (two insertions each) in both living pigs (PigX and PigY).....	108
Figure 7.7	RSSI of two Group I capsules (two insertions each) in both euthanised pigs (PM1 and PM2).....	108
Figure 7.8	Comparison of RSSI of two Group I capsules (two insertions each) in PM2 and PigY.....	108
Figure 7.9	Removed section of the small bowel of PigX that was in contact with the transmitting capsules.....	111
Figure 7.10	RSSI of two Group II capsules in both living pigs (PigX and PigY).....	113
Figure 7.11	RSSI of two Group II capsules in both euthanised pigs (PM1 and PM2).....	113
Figure 7.12	RSSI of two Group II capsules in PM2 and PigY (same pig)...	113
Figure 7.13	Signal strength indicator for each power level with an approximated slope value for each curve.....	114
Figure 7.14	Measured temperature of the four on-board thermistors (A-D) over the full power increase cycle of each insertion into the live pigs.....	116
Figure 7.15	Measured temperature of the four on-board thermistors (A-D) over the full power increase cycle of each insertion into the euthanised pigs.....	116
Figure 8.1	Comparison of volume used by internal PillCam® antenna [41] compared to the, in this thesis, developed conformal antenna design, showing the gained internal space.....	123
Figure A.1	Link-budget model for a CE system.....	126

LIST OF TABLES

Table 2.1	Summary of commercially available CE devices.....	9
Table 2.2	General requirements of wireless CE telemetry systems.....	16
Table 2.3	Transmission requirements for a CE system from within the body [55-59].....	18
Table 3.1	Basic restrictions on the SAR in W/kg according to the exposure guidelines for frequencies above 100 kHz [108].....	43
Table 3.2	Typical skin depths in human tissue [91].....	44
Table 3.3	Electromagnetic properties of human tissue at 433 MHz.....	46
Table 4.1	Measured dielectric properties of the phantom material.....	56
Table 5.1	Required specifications of transmitters for CE.....	75
Table 5.2	Data packet set up with message header, package counter, time stamp and RSSI.....	82
Table 5.3	Step-by-step of moulding and coating process.....	88
Table 6.1	Capsule settings.....	93
Table 6.2	Decrease in RSSI per 10 cm separation step.....	98
Table 7.1	Pig experimental set-up.....	102
Table A.1	Link budget analysis between the Tx and the Rx.....	127

LIST OF ACRONYMS

AiP	Antenna in Package	ISM	Industrial, Scientific, and Medical
ASIC	Application-specific integrated circuit	JPEG	Joint Photographic Experts Group
AoC	Antenna On-Chip	JTAG	Joint Test Action Group
AUT	Antenna Under Test	LED	Light Emitting Diode
CCD	Charge Coupled Device	MC	Microcontroller
CE	Capsule Endoscope	MCU	Microcontroller Unit
CMOS	Complementary Metal Oxide Semiconductor	MD	Medical Device
CRC	Cyclic Redundancy Check	MPEG	Moving Picture Experts Group
CS	Compressed Sensing	NTC	Negative Temperature Coefficient
CSRR	Complementary Split Ring Resonators	PCB	Printed circuit board
CST	Computer Simulation Technology	PEEK	Polyether Ether Ketone
DPCM	Differential Pulse-Coded Modulation	RF	Radio frequency
EDA	Electronic Design Automation	Rx	Receiver
EIRP	Effective Isotropic Radiated Power	SMA	SubMiniature version A
EM	Electromagnetic	SMD	Surface Mount Device
ESA	Electrically Small Antenna	Tx	Transmitter
ETSI	European Telecommunications Standards Institute	UI	User Interface
FBPA	Fast Back-Projection Algorithm	US	Ultrasound
FSPL	Free Space Path Loss	UWB	Ultra-wide bandwidth
GI	Gastro Intestinal	VNA	Vector Network Analyser
GPIO	General Purpose Input/Output	VSWR	Voltage standing wave ratio
HFSS	High Frequency Structure Simulator	WCE	Wireless capsule endoscopy
IMD	Ingestible Medical Device	WMTS	Wireless Medical Telemetry Services

LIST OF PUBLICATIONS BY THE CANDIDATE

Journal Publications

1. **J. Faerber** *et al.*, "In Vivo Characterization of a Wireless Telemetry Module for a Capsule Endoscopy System Utilizing a Conformal Antenna," IEEE Transactions on Biomedical Circuits and Systems, vol. 12, no. 1, pp. 95-105, Feb. 2018. DOI: 10.1109/TBCAS.2017.

Conference Publications

1. **J. Faerber** and M. P. Y. Desmulliez, "Conformal meander shaped antenna for biotelemetry in endoscopic capsules," in Antennas & Propagation Conference (LAPC), 2015 Loughborough, pp. 1-4, 2015.
2. **J. Faerber**, G. Cummins, and M. P. Y. Desmulliez, "Design of conformal wideband antennas for capsule endoscopy within a body tissue environment," in 46th European Microwave Conference (EuMC), 2016, pp. 1223-1226, 2016.
3. G. Cummins, H. Lay, B.F. Cox, V. Seetohul, Y. Qiu, F. Stewart, **J. Faerber**, V. Mitrakos, M. Al Rawhani¹, J. Beeley, D.E. Watson, R. Poltarjonok, C. Démore, I. Nathke, R. J. C. Steele, D. Cumming, M.P.Y. Desmulliez & S. Cochran, "Sonopill: A Platform for Gastrointestinal Disease Diagnosis and Therapeutics"; 6th Joint Workshop on New Technologies for Computer/Robot Assisted Surgery, 2016
4. V. Seetohul, **J. Faerber**, C. Demore, S. Cochran, "Simple microultrasound capsule endoscopy" in Ultrason. Biomed. Microscanning, 9th International Conference, Scotland, 2014.

CHAPTER 1 INTRODUCTION

Capsule Endoscopy (CE) has become a promising alternative to scope-based endoscopy for imaging the Gastrointestinal Tract (GI) and carrying out medical diagnosis and therapy. The GI tract can be inspected with minimal discomfort, which has led to greater patient acceptance, benefiting from colorectal disease screening programmes by encouraging earlier diagnosis and treatment.

Endoscopic capsules became commercially available in 2001 [1]. Since then, they have predominantly relied on optical imaging as main means of diagnosis. Various other diagnostic and therapeutic modalities have been put forward over the years to be integrated into these capsules to increase their diagnostic potential [2, 3]. One modality being investigated by the Sonopill Project [4] is the use of ultrasound imaging in conjunction with optical imaging to improve the early diagnosis and treatment of a wide variety of gastrointestinal diseases, such as colon cancer, due to its ability to detect subsurface neoplasms, among other pathologies [2, 4, 5].

However, an increase in the number of modalities present in a capsule leads to a rise in data generation and a reduction in the space available within the capsule. This new technology raises new challenges in the design and fabrication of these capsules, since materials have to be chosen carefully, and achieving miniaturisation and integration becomes more complex. Increased data generation will result in greater demands on currently used medical telemetry systems, such as the internally located helix antenna found within the Medtronic PillCam®. Denser integration means less available internal space, making it harder for relatively large components such as this helix antenna (approximately 8 mm wide and 5 mm in diameter) to fit within the capsule.

One solution is to place a conformal antenna on the external surface of the capsule [6-8]. This has the advantage of not using any internal space, although it does require, if placed outside the shell of the capsule, an additional coating to protect the antenna from the surrounding conductive tissue and maintain biocompatibility [9, 10]. The restrictions on space are not the only limitation on the antenna design, given that transceiver systems for ingestible medical devices must also overcome the challenges associated with the need for high data rates and omnidirectional radiation distribution [11, 12]. The effect of frequency shifts, polarisation changes and the high attenuation of the signals as they propagate through different dielectric body layers must all be taken into account when designing antennas for this application. Finally, the antenna needs to

be safe to use inside the human body, meaning it should be coated in or consist of biocompatible materials. Additionally, electromagnetic radiation from the antenna must not heat local tissue by more than 1°C [13], to be compliance with patient safety standards and regulatory requirements including IEEE C95.1-2005 (Safety Levels with Respect to Human Exposure to Radio Frequency Electromagnetic Fields, 3 kHz to 300 GHz [14]). Therefore, it is important to use a low-power data transmission system which can transfer the patient's data through the highly absorbent tissues while the system is in motion.

This thesis presents the simulation, design and manufacture of a transceiver system using a conformal helix antenna on a rapidly prototyped endoscopic capsule shell with integrated electronics. This integrated system has been successfully tested *in-vitro* and *in-vivo* using pigs.

1.1 DESIGN ELEMENTS

The design of ingestible telemetry systems consists of several inter-dependent elements which are shown in Figure 1.1. All aspects are treated in more details in the following sections of this chapter.

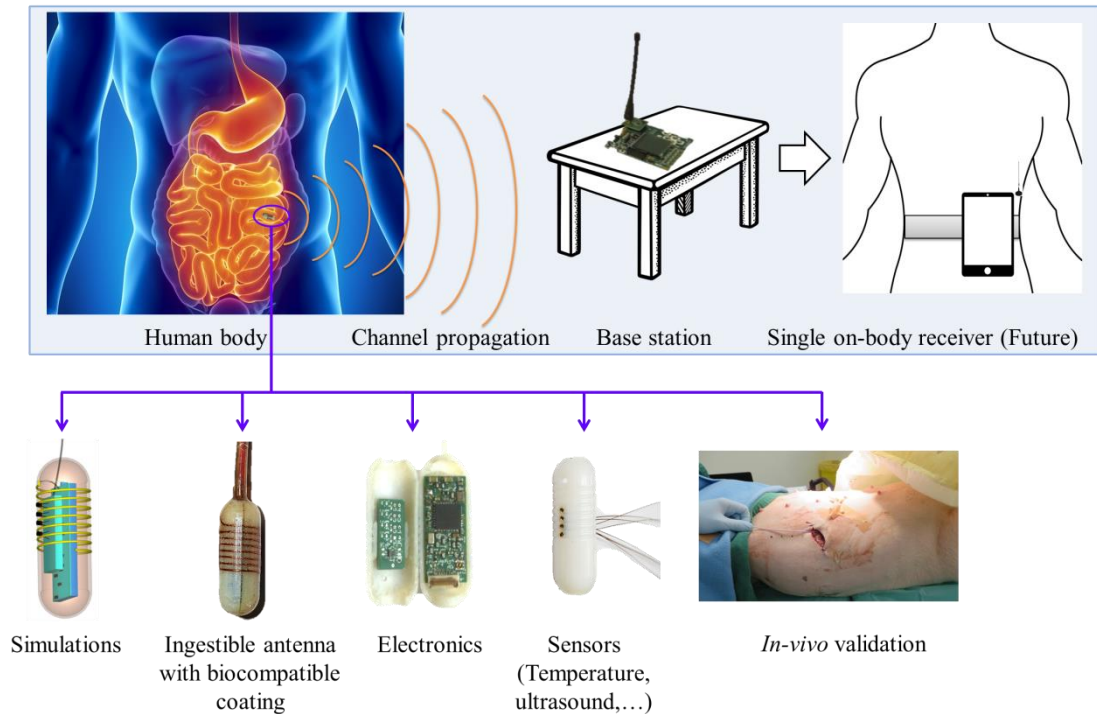


Figure 1.1: Overview of the elements involved in the design of ingestible telemetry systems

Human body

The human body, especially the GI tract, plays a key role in the development of Ingestible Medical Devices (IMDs). It sets limits for each design element and affects the performance of the whole system. Since the body consists of highly lossy dielectric materials, it influences propagation of the RF signals. Equally, RF exposure affects the human body, making patient safety critically important.

Base station

The base station serves as the data receiver and is placed nearby, for example on a portable trolley, or it could be incorporated within an on-body device in future real-life applications. It contains, among other things, antennas, a data acquisition unit and an interconnection system linked to a computer. The performance of its receiver is as crucial as the performance of the capsule antenna transmitter itself in terms of efficiency, bandwidth and directivity.

Channel propagation

RF wave propagation is not only influenced by body materials, but also by the environment in which the signal transmission takes place. Radio signals can be scattered by nearby objects, and can cause multipath propagation. Configuring the system so that these influences are taken into account improves its wireless performance.

Antenna

The antenna forms a key focus for this thesis. It defines the quality of the wireless signal and determines its efficiency, bandwidth and distribution of radiation, while coupling with the surrounding tissue leads to the required performance. Miniaturisation techniques make use of the smallest available volume of the capsule whilst leaving room for other electronic components.

Electronics

Printed circuit boards contain the integrated electronic system driving the antenna and the sensors. The components typically comprise a transceiver system together with a programmable Microcontroller Unit (MCU) to provide the data communication. Low power consumption is required, since the small integrated batteries only have a limited life, unless other options are used, such as wireless power transfer. The electronics are directly related to the antenna, and define the overall capabilities of the system.

Sensors (temperature, ultrasound, pH...)

Nowadays, ingestible endoscopic capsules should not just use optical imaging, but also various therapeutic modalities, including pH, temperature and pressure sensors, which have all been investigated to increase their diagnostic potential [2].

1.2 THESIS OUTLOOK

This section summarises the contents of the eight chapters of this thesis.

Chapter 2 presents the literature review, gives an overview of the CE technology used and lists the available devices and their specifications. A range of antenna designs is listed for ingestible and implantable medical devices, alongside the basic requirements for data telemetry in CE systems. The antenna design process and suggested antenna designs from the literature are summarised alongside explanations of different antenna fabrication techniques.

Chapter 3 adds to the previous chapter by detailing the effects that lossy matter has on electromagnetic radiation and antenna performance. Because the performance of the antenna depends to a large extent on the surrounding material, the chapter discusses the different available numerical and physical human tissue models mimicking the human body for the first prototype tests. Patient safety is one of the main factors influencing the design of medical devices. The Specific Absorption Rate (SAR), which is introduced here, measures the energy the tissue absorbs when exposed to radio frequency magnetic fields.

In *Chapter 4*, the electromagnetic performance of different antenna designs is simulated and measured. Miniaturisation techniques are investigated and the final conformal helix design of the antenna is fully analysed, including tuning to the correct resonance frequency of 433 MHz and SAR simulations.

Chapter 5 includes the integration, packaging and assembly process with all the electronical components for the final prototype. The coating process of the biocompatible insulation layer over the full length of the capsule is described in detail and the data transmission program established.

Chapter 6 presents the *in-vitro* characterisation of the full capsule telemetry system. The phantom model set-up is described and the performance of the measurements provided. The *in-vitro* tests offer an effective evaluation method for testing the antenna performance before the *in-vivo* experiments. The *in-vitro* experiments captured the

known problems of measuring small antennas fed by coaxial cables, and the results are taken into account during the *in-vivo* measurements.

Chapter 7 deals with the *in-vivo* experiments of the complete data telemetry system inside porcine models, identifying the challenges of data transfer from ingestible devices under real tissue conditions.

Chapter 8 summarises the results this work achieved, and conclusions are providing regarding the current system while presenting potential future research options.

CHAPTER 2 LITERATURE REVIEW

This chapter provides an overview of the state-of-the-art technology in medical Ingestible Medical Devices (IMDs) and outlines the research into the design and manufacture of antennas for data telemetry used in IMDs. In particular, the chapter emphasises the data transfer (telemetry) requirements, RF radiation within human body environments and the limitation of these devices. This chapter is organised as follows: A summary of the current state-of-the-art in Capsule Endoscopy (CE) is given in Section 2.1. Section 2.2 discusses the wireless telemetry systems in CE. Section 2.3 summarises the requirements for antennas in wireless CE and gives an overview of the state-of-the-art of small conformal antenna design and their fabrication processes, with a brief summary of the helix antenna theory. Section 2.4 completes this chapter with a summary.

2.1 APPLICATIONS OF INGESTIBLE MEDICAL DEVICES

2.1.1 Ingestible MDs – Endoscopic capsules

The basic difference between implantable and ingestible MDs is that the position of the implant is fixed inside or on the body and does not change with regard to the receiver. Implantable MDs are mainly used for diagnostic and therapeutic purposes, while ingestible MDs are found in gastrointestinal endoscopy [12, 15].

Ingestible MDs, like those used in CE, examine the GI tract visually, replacing traditional flexible endoscopy. The GI tract is part of the digestive system consisting of the oesophagus, stomach and small and large intestines [5]. It is 7.5 to 9 metres long, with the small intestine forming the longest part at 6.7 to 7.6 metres. A capsule takes from 8 to 10 hours to pass through the entire GI tract, spending typically 4 hours in the small intestine, and 5 hours in the colon [5].

Video capsule endoscopy was first introduced in 2001 by Given Imaging Ltd (now Medtronic & Covidien), the producers of the first PillCam® [3]. The wireless capsules are small enough to be swallowed (26 x 11 mm) and, while they travel naturally through the GI tract via peristaltic motion, one or two on-board cameras capture and process images and transmit them to external receivers taped to the patient's body. There is no need for sedation, the patient feels no discomfort compared with the scope-based endoscopy, and can continue as normal immediately afterwards. After the device is

excreted naturally and disposed of, a gastroenterologist analyses the transmitted data [1, 2, 16-18]. A recently developed data recorder (DR3, Given Imaging) now shows the video examination in real-time [18].

CE is used to diagnose a variety of gastrointestinal diseases, specifically small bowel tumours and obscure gastrointestinal bleeding as well as colon cancer, Crohn's disease and coeliac disease [16, 18]. Most of these diseases are found in the small bowel, which conventional endoscopy previously not been able to access [19]. Being able to diagnose these diseases at an earlier stage improves treatment outcomes significantly [20].



Figure 2.1: Some commercially available endoscopic capsules: a) PillCam®SB3 (Given Imaging); b) PillCam®COLON2(Given Imaging); c) PillCam®UGI (Given Imaging); d) PillCam®PATENCY (GivenImaging); e) EndoCapsule (Olympus); f) OMOM capsule (Chongqing Jinshan Science & Technology); g) MiroCam (Intromedic); h) CapsoCam (CapsoVision) [21]

Figure 2.1 displays a selection of commercially available endoscopic capsules. The first generation Pillcam SB contained two small batteries providing up to eight hours of continuous imaging at two frames per second (fps), with a camera at one end [16, 22]. The Endocapsule (Olympus, Japan) has an imaging camera at one end, is battery powered and uses a different imaging technology (Charge Coupled Device (CCD) chip) compared with most other capsules (Complementary Metal-Oxide-Semiconductor (CMOS) chip) [18]. The OMOM capsule (Jinshan Science & Technology (Group) Co. Ltd., China) is larger than the PillCam devices, but shows a similar performance with 2 fps and eight hours battery life [18]. CapsoCam (Capso Vision Saratoga, USA) is a

CE system containing four cameras, with a frame rate of 15 to 20 fps and 15 hours lifespan. Instead of wirelessly sending the images to the external receivers, the capsule stores the acquired data on an internal chip, with the drawback of needing to retrieve it for analysis from the stool [18]. Apart from the small intestinal imaging capsules, Given Imaging also produced an oesophageal capsule endoscope, PillCam ESO, to evaluate oesophageal diseases such as Barrett's oesophagus, and a colon capsule endoscope, PillCam Colon, to evaluate various colonic diseases. Both the oesophageal and colon capsule endoscopes have cameras at both ends [2]. The latest PillCam ESO3 acquires images at 35 fps, while the latest PillCam Colon2 acquires images of 4 fps when stationary to save power, and 35 fps when moving [16, 18]. Due to this high frame rate, the PillCam ESO3's battery life is just 30 minutes. However, this is enough to capture images of the oesophagus while the capsule is passing through this section of the GI until it reaches the stomach [16]. Check Cap (Check-Cap, Israel and USA) is developing a completely different imaging solution for colorectal cancer. They are using a device that transmits X-rays to the intestinal wall, and the device captures the reflected X-rays to form a 3D reconstruction of the colon. This system does not need any bowel preparation, and the X-rays provide a view behind the intestinal wall instead of imaging of the gut wall [2]. Table 2.1 summarises the main characteristics of the commercially available capsules.

2.1.1.1 Power

Power management still represents a major challenge in Wireless Capsule Endoscopy (WCE), but improvements in electronics and their power consumption help to optimise the device performance [16, 17, 22]. The power is supplied by batteries whose duration has been improved over the years and can now last up to 12 hours [17, 18]. In future applications, CE will benefit from wireless power transfer for battery-free devices, freeing up more space for diagnostic and therapeutic components, as well as new designs using externally rechargeable batteries or electric induction technology. These new developments will improve their efficiency and prolong capsule endoscopy procedures [2, 22]. One of the developed CE capsules, the Sayaka pill (RF System Lab, Japan), already uses induction charging as a form of wireless power transmission [2, 3]. It is one of the smallest CE systems at 9 mm by 23 mm, and uses one rotating camera with a frame rate of 30 fps to transmit the images to a receiver, which produces a mosaic of the GI tract [2].

TABLE 2.1: Summary of commercially available CE devices

Manufacturer	Model	Dimensions	Modalities	Resolution	Data rate	Bandwidth MHz	Frequency MHz	Frame rate fps
Medtronic	PillCam SB 3	11x26 mm	CMOS	340x340 pixels	2.7 and 5.4 Mbps	3.2 and 6.5	434	2 to 6
	PillCam COLON 2	11x31.5 mm	CMOS	256x256 pixels	2.7 and 5.4 Mbps	3.2 and 6.5	434	4 to 35
	PillCam ESO2	11x26 mm	CMOS	256x256 pixels	/	3.2	434	18
	PillCam ESO3	11.6x31.5 mm	CMOS	/	/	9.7	434	35
Olympus	Endocapsule 10	11x26 mm	CCD	1920x1080 pixels	/	/	434	2
Jinsham	OMOM 2	11x25.4 mm	CMOS	640x480 pixels	/	/	/	2
Intromedic	Mirocam MC1000-WG	10.8x24.5 mm	CMOS	320x320 pixels	/	/	/	3
Sonopill	ERIC/CAIT	10x30 mm	Sensors: pH, Pressure Chemical,CMOS Image High resolution Ultrasound, Temperature monitor	340x340 pixels	2.04kbps and 4Mbps	20	434	0.006 (in this application), 1.5fps (when MCU uses full 4Mbps)

2.1.1.2 Imaging sensor technology

The first developed CE system by Given Imaging, PillCam (launched in 2001), was quickly followed by Olympus's (Japan) battery-powered Endocapsule (launched in 2005), the OMOM capsule (Jinshan Science & Technology (Group) Co. Ltd, China) and MiroCam (Intromedic Co., South Korea) (launched in 2007). PillCam uses a CMOS chip; EndoCapsule uses a CCD chip as an imaging solution. The CMOS technology requires lower power levels than the CCD technology, while a slower frame rate prolongs battery life [22]. The previously mentioned capsule endoscopes use RF-based communication technologies, whereas MiroCam® uses a new technique for data transmission, explained briefly in the sections 2.1.1.7 and 2.2.2. Improved 'hybrid cameras' are also being developed, combining CMOS and CCD chips [22]. In future devices, chip technology improvements will enhance image resolution further [2].

2.1.1.3 Image compression

Since data rates are limited in CE systems, image compression algorithms and enhanced telemetry link technologies help to overcome these performance restrictions. The images captured during the investigation usually contain about 2.45 Mbits (8-bit colour information) of information, but the frame size varies from 256 x 256 pixels up to 1920 x 1080 pixels comprised of 192kB to 6,075kB with a 24 bit RGB color depth [5, 20, 23-25]. This amount of data needs to be compressed to retain all important information while maintaining available data rates. Image compression removes unnecessary information from a picture or video stream, without losing any important details [26]. Higher frame rates are desirable, and so far data compression is a necessary procedure.

Common compression techniques include Joint Photographic Experts Group (JPEG) and Moving Picture Experts Group (MPEG), which require intensive computation, and therefore consume a large amount of power [27]. More efficient compression methods have been studied, one of them being the de-mosaicing technique, which only requires 7.5 mW for 10 fps and an image size of 2.45 Mbits [28]. Another method is a subsampling-based image algorithm for wireless video capsule applications. A Differential Pulse-Coded Modulation (DPCM) followed by Golomb–Rice coding are applied, which makes it capable of working with any commercial low-power image sensor, without the need of a memory buffer or temporary storage [29]. A recently developed framework, called Compressed Sensing (CS), has the potential to drastically

decrease power consumption and computational complexity, by improving the Nyquist-Shannon sampling theorem, using fewer samples to reconstruct a signal [30].

2.1.1.4 Modalities

The earliest capsules have predominantly relied on optical imaging as the diagnostic modality [1]. Various other diagnostic and therapeutic modalities have been suggested over the years for integration into these capsules to increase their diagnostic potential [2, 3]. New modalities are explained in more details in the following section.

Other wireless diagnostic applications involve pH testing to diagnose Gastroesophageal Reflux Disease (GERD). Given Imaging's Bravo pH capsule is one of the wireless, radio telemetry-based, intra-oesophageal pH monitoring systems [2]. Another system, produced by MotilGI (USA), the Smart Pill, measures pressure and temperature, as well as the pH of the whole gut [2, 3, 17].

Capsules for targeted drug delivery are being developed for future therapeutic treatment [2, 3]. Two new capsules, Intelisite (Innovative Devices, USA) and Enterion (Phaeton Research, UK) have shown promising results, and can be used in future for drug delivery [3, 31]. Studies have shown that biopsy is another modality which could soon become reality via micro biopsy devices and spring-loaded Crosby capsule types [3, 18].

One modality the Sonopill project [4] is investigating is the use of ultrasound imaging in conjunction with optical imaging to improve the early diagnosis and treatment of a wide variety of gastrointestinal diseases, including colon cancer, due to its ability to detect subsurface neoplasms amongst other pathologies [2, 4, 5].

2.1.1.5 Locomotion systems

Another limitation of wireless CE is the passive movement through the GI tract. A controlled capsule movement is desirable and currently under development [16, 21]. External magnetic fields used to manipulate movement, radio-controlled robotic capsules with bioinspired legs and propeller-driven 'swimming' capsules are just a few examples of locomotion systems [16, 21, 32-34]. Ankon Technologies Inc., for example, aims to overcome the poor observation results of the stomach cavity by using a steerable, magnetic-controlled capsule endoscopy system. The capsule is controlled by a medical doctor operating a guidance robot via a joystick while the patient lies on the examination bed attached to the robot. The study showed promising results, but

manoeuvrability still needs to be improved [32]. Finally, the VECTOR project (Versatile Endoscopic Capsule for gastrointestinal TumOr Recognition and therapy) investigates, amongst other studies, active magnetic locomotion in the gastrointestinal tract combined with an accurate driving by an anthropomorphic robotic arm [35].

2.1.1.6 Localisation

The physical location of the capsule is important to gain a correct diagnosis. The main localisation systems use magnetic tracking and electromagnetic waves [5, 21]. The PillCam SB system uses the RF triangulation technique by estimating the location of the capsule via RF signal-level measurements of sensors. Given Imaging also patented a system based on a single electromagnetic sensor coil [5, 36].

2.1.1.7 Telemetry

In almost all endoscopic capsules, captured data is transmitted via wireless communication. The quality of the wireless link is defined by the power efficiency of the electronics and the data rate [5]. Some CE systems use commercially available transmitter chips, while others use custom-built solutions [26].

The PillCam systems, for example, use a customised telemetry chip purpose-built by Zarlink, Inc (USA). The chip has a power consumption of 5.2 mW, and a data rate of 2.7 Mbps, with a carrier frequency of 403 to 434 MHz [5]. This chip transmits data from the capsule, therefore it forms a unidirectional link. For future capsules, a bidirectional data transmission is essential for sending and receiving instructions to and from control, for example the capsule therapy system. A proof of concept of a ZigBee module (based on the IEEE 802.15.4 standard) has been applied to experiments by Valdastrì *et al.* [37, 38]. ZigBee networks have a defined data rate of 250 kbps at a carrier frequency of 2.4 GHz, which is too low to transmit images, but sufficient for a data signal, and offers a long battery life [5].

As mentioned previously, MiroCam® uses a CMOS chip as an imaging solution and takes a different approach for data transmission to other CE devices, using a conductive casing consisting of two gold plates with the body as conductor for the image transmission [2, 16, 22, 39, 40]. This new ‘Human Body Communication Technology’ uses electric field propagation through the human body, which therefore bypasses the need for RF transmission. Two external capsule electrodes are used for transmission, alongside eight single-skin electrodes to receive the data using the human body as an

electrical conductor. This reduces power consumption while obtaining images at a higher frame rate of 3 fps, with no need for data compression. This prolonged the length of the operation to 11 hours [2, 5, 16, 18, 20-22, 39]. MiroCam was approved for general clinical use in Europe in August 2007, and by the US Food and Drug Administration (FDA) in June 2012 [20].

2.1.2 Summary

Due to the space constraints and limited technological developments in wireless communications, the telemetry system represents a big challenge for CE designs [21]. While telemetry data rates are slowly improving, new advancements in image compression algorithms will allow high-resolution imaging [5, 21]. A high data rate and low power consumption are important for reliable wireless data transmission, but medical safety limits concerning signal transmission power also need to be taken into account [38]. The advances made in CE will help to improve diagnostic and therapeutic capabilities for treating GI diseases. Due to the increased use of multiple modalities within single CE systems, internal space is becoming increasingly restricted. The need for wireless communication solutions, as well as the development of new antenna designs, is becoming more important. This challenge forms the basis of this thesis. Figure 2.2 shows a view of various available capsules with corresponding X-ray images.



Figure 2.2: Top view of the capsules, with corresponding X-ray image. Left to right: PillCam SB2, EndoCapsule, CapsoCam, MiroCam, OMOM capsule, PillCam ESO2, PillCam COLON2 [41]

2.2 TELEMETRY IN IMPLANTABLE/INGESTIBLE DEVICES

In this section, the basic requirements for telemetry in CE systems are discussed. Telemetry is the transmission of data over a certain distance to a detecting element for storage or analysis. Transmission can either happen through wired or wireless communication technologies. In general, antennas are reciprocal, with identical receiving and transmitting properties. The radiation patterns from receiving and transmitting antennas are therefore the same in free space [42]. Wireless data transfer in medical communications refers to in-body applications which communicate without wires with exterior monitoring and control devices to avoid penetration through the body tissue to ensure a connection [43].

2.2.1 Frequency bands

The choice of frequency bands for wireless IIMDs depends on the data rate, working range, power transfer capability and the various standards adopted by different countries [44]. This thesis focuses on the electromagnetic (EM) radiation occurring in the 433.05-434.79 MHz Industrial, Scientific and Medical (ISM) band. Regulations vary from country to country, and more information can be found from the relevant national licensing authority.

The IEEE 802.15.6 standard [45] refers to existing ISM frequency bands, as well as those approved by national medical and/or regulatory authorities, used to establish a communication standard for low power medical and non-medical applications [12]. The IEEE standard suggests following frequency bands that are safe to use for transmission and reception: 402.0-405.0, 420.0-450.0, 863.0-870.0, 902.0-928.0, 950.0-958.0, 2,360.0-2,400.0, 2,400.0-2,483.5 MHz. Ultra-wideband (UWB) medical devices which implement low-band (3,494.4 - 4,492.8 MHz) or high-band (6,489.6 - 9,984.0 MHz) channels are also supported. The frequency bands may interfere with frequencies already allocated to other operating services, which could lead to harmful effects in terms of false IIMD activation, link unavailability and data corruption [12]. These frequency channels should radiate in a wide enough bandwidth due to permittivity changes of the biological tissue, which is explained in more detail in Section 2.5 [12]. The reflection at boundaries, scattering, absorption and refraction of electromagnetic fields depend on frequency, with greater absorption of the EM waves as the frequency increases [46]. The reflection at most boundaries is low except at the fat-to-other tissue or skin-to-air interfaces [47].

The frequency typically chosen for medical telemetry IIMDs lies in the 433 MHz ISM band, which offers good signal propagation throughout human body tissue [12]. Higher frequencies, such as the 2.45 GHz ISM band, enable a wider bandwidth and therefore higher data rates, which are good for real-time video transmission applications [12]. At wider bandwidths and higher frequencies, attenuation is however higher [48]. Link performances are reduced greatly at the 2.4 GHz frequency [49]. One possible way of amplifying the signal is to use amplifiers and change the operating frequency of the transceiver while keeping the noise level low. Another option is to compress the signals to produce high data rates at increased distances [12]. The designer has therefore to trade-off multiple requirements: frequency, antenna size, bandwidth, data rate, attenuation and power consumption.

2.2.2 Wireless telemetry in capsule endoscopy

A standard CE telemetry system includes a transmitter embedded within a capsule that converts the obtained information to transmit it via a channel. The channel transports the signal and delivers it to an external receiver [21, 50, 51].

Three different types of data transmission have been used so far in CE:

1. Wireless RF transmission (PillCam, etc.)
2. Wireless human body communication technology (MiroCam)
3. Integrated data storage (CapsoCam)

Wireless RF transmission has been proven to be reliable and efficient through layers of tissues, especially at low frequencies such as the 433 MHz ISM band and lower [21]. However, it does have the drawback of high power consumption, due to the necessary electrical components, such as the oscillator and amplifier. Additionally, the RF signal is highly attenuated by the high dielectric body tissue materials [39].

Human body communication technology requires less power than RF communication, but involves a higher number of receiving electrodes being placed on the skin of the upper body [21]. A small study showed no significant interference with pacemakers [20]. If this wireless communication version were to be used in the Sonopill project, the gold plates would interfere with the US transducer as they occupy most of the capsule available surface area. The system works best with tissues with high water content. This can lead to a lack of signal transmission in the higher part of the GI tract [40]. Integrated storage avoids wireless communication, but has the disadvantage of incorporating

additional internal components as well as having to be retrieved from the stool, which can lead to devices and data being lost [21, 50].

2.2.2.1 Telemetry system requirements

To manage the large amount of transmitted data, the telemetry system needs to have a wide enough bandwidth [21, 27]. Since power supply is limited, power consumption of less than 10 mW is desirable when choosing the telemetry system [27]. The chosen working band should match the range of the medical band (Medical Implant Communications Service [MICS] or industrial, scientific or medical [ISM] bands [27].) Table 2.2 shows the requirements of a wireless CE telemetry system.

TABLE 2.2: General requirements of wireless CE telemetry systems

	MICS, MedRadio, ISM	Comments
Transmission time	> 12 hrs	depending on patient
Frame rate	> 2 fps	depending on application
Data rate	≈ 2 Mbps	depending on application
Power consumption	< 10 mW	
SAR limit	< 2 W/kg	
Resolution	> 256x256 pixels	

2.2.2.2 ASIC design

CE telemetry system design relies on the development of Application-Specific Integrated Circuit (ASIC) which processes and transfers the acquired image data through the chosen type of data transmission. For bidirectional communication, it can also receive commands and information. Low power consumption is a critical requirement for the ASIC chip.

The first ASIC developed for the PillCam was a 2.7 Mbps, 434 MHz radio transmitter chip with a power consumption of 5.2 mW designed by Zarlink Semiconductor Inc. (Canada) [5, 17]. Thoné *et al.* developed a low-power 2 Mbps Frequency-Shift-Keying (FSK) transmitter which only consumes 2 mW at 1.8 V using a carrier frequency of 144 MHz [26]. Shen *et al.* proposed a system that transmits at 416 MHz with a data rate of 2 Mbps at a slightly higher power level of 4 mW than Thoné's, but lower than the Zarlink chip described above [52]. At higher frequencies, greater data rates and miniaturised antenna systems can be achieved. This was shown by Gao *et al.*, who

selected a 3-5 GHz frequency band for enhanced antenna performance, and developed a low-power transceiver system producing a data rate of 10 Mbps [53].

The European Project VECTOR investigated a low-power CMOS, which, during normal operation, consumed less than 40 mW at 30 fps, which is less than what most off-the-shelf devices consume [27]. A very small ASIC chip of only 1 mm² was fabricated by Kim *et al.* This used a simple On-Off Keying (OOK) transmitter with image data at a rate of 20 Mbps using a 500 MHz RF channel [54]. The power consumption was not mentioned in this paper.

2.3 ANTENNAS IN WIRELESS CAPSULE ENDOSCOPY

This thesis focuses on RF data transmission using antennas. The suggested designs of antennas are summed up in more detail in the following section 2.3.2. Current medical research increasingly focuses on antenna-enabled IIMDs to overcome many challenges such as (1) low data rate (1-30 kbps), (2) restricted communication range of less than 10 cm, (3) contactless power transfer, (4) reduced power consumption and (5) low sensitivity in a body tissue environment [12, 48]. The tissue type determines the signal losses, power absorption and penetration depth. Recent studies have shown that implantable antennas have enhanced gains at higher frequencies, which also enables smaller-sized antennas and components [12]. Table 2.3 gives an overview of the requirements for wireless telemetry in CE, collected from several papers [55-59].

TABLE 2.3: Transmission requirements for a CE system from within the body [55-59]

Transmission	
Frequency (MHz)	402 (MICS), 433 (ISM)
Tx Power (dBm)	-16
Tx antenna total gain (dBi)	-36
Effective Isotropic Radiated Power (EIRP) (μ W)	< 25 for MICS [60]
Bandwidth (kHz)	200
Polarisation	circular
Propagation:	
Distance (m)	1
Free-Space loss (dB) (1 m)	35
Path loss (dB) (1 m)	-70
Receiver base station:	
Rx antenna total gain (dBi)	2
Rx sensitivity (dBm)	-100
Noise power density (dB/Hz)	-200
Signal quality:	
Bit rate (Mb/s)	2
Bit error rate	10^{-5}
Packet error rate	10^{-3}
Signal to noise C/N_0 (dB/Hz)	75
Tissue property	
Type	e.g. muscle and fat
Rel. permittivity	57 / 11
Conductivity (S/m)	0.8 / 0.08

Most of the commercially available endoscopic capsules use internal antennas to transfer data via RF transmission. It is very difficult to find more detailed information about CE telemetry systems in commercially available capsules because of commercial confidentiality. Some antenna designs can be seen when observing the X-ray images taken from the various available capsules in Figure 2.2 in Section 2.2.1.8. The PillCam[®], for example, uses a helix antenna of an estimated 8 mm width and a 5 mm diameter with six to seven turns, as displayed in Figures 2.3 and 2.4 below.

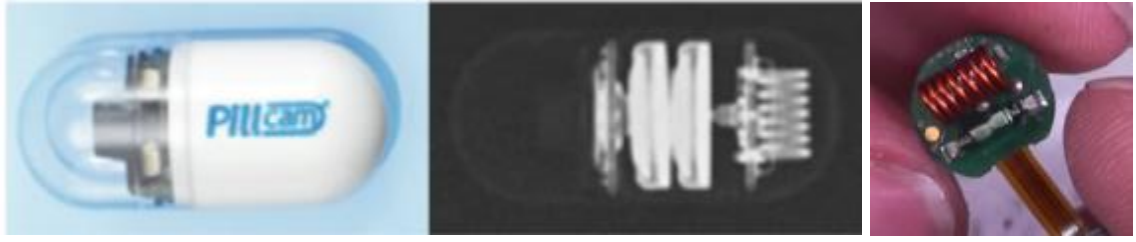


Figure 2.3: External (left) and internal (middle) views of a PillCam® SB; Internal helix antenna of PillCam® (right)

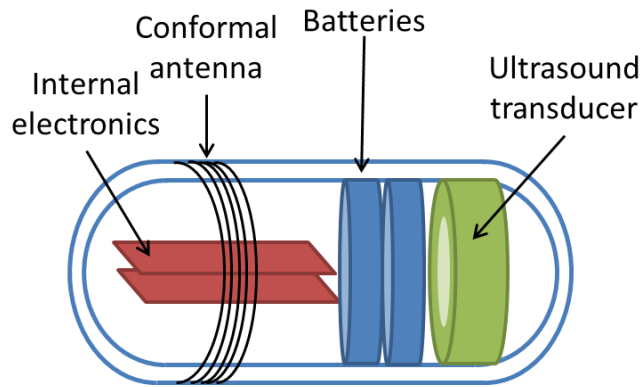


Figure 2.4: Stack-up of a potential Sonopill with a conformal helix antenna

The Figure 2.3 demonstrates clearly that the antenna takes up space that could be put to better use. In Figure 2.4, a different configuration is proposed, with a conformal antenna wrapped around the capsule shell offering a desired space-saving telemetry version.

Relatively low frequency bands are required, as mentioned in section 2.2.1 (frequency bands); however this would lead to a large radiator size. Therefore, miniaturisation techniques are required, resulting in small ingestible antennas, which have low radiation efficiencies as well as gain values.

2.3.1 Antenna design process

Kiourti *et al.* provide a detailed guide to the design, fabrication and *in-vitro/in-vivo* testing of an implantable antenna for medical data transfer applications [61]. The work was carried out on a patch antenna for intracranial pressure monitoring. The guide deals with the steps from the antenna model selection, biocompatibility considerations, miniaturisation options, simulations, fabrication and evaluation of the antenna in *in-vitro* and *in-vivo* experiments. *In-vivo* testing is recommended to verify the antenna functionality. A summary of the suggested design steps collected from several papers [11, 61-65] is given in Figure 2.5:

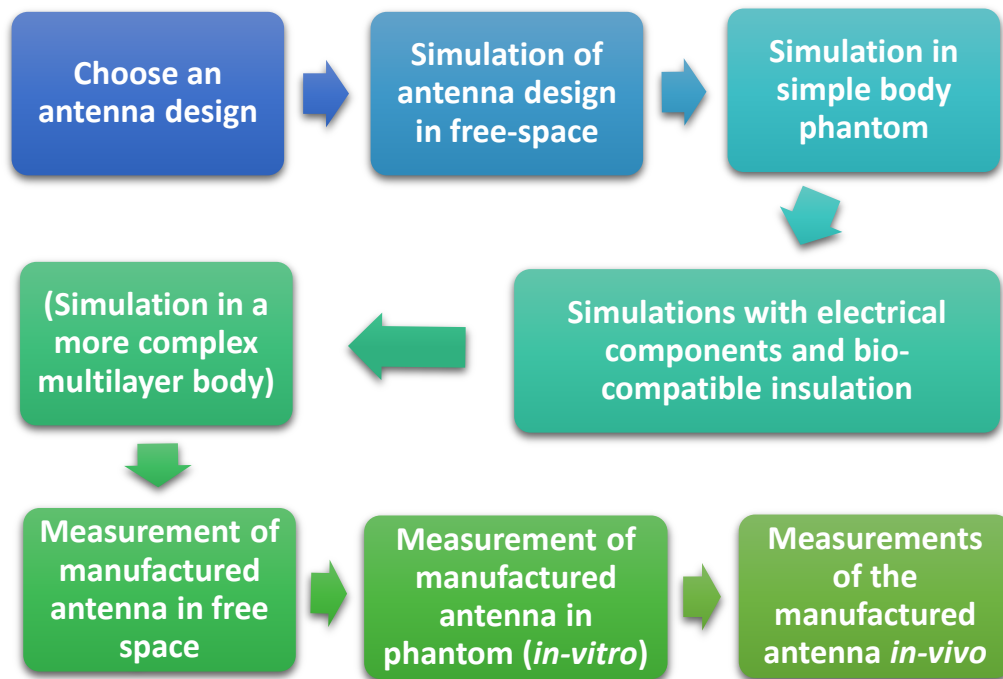


Figure 2.5: Flow chart of the antenna design process steps [11, 61-65]

Choosing an antenna depends on several factors:

- Device physical constraints, since compact packaging is required,
- Frequency band allocation,
- Complex media of propagation,
- Electromagnetic specifications of the signal transmission,
- Range of applications, which decides the implant's position in the body,
- Fabrication processes available, which dictate whether conform, flexible or planar shaped antennas can be manufactured.

The simulation of different antenna designs in free space reduces computation time, and body losses do not influence bandwidth optimisation. After obtaining initial performance results, simulations with added electronics and biocompatible layers are performed. Antennas are placed into a simple body phantom to execute the last modifications and subsequently into a more complex one, to tune them to the required frequency. These simulations are followed by measurements of the fabricated antennas. It is important to check the manufacturing process by producing a few antennas, testing them and comparing the results [64].

Different antenna designs (spherical, spiral, meander and multi-layered) were analysed in [64], and one was manufactured and tested to be incorporated into a capsule. The

final design is a pyramidal stacked antenna, operating with two frequency bands (Medradio 401-406 MHz and ISM 2.4-2.5 GHz). The higher band (2.4-2.5 GHz) improves power efficiency by awakening the sensor from the sleeping state only when receiving a signal. Subsequently, data transmission occurs only in the MedRadio frequency range [64]. The design process followed a standard procedure. First, simulated free space analysis allowed the choice of the antenna typology with reduced computation time. Subsequently, the antenna, inserted in a body phantom, is designed to take into account all the necessary electronic components, power supply and biocompatible insulation so as to realise a complete implantable device. Additionally, a conformal ground plane prevented the active components from interfering with the antenna. The antenna was then implanted subcutaneously in a homogenous cylindrical body phantom (80 x 110 mm) with muscle equivalent dielectric properties. Gain magnitudes of -28.8 dBi and -18.5 dBi were obtained in the two desired frequency bands, respectively [64].

2.3.2 Small, conformal antenna designs – state-of-the-art

Loop, monopole, modified dipole, 3D spiral antennas used for implantable devices are mentioned in the literature, and, if altered, can also be used for ingestible devices. For these, helical antennas are the commonly used configurations. Wideband spiral, outer-wall loop, conformal chandelier-meandered dipole antennas and patches with split ring resonator loading have also been researched [12].

An antenna design often used for implantable models is the micro-strip patch version, because of its direct radiation pattern and flexible design shape. They are also easy to miniaturise due to their conformability and low profile [12, 66]. Since ingestible devices require an omnidirectional radiation due to their constantly changing position and orientation, this antenna is not an option, unless it has a folded design [66].

One way of saving space is to use CE systems external shell by developing conformal antennas. Antennas fabricated on flexible substrates have been developed recently. Cheng *et al.* designed an inductively loaded folded-patch antenna with a resonance frequency of 433 MHz within a homogenous body tissue phantom. It has a diameter of 10 mm and a width of 18.5 mm. Measurements show a good return loss of +18 dB, a typically low gain of -9.6 dBi and efficiency of 1.9% in phantom tissue, due to the high absorption of electromagnetic waves in the human body [67].

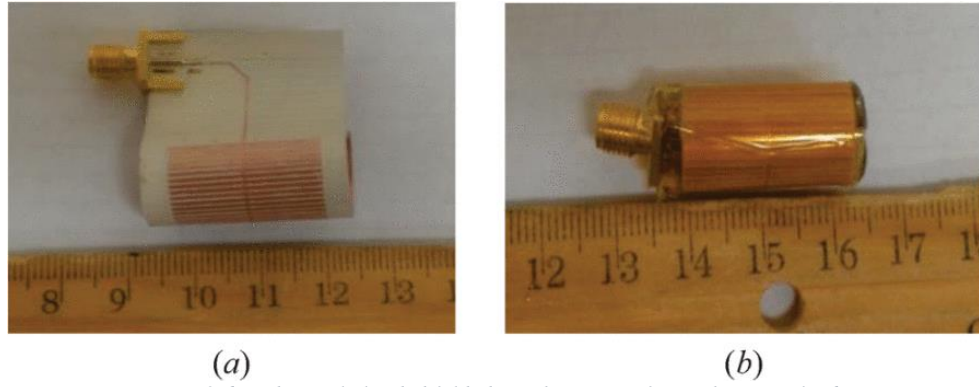


Figure 2.6: Inductively loaded folded-patch antenna from Cheng *et al.* [67]

Wang *et al.* produced and measured a conformal trapezoid strip Dielectric Resonator Antenna (DRA) with a centre frequency of 4 GHz in body tissue. It uses UWB of 3.1-4.8 GHz, and its small size of 8 mm diameter would fit into medical capsule endoscope applications. However, the image transmission measurements have shown a loss of data at a distance of only 10 cm between the receiver (Rx) and the transmitter (Tx), which could be due to the high carrier frequency and/or the choice of Rx [68].

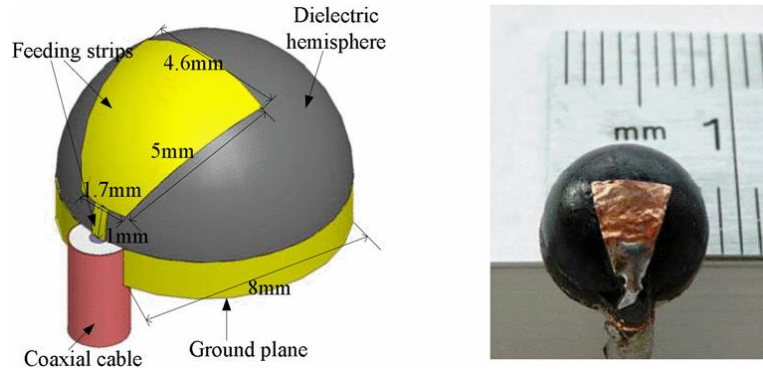


Figure 2.7: Conformal trapezoid strip excited broadband hemispherical dielectric resonator antenna from Wang *et al.* [68]

Yun Sumin *et al.* designed a loop antenna resonating at 500 MHz in body tissue to achieve a UWB of 260 MHz. The outer and the inner radius of the capsule were 5.5 and 5 mm respectively, while its length was 24 mm. The antenna was fabricated on a flexible Printed Circuit Board (PCB) made of polyimide with a thickness of 25.4 μm and a copper line thickness of 18 μm . Measurements have shown a received power of -57.8 dBm over a distance of 15 cm between Rx and Tx, with a radiation output power of 1 mW. It achieved better radiation efficiency than antennas placed in the inside of the capsule. The height of the meander line and the gap between meander patterns can be used as tuning parameters, but electrical components near the antenna can also affect its performance [8].

Loop antennas are typically only used as receivers, because they are poor radiators due to their small radiation resistances, which are smaller than their loss resistances [69]. They also have a poor transmitting gain and a narrow bandwidth [70].

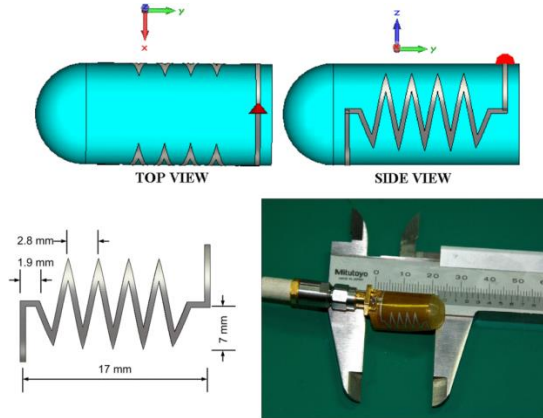


Figure 2.8: Outer wall loop antenna for ultra-wideband capsule endoscope system from Yun Sumin *et al.* [8]

Izdebski *et al.* [91] [44] investigated a conformal chandelier meander antenna for ingestible capsules using the frequency band of 1.4 GHz allocated for the Wireless Medical Telemetry Services (WMTS). The planar-meandered dipole is offset-fed by using an additional series resonance for a closer match. After simulating this antenna, the authors conformed the planar version to a capsule and restarted the simulation. Comparing both results displays no significant change in the return loss, which suggests that the miniaturisation process is made simpler by first changing the planar version, which can then be used to simulate the conformal antenna. The conformal antenna has a circular polarisation to pick up signals from random directions. The group also simulated the influence of internal batteries on the return loss in free-space of the antenna and concluded no critical effect on the matching of the system. The antenna radiates with an efficiency of 0.05% in tissue [65].

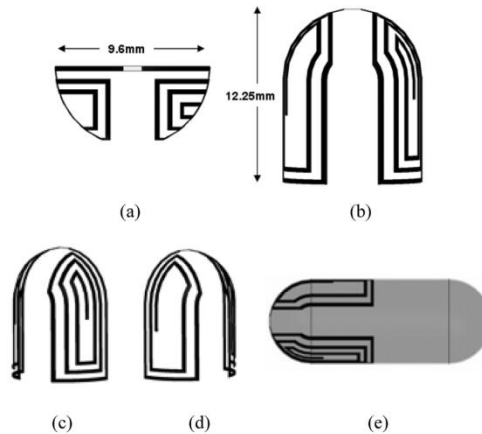


Figure 2.9: A novel chandelier meandered design from Izdebski *et al.* [65]

Alrawashdeh *et al.* investigated two different types of conformal antennas. One small meandered type was simulated, showing a resonance frequency of 785 MHz, for the use of ingestible capsules with a diameter of 11 mm and length of 10 mm. The meander shape helps to extend the antenna length but, at the same time, only uses a small surface. As reported in [65], it was also found that antenna performance did not change significantly when a battery was placed in the internal capsule space. The other antenna was a new flexible loop antenna with Complementary Split-Ring Resonators (CSRRs). This antenna operated at two bands - 403 MHz and 2.45 GHz - within human tissue with the dimension of 30 by 15 mm, which can be bent around a capsule with a 10 mm diameter. Both included a biocompatible layer of Polyether Ether Ketone (PEEK) [7, 71].

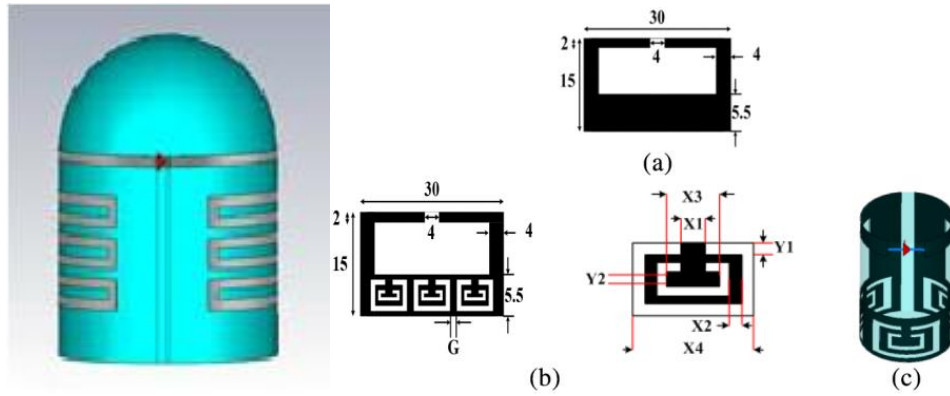


Figure 2.10: A new small conformal antenna for capsule endoscopy [7] and a broadband flexible implantable loop antenna with complementary split ring resonators from Alrawashdeh et al. [71]

Suzan *et al.* recently investigated another conformal design. This group developed a conformal loop antenna for Wireless Capsule Endoscopy (WCE) systems operating at 433 MHz. Its UWB of 744 MHz makes it robust against changes in the environment. A biocompatible coating (PEEK) was included, and the detuning effects of internal batteries and the location of the antenna for different implant depths were simulated. The performance of the system was measured in a liquid tissue phantom [72].

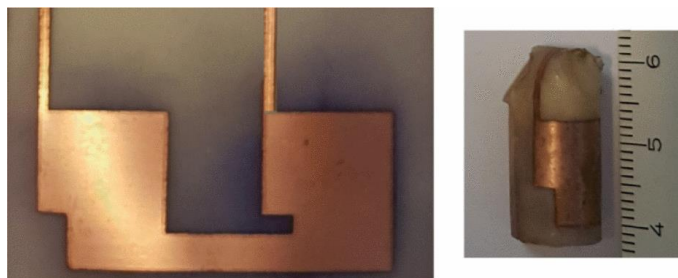


Figure 2.11: An UWB conformal loop antenna for an ingestible capsule endoscope system from Suzan et al. [72]

Apart from conformal antennas, some other designs have been investigated in recent years, with the aim of miniaturising the existing capsule antennas. Kwak *et al.* designed a small spiral antenna that fits inside the capsule with a diameter of just 10.1 mm and a height of 3 mm. It has a frequency of 450 MHz and a bandwidth of 70 MHz [73].

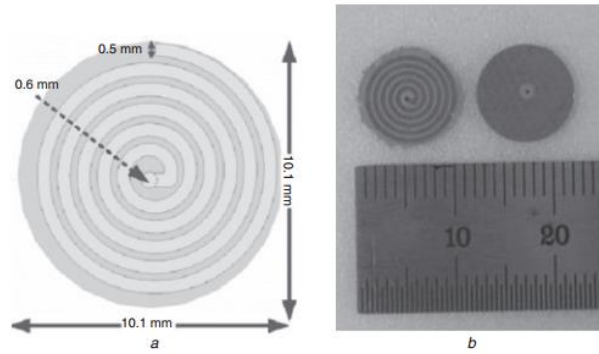


Figure 2.12: Small spiral antenna for a wideband capsule endoscope system by Kwak *et al.* [73]

Lee *et al.* used a similar approach for designing different types of spiral antennas, all of them occupying the internal space of an ingestible capsule [74-76].

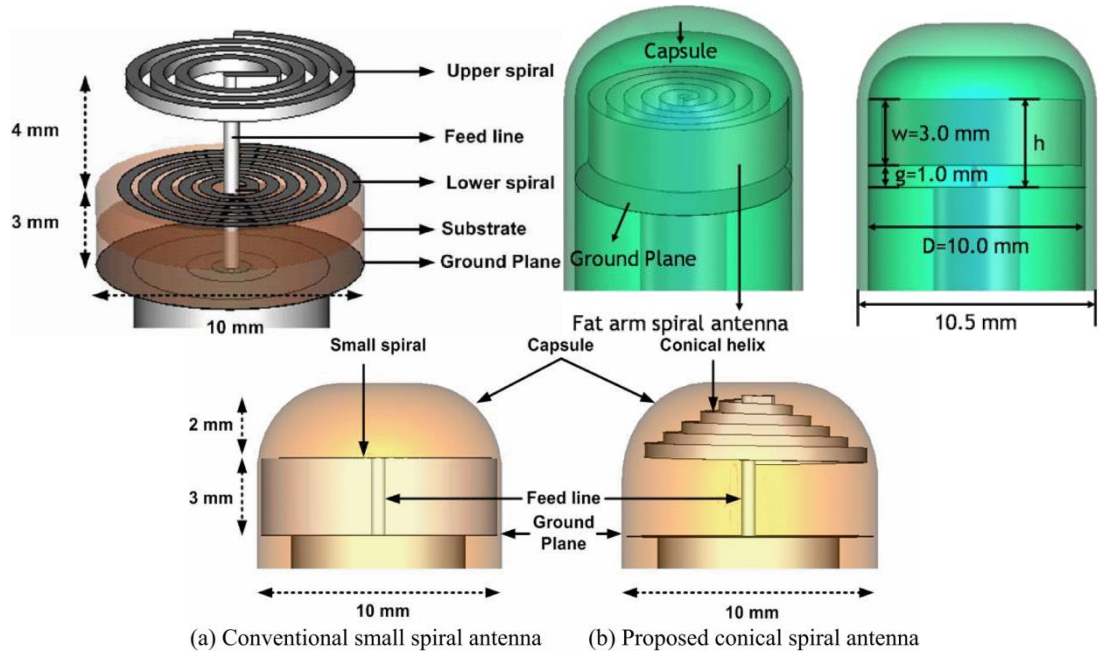


Figure 2.13: different types of spiral antennas suggested by Lee *et al.* [74-76]

Liu *et al.* [77] simulated, manufactured and measured a multilayer, miniaturised and circularly polarised helical antenna using the ISM band of 2.4 GHz for ingestible capsule endoscope systems.

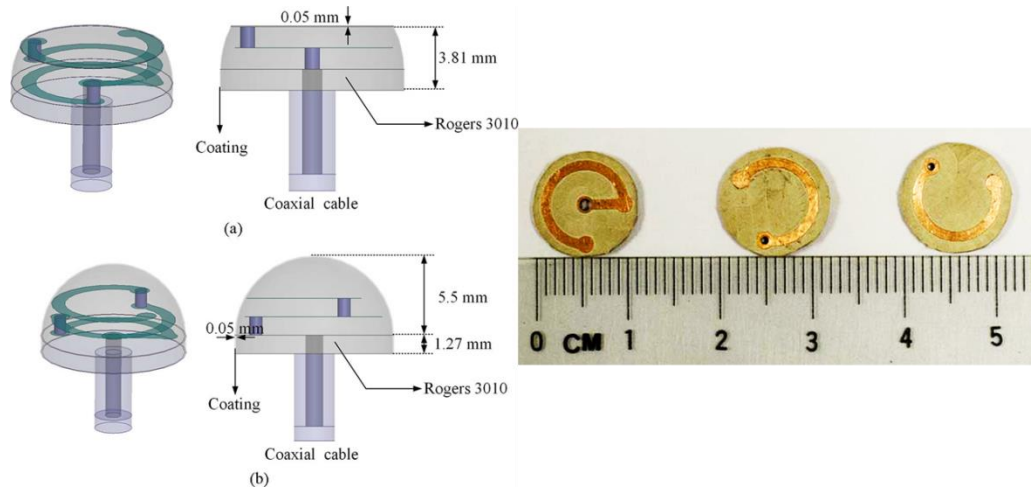


Figure 2.14: Multilayer miniaturised and circularly polarised helical antenna Liu *et al.* [77]

Instead of using separate antennas, recent studies have also focused on Antenna-in-Package (AiP) and Antenna on-Chip (AoC) systems which combine radio chips (in CMOS technology) and antennas to save internal capsule space [17]. Most AoCs are integrated into radio systems using frequencies of approximately 60 GHz [78]. Okabe *et al.* proposed a very small (2.3×2 mm), silicon-based AoC with an antenna radiating at 465 MHz for wireless sensor systems and RF Identification (RFID) in the near-field. The RF signal of 5 dBm (3.1 mW) was supplied to the transmitter (Tx) with the fabricated antenna. The received maximum power in air was measured as -49.4 dBm at the distance of 1 m between the Rx and Tx [79].

2.3.3 Antenna fabrication

The previously discussed conformal designs involved fabricating thin layers of copper on contoured substrates. This section analyses different processes for fabricating small conformal antennas.

In the paper by Gu *et al.* [80], a spiral antenna was deposited by aluminium sputtering on a silicon substrate to transmit signals from a wireless smart sensor. The size of the antenna is in inverse proportion to the operating frequency, and its design also depends on the number of turns, outer diameter, width of spiral pattern and the gap between patterns. With increased turns, the inductance increases and lowers the frequency. As shown in Figure 2.15 (next page), impedance matching is achieved by adjusting the width of the metal tracks and the spacing between the tracks.

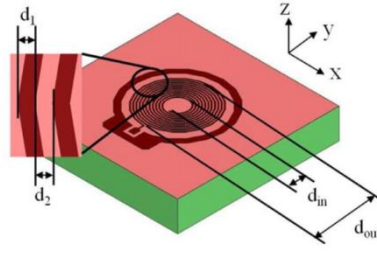


Figure 2.15: Wireless smart sensor with small spiral antenna on Si-substrate [80]

As well as using sputtering, antennas can be fabricated using screen printing [81], inkjet printing [82] and liquid metal-filled microfluidics [83], but these techniques introduce limitations in both spatial resolution and dimensionality. Omnidirectional printing of metallic nanoparticle inks offers one way of meeting the requirements of Electrically Small Antennas (ESAs) on curvilinear surfaces, as demonstrated in [84]. Adams *et al.* [84] presents a way of omnidirectionally printing metallic nanoparticles on curved surfaces, creating meandered, conductive silver lines. This procedure raises the bandwidth limit for ESAs, thus providing a larger scale of possibilities for antenna customisation. Conformal printing on a curved surface is harder than on a planar one, since the nozzle is not always perpendicular to the surface, and could change the dimension of the lines or have to be bent according to the nozzle angle.

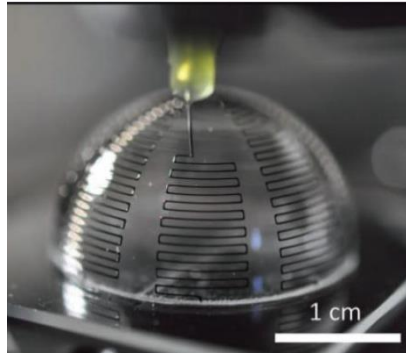


Figure 2.16: Printing of silver nanoparticle inks on curvilinear surface [84]

S.R. Best came up with the design of the electrically small, folded spherical helix antenna [85]. This design has the advantage of being self-resonant, and does not need external components for impedance matching [86]. The Q factor is restricted by the volume of the sphere that contains the antenna, and this also restricts the bandwidth. Electrically small spherical helix antennas are among the most efficient designs to reach the maximum theoretical bandwidth of an ESA, if they use all the available volume within the sphere [86]. The theoretical bandwidth of an ESA is limited by certain aspects such as radiation efficiency, size and radiation power factor [87], all of which need further investigation. But these antennas also have the drawbacks of (1) being

fixed to the spherical shape; (2) being difficult to tune to self-resonance since the feed-point resistance is hard to control and (3) being an immature technology in terms of low-cost fabrication in large batches.

Huang *et al.* [86] used the low-cost Selective Laser Sintering (SLS)-based moulding process, which enables the accurate fabrication of complicated structures in larger quantities. A high-power laser is used to fuse small polyamide particles into a mass that has the desired 3D shape, in this case a folded ellipsoidal helix antenna. By increasing the number of turns of the antenna, the resonance shifts to lower frequencies and the antenna resistance also decreases. But if all other parameters are fixed, the resonance and the input resistance change when the radius of antenna is altered. The effective inductance and capacitance of the antenna ensures that the product of LC (L =inductance; C =capacitance) is always approximately a constant, enabling a self-tuneable antenna impedance matching method without external passive components. The fabricated antenna can be seen in Figure 2.17.

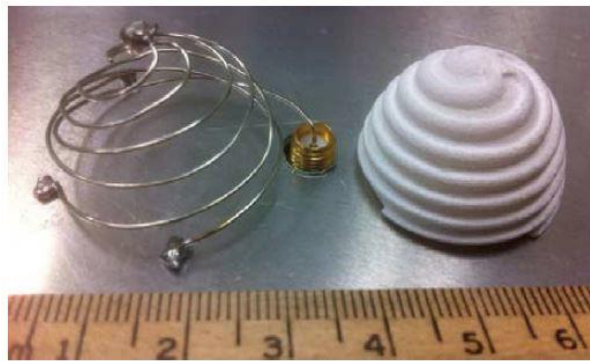


Figure 2.17: Electrically small folded ellipsoidal helix antenna fabricated using selective laser sintering based moulding process [86]

Pfeiffer *et al.* [88] presents three fabrication processes for conformal antennas. Metallic inkjet printing is one of them, but this has issues with producing efficient antennas due to the ink's finite conductivity, the slowness of the process and its inability to print thick traces. A second technique involves printing circuits onto a flat surface and shaping them to the desired profile. Instead of fabricating the antennas manually, which is both time-consuming and expensive, they used silicon wafer processing techniques to print metallic traces onto contoured substrates as shown in Figure 2.18. This process improves accuracy and makes it easier to fabricate an ESA as shown in Figure 2.19. To analyse antenna performance, Pfeiffer *et al.* [88] developed a circuit model based on an ESA's frequency-dependent polarisability, which helps simplify the design process. The far-field pattern of an ESA is similar to that of a small electric dipole or a small

magnetic dipole. The impedance of an ESA is the same as a capacitor in series with a resistor, which produces a strong electric field in its near-field. To even this impedance mismatch out, an inductor is needed to match its feed. Using an inductive sheet impedance cancels out the capacitance. Pfeiffer *et al.* state that the inductive sheet impedance and a spherical helix antenna are in fact one and the same, since the sheet impedance is simply produced by winding a metallic conductor around a sphere, like a spherical antenna. They also found out that having several arms improves the impedance match since this also decreases the radiation resistance and has only a minimal impact on resonance frequency. Helical-shaped antennas have a good transmission gain, and can be fine-tuned by extending or compressing the length of the coils. On the other hand, they can be de-tuned easily by nearby objects [70].

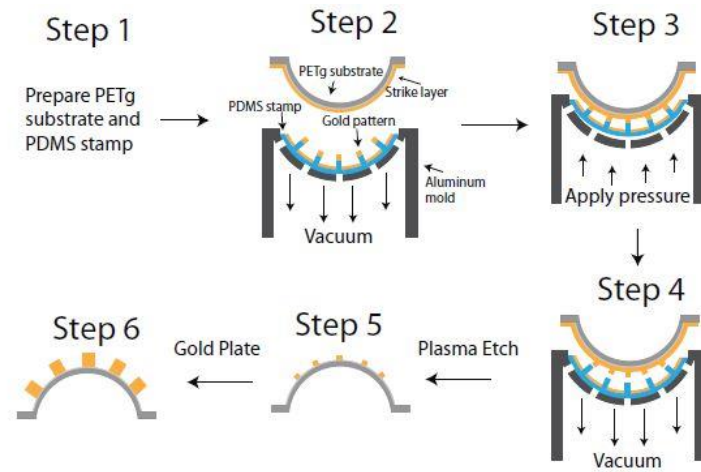


Figure 2.18: Novel methods to analyse and fabricate electrically small antennas: printing metallic traces onto contoured substrates [88]

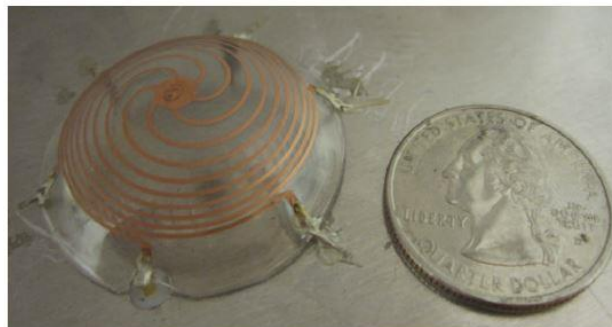


Figure 2.19: Spherical helix antenna with direct transfer patterning by Pfeiffer *et al.* [88]

For future antenna fabrication, it will help to include research on wearable antennas. Whittow *et al.*, for example, reported a novel method of fabricating wearable antennas using inkjet printing [89].

2.3.4 The helix

The antenna analysed in this thesis is a helically-shaped antenna. The helical antenna is a wire antenna, which is wound in the form of a helix [69]. It is considered to be a hybrid of a loop and a dipole antenna [90]. It is usually used with a Ground (GND) plane, which can have different shapes. If a flat GND plane is used, it should have a diameter of at least $3\lambda/4$ [69]. Depending on geometry and frequency, its radiation can be elliptically, plane or circularly polarised [69, 90].

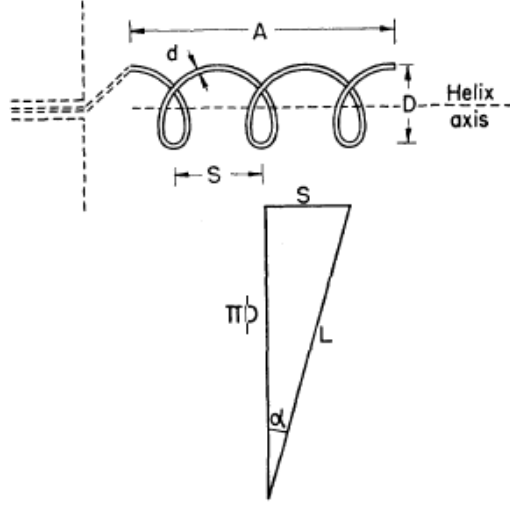


Figure 2.20: Configuration of a helical antenna [90]

Figure 2.20 shows the geometrical configuration of a helix. D is the diameter, S the spacing between turns N and the total axial length is $A = NS$, while the total length of the wire, L_N , is:

$$L_N = NL = N\sqrt{S^2 + (\pi D)^2} \quad (1)$$

The pitch angle α is defined by:

$$\alpha = \tan^{-1}\left(\frac{S}{\pi D}\right) = \tan^{-1}\left(\frac{S}{C}\right) \quad (2)$$

with C being the loop circumference. When the helix is small ($NL \ll \lambda$), it radiates in the normal mode, which means its direction of maximum radiation is in the plane perpendicular to the helix axis and minimum along its axis. Since the helix is a combination of a loop and a dipole, its far-field can be described with the E_θ and E_ϕ components of the dipole and loop, respectively. This process is extensively described in Balanis' antenna book [69].

When the loop circumference of the helix is between $3\lambda/4$ and $4\lambda/3$, the antenna radiates in the axial mode with an optimal design, i.e. a maximum radiation along its axis, for a

circumference is nearly one wavelength [69]. The helix antenna is a travelling wave antenna, since the current travels along the antenna with a continuously varying phase [42]. Summing up from this short overview of helical antennas, it can be said that varying the geometry of the helix antenna changes its radiation characteristics. Also changing the surrounding dielectric media, such as human body tissue, will constantly influence its performance.

2.4 SUMMARY

This chapter gave an overview of currently available endoscopic capsule devices, their mode of operation and challenges in their design. Furthermore, the requirements for CE systems have been investigated and three different wireless data telemetry systems for CE were briefly analysed. Collected antenna design steps from several papers formed the antenna design process followed in this thesis. A number of state-of-the-art small antennas reported in the literature were researched, demonstrating the need of the design of a conformal antenna for ingestible endoscopic systems. Additionally, a more detailed explanation about the helical antenna design was presented.

Based on this literature review, a conformal antenna design for RF data transmission is proposed, helping to reduce space constraints within the CE system and improving the data transfer through high dielectric tissues. This solution features a quick and easy method of manufacturing devices, since thin copper wires are used that can be manually integrated into capsule prototypes, offering an alternative to more complicated fabrication processes.

To understand the challenges involved in the design of small conformal antennas for in-body applications, Chapter 3 provides an overview of the knowledge required to design ingestible capsule antenna systems.

CHAPTER 3 CRITICAL PARAMETERS FOR THE CHARACTERISATION OF ANTENNAS IN THE HUMAN BODY

This section provides an overview of the knowledge required to design ingestible capsule antenna systems surrounded by lossy biological tissues. The antenna performance is strongly affected by the surrounding tissue, reducing its radiation efficiency, changing the radiation distribution and input impedance. The interaction of microwaves with biological materials is described in more detail by Vander Vorst *et al.* [91] and more information about dielectric properties of human tissues can be found in Gabriel *et al.* [92-94]. First the constitutive parameters of lossy media are covered, followed by the parameters which characterise antennas, taking into account the influence of the surrounding biological tissue. This chapter serves as foundation for all the following investigations and outcomes presented in this thesis later on. Section 3.1 deals with the theoretical aspects of antennas in lossy matter, followed by a brief introduction to the fields surrounding an antenna in Section 3.2. Sections 3.3 to 3.5 describe the influence of lossy matter on the performance of an antenna system. The Specific Absorption Rate (SAR) is introduced in Section 3.6 for the analysis of EM waves in biological tissues. Section 3.7 briefly points out the importance of insulation layers for ingestible devices. In Section 3.8 the challenges and limitations for small ingestible are summarised and Section 3.9 presents several solutions to mimic biological tissues and the human body.

3.1 CONSTITUTIVE MATERIAL PARAMETERS: PERMITTIVITY, PERMEABILITY AND CONDUCTIVITY

The dielectric properties of surrounding lossy matter have a significant impact on the performance of a radiating antenna. It does not just change the antenna electrical size, but also its bandwidth, efficiency and gain. The dielectric properties of a biological tissue are generated from the interaction of EM radiation at the cellular and molecular levels [92]. Research has been published discussing the advantages of ingestible and implantable telemetry systems, as well as the challenges involved in designing them. A detailed description of dielectric properties of human tissues for electromagnetic exposure situations can be found in the publications of Gabriel *et al.* [92-94]. Vander

Vorst *et al.* summarize the interaction of microwaves with biological materials and provide fundamental knowledge of this subject in [91].

With a low conductivity, a greater E-field is generated, which enhances wave propagation and reduces the dielectric losses, while a material with a high permittivity lowers the speed of propagation of the E-field and reduces its magnitude. Lossy dielectrics, such as biological tissues, have several polarisation mechanisms which are influenced by an applied EM field and vary in their characteristic relaxations times. This results in complex permittivity behaviours that vary over frequency [95]. This non-linear frequency behaviour is described by relaxation models, with the simplest and most commonly used ones for tissues being the Debye and the Cole-Cole model [96, 97]. A better understanding requires further reading of, e.g., Feldman *et al.* [95].

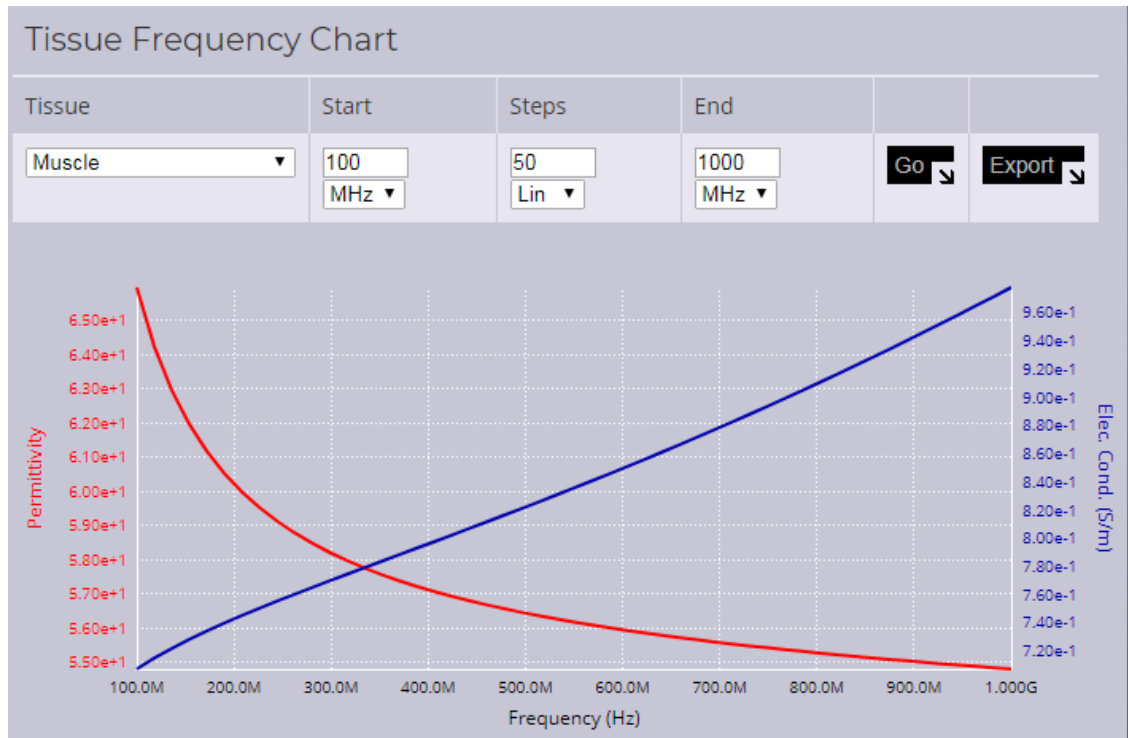


Figure 3.1: Change of relative permittivity and conductivity over frequency for muscle tissue [13]

Figure 3.1 shows that the permittivity decreases and conductivity increases with increasing frequency. Conductivity and permittivity of tissue materials both influence the Specific Absorption Rate (SAR), the Voltage Standing Wave Ratio (VSWR) and the return loss of an antenna. The return loss and the VSWR are related to each other. These three factors are important because they determine the performance of the antenna in a body tissue environment. The reflection coefficient indicates how much power is reflected from the antenna. Ideally, the majority of the power delivered to the antenna should be radiated. The VSWR characterises the mismatch of the transmitting and

receiving antenna. When the antenna is not matched, reflected power causes standing waves along a transmission line which produce unwanted noise. The smaller the VSWR, the better the antenna matches the transmission line and the more power is delivered to the antenna. A perfectly matched antenna has a VSWR of 1.

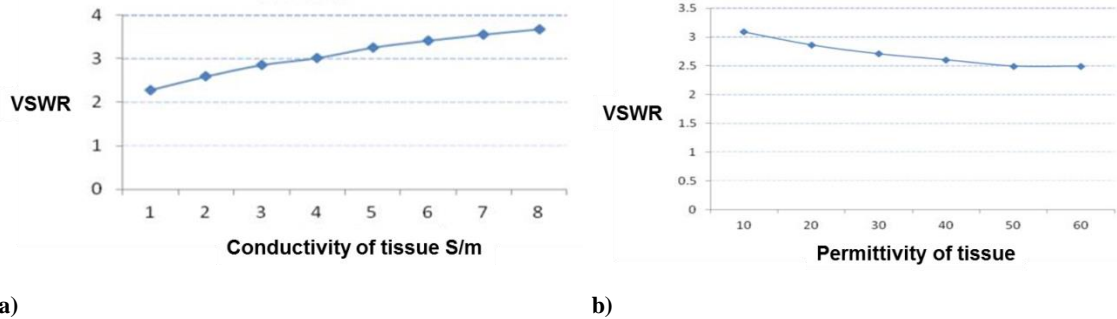


Figure 3.2: a) Variation of VSWR over conductivity of tissue; b) Variation of VSWR over permittivity [98]

Figures 3.2 a) and b) illustrate how the VSWR increases with conductivity and decreases as permittivity increases. Even if the antenna is matched to one type of tissue, mismatch can occur when radiating through a different kind of tissue [62, 98]. In [62], Yuce *et al.* detected 20-30 dB attenuation through the biological tissue within the 3-5 GHz band for every 2 cm, which is not entirely down to absorption by the tissue. The antenna mismatch due to presence of the tissue also contributes to this attenuation.

EM energy is absorbed by lossy human body tissue. Penetration depth depends on frequency and material, as can be seen in Figure 3.3 [97].

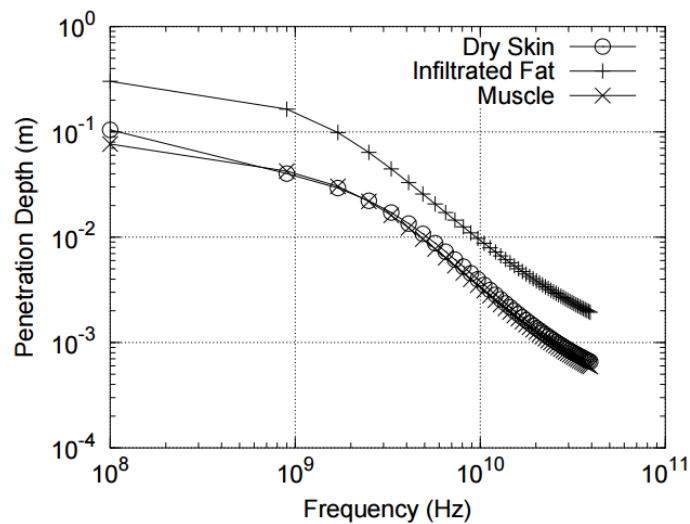


Figure 3.3: Log-log plot of penetration depth from 100 MHz to 40 GHz of dry skin, infiltrated fat, and muscle by Gabriel's Cole-Cole model [97]

The penetration of EM energy decreases as frequency increases. At frequencies in the MHz range, EM waves can penetrate multiple layers of different kinds of tissue, even

when taking into account the reflections caused by the different dielectric properties of the various tissues. Because different tissues differ in their absorption and reflection characteristics and therefore produce mismatched boundaries, modelling these interactions is a complex procedure [97]. For the design of ingestible antennas, it is also important to know that the permittivity of a medium affects the speed of propagation of the wave, and hence its wavelength [99]:

$$v = \frac{1}{\sqrt{\epsilon\mu}} \rightarrow \frac{c}{\sqrt{\epsilon_r\mu_r}} \quad (3)$$

When the relative permittivity $\epsilon > 1$, the wave velocity v and the wavelength λ will decrease, but the resonance frequency f_0 in free space stays the same, as can be seen in equation (4) [42]:

$$\lambda' = \frac{c}{f_0\sqrt{\epsilon_r}} = \frac{\lambda_0}{\sqrt{\epsilon_r}} \quad (4)$$

with μ as permeability, λ as wavelength and c as velocity of light. The new frequency inside a high dielectric material can be calculated with the following equation [100]:

$$f' = \frac{c}{\lambda_0\sqrt{\epsilon_r}} = \frac{f_0}{\sqrt{\epsilon_r}} \quad (5)$$

This equation shows the shift in resonant frequency when the radiator is inserted into body tissues with varying relative permittivities. The dielectric loading effect leads to an increased electrical antenna length, due to the surrounding high dielectric material, and hence a reduction of the resonant frequency [44]. Kim *et al.* demonstrates this frequency shift with an implantable spiral antenna simulated in free-space and in a lossless phantom [101]. A shift to 12% of the original frequency is recorded when permittivity changes from 1 to 49.6. Based on [101], Figure 3.4 shows that the higher relative permittivity of the surrounding medium lowers the resonance frequency, but barely affects bandwidth [10].

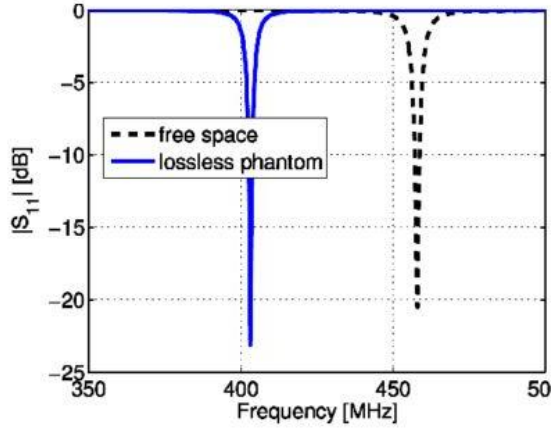


Figure 3.4: Frequency shift of a simulated antenna radiating in free-space versus into a lossless medium [10]

Losses of a dielectric material also modify the current distribution along an antenna, and thus its radiation behaviour [102]. For this reason, an insulation layer establishing a border between the antenna and the surrounding lossy medium helps stabilise the current distribution, and makes the antenna less sensitive to its location within the body material [102].

3.2 NEAR- AND FAR-FIELD

To understand the behaviour of the wave propagation around an antenna, a brief introduction to the fields surrounding an antenna is given below. Figure 3.5 visualises the three different regions: reactive and radiative near-field, and the far-field, of a radiating antenna.

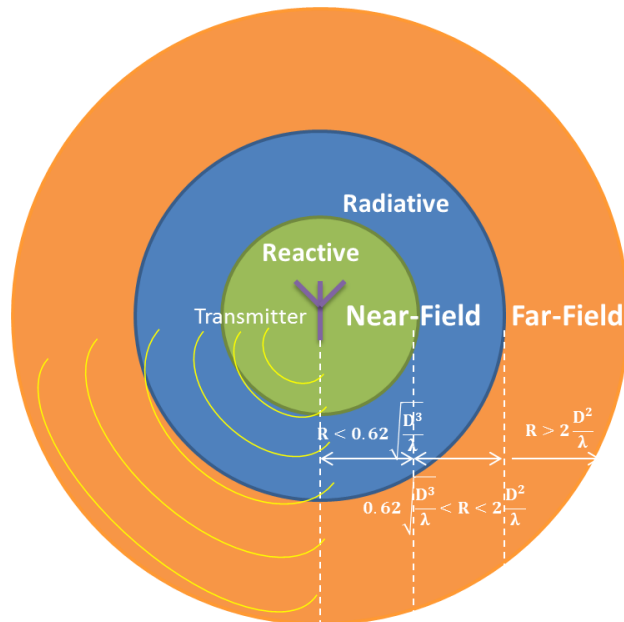


Figure 3.5: Near- and far-field of an antenna

The reactive near-field region is given by

$$R < 0.62 \sqrt{\frac{D^3}{\lambda}} \quad (6)$$

with R as the distance from the centre of the radiation of the antenna to the point of measurement, D as the largest dimension of the antenna and λ as wavelength. A comprehensive analytical description is given by Mikki *et al.* in [103] and [104]. They specify the reactive field as the region where energy is stored and exchanged between the signal source and the E and H fields, but not radiated. In free-space, the reactive near-field affects neither the radiated nor the absorbed power [10, 44]. This reactive component of the EM field has a high power density, hence, in high dielectric materials, coupling occurs with the closest surrounding medium of the transmitting antenna, and more power is lost [102, 103]. The near-field coupling with lossy dielectrics reduces the radiation efficiency and gain of ingestible antennas [105, 106]. An insulation layer can again help reduce this effect by reducing coupling of the nearest tissue surrounding the antenna [64, 107].

The devices in this project use frequencies in the Medical Implant Communication Systems (MICS) band (402-405 MHz) and 433 MHz ISM band to transmit data. The receiver is placed either on the lower body's external surface or at a distance of 1 to 2 m from the body, for example on a table. Since the reactive near-field region is in the range of a few mm within the dielectric biological medium (with $\epsilon_r = 16$ to 64), it is highly unlikely that any coupling mechanisms of the transmitting antenna and the tissue will affect the receiver base station. If, however, the Rx antenna is located in the near-field of the Tx antenna, the coupling would affect the impedance of both antennas, as well as the field distribution around them. This thesis therefore focuses on the far-field telemetry, and the classic definition of efficiency can be used, as described in more detail in the next section.

The reactive near-field may have a different strength depending on which body part is exposed to the radiation; therefore it is essential to demonstrate that the systems comply with human exposure limits to electromagnetic fields, as explained extensively in [108]. However, until now, there have been no regulatory guidelines quantifying exposure to power transmission systems [108]. The radiating near-field region is defined by:

$$0.62 \sqrt{\frac{D^3}{\lambda}} < R < 2 \frac{D^2}{\lambda} \quad (7)$$

The outer boundary is given by:

$$R = 2 \frac{D^2}{\lambda} \quad (8)$$

This region is a mixture between reactive near-field and far-field, since it consists of the radiating E and H fields with the energy radiated away from the source and also energy exchanged with the source. In the radiative near-field, the radiation wave front is still curved and characterised by the angular field distribution, which depends on the distance from the antenna [109]. This region may not exist in an antenna which is very small compared to the wavelength [69]. The far-field is given by:

$$R > \frac{2D^2}{\lambda} \quad (9)$$

In this region, the pattern does not change its planar shape with distance and the E and H fields are orthogonal to each other. Additionally, the far-field region distance must satisfy the conditions of being much larger than the dimension D of the antenna ($R \gg D$) and the wavelength λ ($R \gg \lambda$). The energy radiates from the source in a radial direction. To evaluate the effects of human body tissue on the wave attenuation, the theoretical path loss model for both male and female human phantoms have been presented in [110] and it has been reported that at 402.5 MHz and for the dipole antenna the far field begins at a distance of 47.5 mm from the source. At frequencies from several hundred MHz to a few GHz, both electric and magnetic fields contribute to exposure [108].

3.3 RADIATION POWER, EFFICIENCY, GAIN, DIRECTIVITY

In ingestible wireless systems, good radiation efficiency and wide bandwidth are essential for transmitting over a wide enough range with a high enough data rate [10]. The best way to describe the performance of an antenna system is to use the radiation pattern, gain, directivity, efficiency and power [69].

The radiation pattern is a plot of magnitude of the far-field strength versus the position around the antenna. Directivity is defined as the ratio of maximum radiation intensity in the main beam to average radiation intensity over all space. A narrow main beam indicates high directivity. Radiation efficiency is the ratio of the desired output power to the supplied input power. External and internal losses influence the radiation

characteristics and hence the efficiency. Antenna gain G is the product of efficiency η and directivity D [99].

$$G = \eta D \quad (10)$$

The more energy the tissue absorbs, the more it lowers the radiation efficiency and the magnitude of the far-field [47]. Radiation efficiency is defined by:

$$\eta = \frac{P_{rad}}{P_{source}} \quad (11)$$

where P_{rad} is the radiated power in free-space at far-field distance, and P_{source} is the power delivered to the antenna. The power radiated by the transmitting antenna (source) given below:

$$P_{source} = P_{rad} + P_{abs} \quad (12)$$

is also influenced by the surrounding lossy medium. Power absorption is obtained by integrating losses over the whole volume (Chapter 1.4.1 of [91]). The total energy stored in a volume is obtained by integrating the energy over the volume [91].

The quality of performance of an implantable or ingestible antenna is not related to bandwidth or the antenna radiation efficiency, but to the amount of power it transmits from the host medium [10]. Gain depends on the surrounding material, and increases with decreasing $\tan \delta$, as shown in [64], where the gain increased when the antenna was surrounded by fat rather than muscle tissue. Power, gain and efficiency all depend on the position of the source relative to the lossy dielectric-air interface [44]. This is explained further in the next section about the radiation pattern. The radiated power of a short dipole antenna decays by $\frac{1}{R^3}$ rather than $\frac{1}{R}$, which makes it less efficient than the magnetic loop antenna in the human body [Chapter 2.2.1 of [100]].

3.4 RADIATION PATTERN

Moore [111] stated as far back as the 1960s that the normal concepts of a far-field radiation pattern fail when the antenna radiates into a conducting medium. When an antenna radiates into a lossy medium, power is lost due to the strong coupling of the near-field with the adjacent tissue [10]. Thus, the total radiated power depends on the distance from the centre of the antenna to the point where you want to identify the electric field. But since the receiver of the implanted or ingested device will be placed outside the finite lossy medium in the far-field region, the coupling of the near-field

with the surroundings influences the performance in terms of encapsulation options [10, 44].

The EM field and signal propagation are affected by the location of the device inside the body, depending on the different tissue properties and the distance between the inserted antenna and outer surface of the body, which causes variations in path loss at different frequencies of the system. When inserted in the body, the body becomes the radiator. This makes it difficult to characterise the propagation channel [112]. Chirwa *et al.* [47] discovered that, in the gut region, vertically polarised radiation is more attenuated than horizontal radiation, due to the anatomy of the gut and that radiation characteristics change significantly depending on whether the device is located inside the body or closer to the surface - Basar *et al.* [112] also spotted this.

3.5 BANDWIDTH AND QUALITY FACTOR

This project considers small antennas. Decreasing the electrical size of the antenna leads to a degradation of its electromagnetic performance [10]. The limiting factors in the design of ESAs for IIMDs include the limited available space, the bandwidth and quality factor. The Q factor can be understood as a damping factor of the antenna frequency. The Q factor is described as

$$Q = \frac{f_c}{f_2 - f_1} \quad (13)$$

with f_c as the centre frequency and f_1 and f_2 as the bandwidth threshold. The bandwidth describes the frequency range where the antenna is matched and operates properly in terms of radiated power. The Q factor is inversely related to the bandwidth.

There is a trade-off between bandwidth and Q factor. A higher Q factor means that less reinforcing energy from the transmitter is needed to let it operate efficiently within a narrow frequency range. A wider bandwidth helps to increase the data transmission, since the resonant frequency of the capsule can shift as the electromagnetic wave passes through different tissues. This shift detunes the antenna and lowers the transmission efficiency [7, 62, 63]. If an antenna is tuned to a larger bandwidth, it can cover more frequencies to transmit signals and the shift would not induce any loss of signals [8, 61, 62].

The methods for designing such an antenna are the same for both ingestible and implantable devices since, in both cases, the antenna is optimised to the surrounding

tissue [62]. For ingestible applications, a small-sized antenna (diameter = 10 to 11 mm and length = 26 to 30 mm) on the shell is required, since other electrical or sensing components will use the capsule interior. A smaller-sized antenna is expected to have a narrower bandwidth, however, the surrounding medium introduces losses, and therefore increases bandwidth [10]. Equally, an omnidirectional radiation pattern is necessary to achieve an even transmission of data irrespective of its location and orientation [63, 113]. Encapsulation with a biocompatible layer will protect fragile antenna structures [84].

Developing strategies for transmission through a lossy medium is important. If the permittivity stays the same, the conductivity and hence the loss increase, so is the bandwidth, as shown in Figure 3.6.

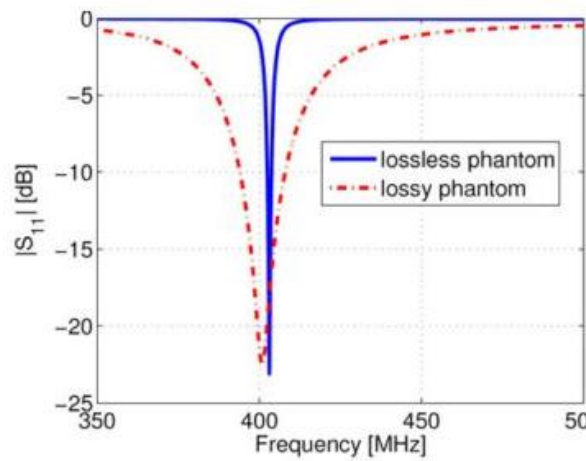


Figure 3.6: Increase in bandwidth for an antenna radiating into a lossy phantom compared with a lossless phantom [10]

The near-field part of the EM field strongly dissipates into the surrounding material. The body tissue absorbs most of the power, some of which is reflected back to the antenna, which can cause wide bandwidths. We can summarise that the bandwidth increases, but the radiated power reduces [Chapter 2.2.4 of [44]]. A lossy medium lets EM energy dissipate into e.g. heat. Bandwidth increases with conductivity and the medium losses. So before improving the Q factor, it is more important to increase the power transmitted through the tissue and *then* optimise the Q factor according to the necessary bandwidth.

3.6 SPECIFIC ABSORPTION RATE (SAR)

Patient safety is the main factor influencing the design of medical devices, with the main issues divided into RF exposure to human tissue and related tissue heating, and

biocompatibility of the capsule with the human body. The latter is explained in more detail in Section 2.5.7.

Medical ingestible implants, which are either constantly close to or inside the body and require wireless data transmission, present potential direct health hazards for the patient, or indirect risks via interference with other medical devices [108]. EM fields can be reflected, refracted, transmitted or absorbed when passing from one dielectric medium to another. This depends on the carrier frequency and the characteristics of the relevant body tissue [91]. Absorbed RF energy tends to be converted into heat and may impair the functioning of the living system [91].

The energy the tissue absorbs when exposed to radio frequency electromagnetic fields is measured by the SAR, defined as the power absorbed per mass of tissue (W/kg) [114]. The SAR is not directly related to input power, but rather to the antenna's current distribution [115]. Power dissipated into the surrounding biological tissue can generate heat, which can have harmful consequences. To compare measured SAR values with safety standards, the results need to be averaged over 1 g and 10 g, as specified in the IEEE guidelines [14, 116].

Mathematically, the SAR (W/kg) is defined by the following equation

$$\text{SAR} = \sigma \frac{E^2}{\rho} \quad (14)$$

and the power absorbed by the human body by

$$P_{abs} = \frac{1}{2} \int \sigma |E|^2 dV \quad \left(\frac{W}{m^3}\right) \quad (15)$$

where σ is the frequency dependent conductivity of the tissue, ρ is the mass density and $|E|$ is the intensity of the electric field inside the tissue.

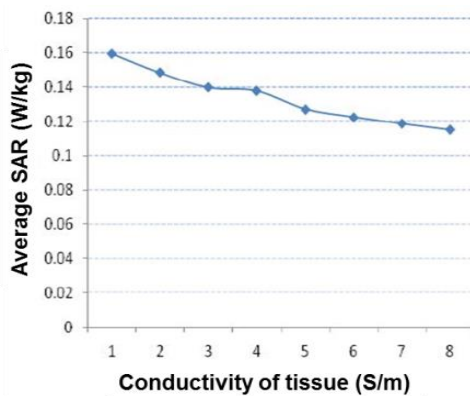


Figure 3.7: SAR over conductivity of tissue [98]

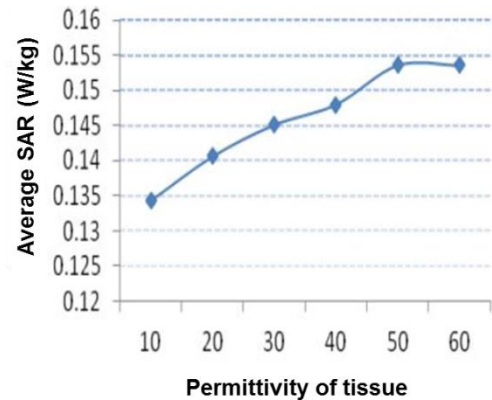


Figure 3.8: Variation of SAR over permittivity [98]

Figures 3.7 and 3.8 show, that the SAR increases with increasing permittivity, and decreases with increasing conductivity. A good conducting material has a very low, rapidly attenuating electric field. Therefore, dissipative losses are high with increased conductivity, but the SAR is low, so less power is absorbed and less heat develops. Absorbed power is therefore related to the electric field and thus the SAR. For that reason, the SAR maximum values can be detected where electric radiation is at its highest in the tissue [12]. The SAR depends on the device location within the tissue, the surrounding tissue property, the computation technique and the individual biological tissue/cell responses [117]. Some studies with rodent and non-human primate models have reported tissue heating with a temperature rise in excess of 1–2°C for 4 W/kg [13].

Organisations such as the IEEE and International Commission on Non-Ionizing Radiation Protection (ICNIRP) provide safety standards [13, 14]. Since patients’ safety is of the utmost importance, standards such as the “IEEE Standard for Safety Levels with Respect to Human Exposure to Radio Frequency Electromagnetic Fields, 3 kHz to 300 GHz” set power limitations to prevent hazardous heating of biological tissue. The maximum power for transmission from any IIMD must comply with the peak spatial-average SAR limitations. Table 3.1 shows the SAR restrictions for the whole body, and for any 10 g or 1 g tissue mass, to prevent thermal stress and local thermal injuries. The ICNIRP sets the SAR to less than 2W/kg for 10 g of contiguous tissue, the IEEE(1992) to less than 1.6W/kg for 1 g of tissue in the shape of a cube, and the IEEE(2005) to less than 2 W/kg per 10 g of tissue in the shape of a cube [12, 14, 108, 116].

TABLE 3.1: Basic restrictions on the SAR in W/kg according to the exposure guidelines for frequencies above 100 kHz [108]

	Averaging mass	Body region	General public (W/kg)	Occupational (W/kg)
ICNIRP 1998 [13]	10 g contiguous volume	head and trunk	2	10
	10 g contiguous volume	limbs	4	20
	whole body		0.08	0.4
IEEE 2005 IEEE [14]	10 g cubical volume	all but extremities and pinna	2	10
	10 g cubical volume	extremities and pinna	4	20
	whole body		0.08	0.4
IEEE 1992 [118], NCRP 1986 [119]	1 g cubical volume	all but extremities	1.6	8
	1 g cubical volume	extremities	4	20
	whole body		0.08	0.4

Those standards are based on different guidelines depending on the organisation, and vary slightly in their definitions.

The attenuation of EM waves in the human body is described by the skin depth. This defines how far most of the microwave power penetrates in the human body [99].

The effective skin depth for a good conductor ($\sigma \gg \omega\epsilon$) is defined by [120]:

$$\delta = \sqrt{\frac{2}{\omega\mu\sigma}} \quad (16)$$

$$\omega = 2\pi f \quad (17)$$

where δ is the skin depth, ω the angular frequency (rad/s) of the antenna, μ the permeability of the tissue (H/m), and σ its electrical conductivity (S/m). For most biological materials, a more general expression should be used instead [91]:

$$\delta = \left(\frac{1}{\omega}\right) \left\{ \left(\frac{\mu\epsilon}{2}\right) \left[\sqrt{1 + p^2} - 1\right] \right\}^{1/2} \quad (18)$$

where $p = \sigma/\omega\epsilon$ is the ratio of the amplitudes of the conduction current to the displacement current. The attenuation constant α for general lossy media is the inverse of skin depth $\delta = \frac{1}{\alpha}$ [99]. As $\frac{\sigma^2}{\epsilon^2\omega^2} \ll 1$, only the displacement current exists and we can use following equation for α [121]:

$$\alpha = \frac{\sigma}{2} \sqrt{\frac{\mu}{\epsilon}} \quad \left[\frac{Nep}{m} \right] \quad (19)$$

The skin depth decreases as the frequency increases, and decreases as the conductivity increases. In other words, the signal penetrates tissue better at lower frequencies [91]. This is desirable for ingestible applications. The lower the water content of a biological tissue, the deeper a wave can penetrate [Chapter 3.1.1 [91]].

TABLE 3.2: Typical skin depths in human tissue [91]

Parameter	Radio FM	TV transmitter	Mobile phones	Mobile phones
Frequency (MHz)	100	450	900	1,800
Skin depth (cm)	3	1.5	1	0.7
Depth at which power reduces to 1 % (cm)	9	4.5	3	2

3.7 INSULATION LAYERS

In terms of biocompatibility, the ingestible medical device should clearly not harm the patient, nor should the body reject it. Wireless operation of implantable devices reduces the risk of infection and patient discomfort [122]. The antenna structure should either be hermetically sealed by a biocompatible superstrate dielectric layer or insulated with a thin layer of low-loss biocompatible coating as it is placed in a conductive environment with high permittivity [61, 123]. This insulation layer helps to stop the tissue from reacting to the shell material, prevents short-circuiting effects due to the conductive nature of the human body tissue, and may also enhance the performance of the medical telemetry applications [64].

The radiation efficiency of an ingestible antenna is mainly affected by the strong near-field coupling between the antenna and the surrounding biological tissue. As mentioned in Sections 2.5.1 and 2.5.2, the insulation layer helps steady current distribution when an antenna is inserted into lossy biological tissue, and reduces coupling with the nearest tissues to the antenna. Merli *et al.* simulated varying thicknesses of biocompatible insulation layers and reports a decrease in lost power and hence in an increase in radiation efficiency with increasing layer thickness [107].

The encapsulation affects antenna performance by reducing overall dissipative losses if conductivity is close to 0 S/m [103, 104]. Different materials can be used, such as Zirconia, PEEK, DMS and Silastic MDX-4210. Zirconia has the best electromagnetic properties (lower σ and lower ϵ), but PEEK is generally the most commonly used material, since it is easier to handle and to produce [12, 64].

3.8 CHALLENGES/ LIMITATIONS OF INGESTIBLE ANTENNAS

Wheeler published his analysis of the limitations of ESAs, in terms of bandwidth, gain and Q factor [87]. This study is based on results in a lossless environment and can therefore only be considered under very limited conditions. Analysing antenna design is made more complex by the near-field coupling of the surrounding lossy tissue environment and by the way the human body alters the EM wave propagation. So it is difficult to define the dimensions of the radiating antenna and the minimum sphere surrounding it, which forms the part of the evaluation of ESA limitations in free-space [124, 125].

Using Wheeler's submarine model and the ESA analysis of [87, 120, 126] can help to find preliminary notions of the radiation of small ingestible antennas that are used in

this thesis work. However, we can conclude that ESA definitions surrounded by a single lossy medium are not available yet, and it is particularly challenging to identify ESA radiation characteristics within a constantly changing environment such as the human body. Connecting an ESA to an unbalanced transmission line, such as a coaxial cable, can increase radiating currents on the outer part of the cable, affecting measurement results. Although ingestible devices have their electronics and radiators integrated within the capsule, measuring prototypes can still be problematic. Coaxial feed interferes with the antenna radiation, due to the presence of the dielectric body phantom [72, 100, 127]. To perform accurate overall measurements, the implantable antenna should be isolated from the surrounding material. The currents on the external surface of the cable dissipate into the lossy materials, increasing radiation and variation of the reflection coefficient [128]. This effect will be further discussed and evaluated in Chapter 4.

3.9 HUMAN BODY MODELS

The wireless endoscope antenna radiates from within a lossy and dispersive human body tissue. It is important to take human body effects into consideration to achieve a functional antenna design. A real human tissue environment would benefit the characterisation of antenna performance; however, this is neither economical nor practical for first prototype tests. Table 3.3 displays the large variation in tissue properties in the human body at a frequency of 433 MHz.

TABLE 3.3: Electromagnetic properties of human tissue at 433 MHz

Tissue properties	Frequency: 433 MHz			
	ϵ'	ϵ''	σ (S/m)	$\tan \delta$
Muscle	56.90	34.10	0.80	0.60
Skin	46.10	29.60	0.7	0.64
Fat	5.50	1.70	0.08	0.31

Instead, human body phantoms are used that approximate the human tissue as a homogeneous or heterogeneous 3D medium, whose essential properties are as close to those of the human body as possible. This method offers a simple, cost-effective solution, although it lacks accuracy and does not take into account the frequency-dependent characteristic of human tissues [67].

There are two approaches to examine EM radiation from RF devices: 1) physical tissue phantoms (liquid, solid, gel-like) [129, 130], that mimic the EM characteristics of human tissue and 2) a computational modelling method, i.e. simulations [131, 132]. For simulations, numerical human body models are available from High Frequency Structure Simulator (HFSS, Ansys Inc.) and Computer Simulation Technology (CST), offering frequency-dependent EM parameters, including relative permittivity and conductivity, for most human organs and tissues [67]. The physical and numerical models can further be divided into homogenous, single-layer phantom models [123] and more realistic, multilayer models consisting of several tissue properties [133]. Additionally, simple box (cubic or spherical) models are used, as well as realistic human-shaped models [112, 134]. Kiourti *et al.* [96] provides a collection of phantoms used in the literature to test implantable patch antennas, as well as a brief overview of tests within animal tissue. A detailed summary of a number of phantoms is also given by Ito [135].

Modern simulations software such as CST and Ansys HFSS have deployed very accurate body models from the Visible Human Project® (named Hugo) including a majority of tissue permittivity and loss values over a 10 MHz to 100 GHz frequency range. Gabriel [92-94] obtained those particular values, and they are commonly used in the interaction of EM radiation and biological tissues. Additionally, high resolution virtual family models are provided by the IT'IS Foundation and are freely available to the scientific community, as pictured in Figure 3.9 [136].

Simple tissue-mimicking materials can be used for the initial design steps and more body tissue-like phantoms at a later stage of the design process. Phantoms in simulations help save time, while physical phantoms reduce experimental costs and experiments can be repeated numerous times without changes in properties. Additionally, there is no limited shelf-life of real biological tissues to worry about.

Yuce *et al.* [62] reviewed useful phantom recipes and stressed the advantage of dry materials over liquid mixtures for their long-lasting nature of up to a year. Main ingredients included graphite powder, ceramic powder and a bonding resin. Water is replaced by a liquid monomer whose change of composition allow for variation of properties. Saline solutions can also be used to simulate a very simple tissue environment. Jegadeesan *et al.* [137] used a gel made out of distilled water, sugar, salt and agar to mimic skin at 402 MHz and Onishi *et al.* [129] fabricated an agar-based

solid phantom. Animal tissue can also be used as phantom material, since it has very similar electromagnetic properties to human tissue [62].

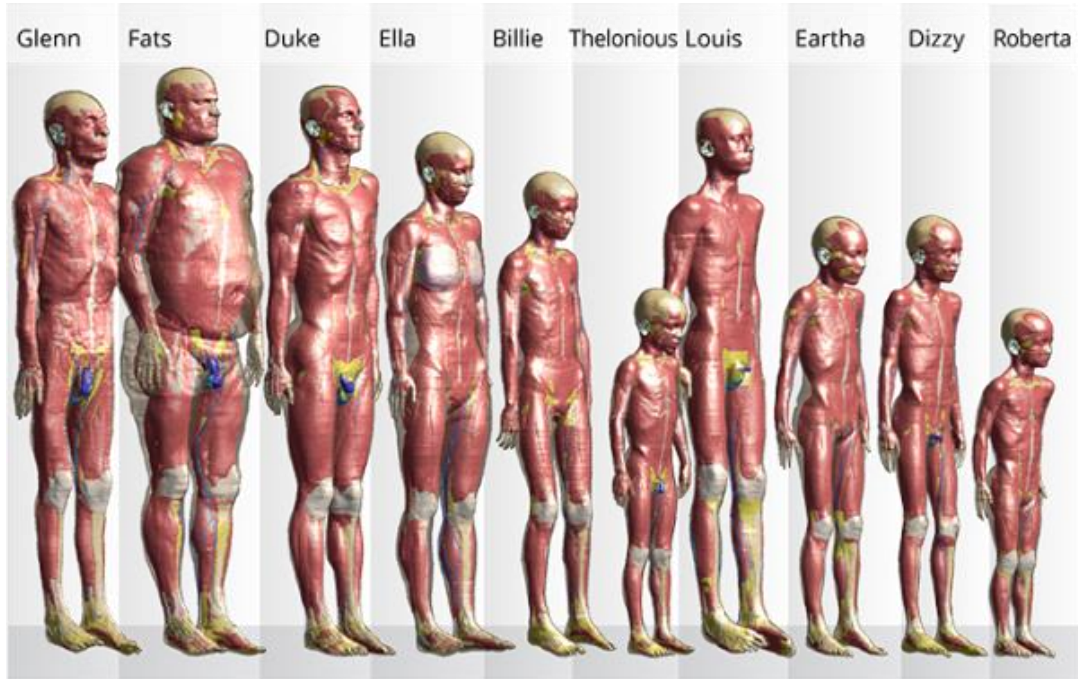


Figure 3.9: The virtual family provided by the IT'IS Foundation [136]

3.9.1 Geometry, composition and dimension

A range of shapes of phantoms is used to design implantable antennas. Nikolayev *et al.* decided to use a homogeneous spherical phantom, since the radiation pattern is less likely to be affected in terms of gain values [138]. Wainwright, on the other hand, mentions that a cubic shape is better suited to assessing thermal consequences [117] while the cylindrical phantom modelled in [139] follows the European Telecommunications Standards Institute (ETSI) recommended standard (ETSI TR 102 655 V.1.1.1 (2008-11), Annex B.3.2). Symeonidis *et al.* [140] uses a cylindrical phantom consisting of three layers of bone material to evaluate bone fractures with implanted monopole antennas. Spherical models are largely used as head phantoms [44]. Homogenous or single-layer cubic box models were used in [61, 141]. Merli simulated the effect of different body phantoms, cubic and cylindrical, and found no significant change in terms of reflection coefficients [64]. However, the shape of the simplified body model significantly affects radiation efficiency, gain and pattern [49, 100].

Homogenous models usually represent one tissue type, mostly muscle, while multilayered models consist principally of three layers, muscle, fat and skin, as seen in [7, 142]. Simple phantoms also reduce simulation times, and mean analytical procedures can be used, whereas more complex and real phantoms provide a more accurate outcome of expected radiation characteristics.

The dimensions of phantoms displayed in the literature can range from 8.5 mm to 1,000 mm in length, as summarised by Merli [Chapter 2, Table 2.3 [44]]. Implant depths also vary, depending on the application. The placement (depth) and location (head, abdomen etc.) of the antenna inside a phantom greatly affect antenna performance.

Antenna performance does not only depend on phantom and placement, but design, electrical size, biocompatible insulation and operating frequency all play their part, making choosing the phantom trickier. A comparison undertaken by Gemio *et al.* [143] shows that homogenous tissue models tend to overestimate radiation losses compared with multilayered models, thus choosing a homogenous phantom for safety reasons is preferable. Comparing single and multilayer models in terms of reflection coefficient presents some variation in the literature. Placing antennas in different tissue, such as skin or muscle, leads to a variation in reflection coefficients, depending on antenna design. For example, Soontornpipit *et al.* [144] shows a variation of 10% for two different antennas (spiral and serpentine), whereas Kim *et al.* [101] shows very small variations.

When a precise radiation pattern measurement is needed, it is essential to use an accurate human body model, since it is influenced by the phantom's shape [64].

3.10 CONCLUSION

This chapter discussed the fundamental theoretical aspects of antennas immersed in high dielectric, lossy materials, and an overview of multiple phantoms to assess the electromagnetic performance of antennas was given. Regarding the effect of human body tissues on the antenna radiation, it can be summarised that the coupling between near-field and the surrounding tissue influences the characteristic antenna parameters (radiation efficiency, pattern, power and bandwidth), which need to be evaluated to successfully design a functioning radiating antenna. The resonance frequency of the antenna is detuned by the different body tissues, the position within the body and at different orientations of the antenna system.

Maintaining the patient safety is an important aspect involved in the design of a medical telemetry system. SAR specifications help to prevent hazardous heating of the body tissue and ingestible antennas have to comply with them. A brief overview was given about skin depth and the path loss to better understand the radiation behaviour in tissues related to the SAR. Another aspect ensuring patient safety and improving the antenna radiation is to add a biocompatible insulation layer and a short overview is given involving available materials.

In order to assess the radiation performance of the Antenna Under Test (AUT), a body model for both simulations and phantom is used. Producing a real phantom is challenging, due to the dispersive dielectric properties of human body tissues. In this thesis, a single-layer model with muscle-like dielectric properties over the required frequency range was used, providing a worst-case scenario in terms of power and signal loss, since muscle has the highest permittivity and loss tangent of the tissues involved.

The gained knowledge will be applied to the design and simulation of an ingestible antenna in the following chapter.

CHAPTER 4 ANTENNA SIMULATION

A denser integration of internal electronics, due to an increased number of modalities within the capsule, leads to increasing challenges caused by the limited space available within the capsule. This makes it harder for relatively large components such as a typical helix antenna used within the Pillcam® (as seen in Figure 2.3) to fit within the capsule without reducing sensing capabilities.

Previously designed conformal antennas cover either most of the capsule surface, represent larger dimensions due to the larger size of the capsule or radiate at higher frequencies than the antenna developed in this thesis [6-8, 57, 65, 77, 145]. Liu *et al.* and Das *et al.* presented conformal antennas radiating at 2.4 GHz and 915 MHz and demonstrated their performance in simple body models, composed of a liquid mixture and minced pork respectively [57, 77]. None of the state of the art conformal ingestible antennas has yet been investigated *in-vivo* using a data transmission chip and recording temperature/SAR measurements. In the following we demonstrate the design, manufacturing and performance characterization of a helical antenna conformally placed outside an endoscopic capsule and the characterisation *in-silico*, *in-vitro* and *in-vivo* of the telemetry system in pig models.

Using the external surface of the shell allows an effective increase in antenna size. The resulting increased antenna length allows operation at a lower resonance frequency in the MHz range, offering higher radiation efficiency within high-dielectric materials, such as human body tissue. In this chapter, the design of the ingestible antenna is described, including the initial antenna design, simulation and measurements. The design steps, which were formulated in Chapter 2 (Figure 2.5), are applied. Simulations using the CST software package and its time and frequency domain solvers have been carried out to characterize the performance of the antennas. All investigated types of antenna offer a cost-effective and easy way of producing prototypes for hands-on measurements and tests.

This Chapter is organized as follows: The initial conformal antenna design is investigated in Section 4.1, including simulations and measurements and the analysis of the effect of an attached cable on the radiation performance of the antenna. In Section 4.2 the final antenna design and its optimization, including SAR simulations, is presented.

4.1 ANTENNA DEVELOPMENT

4.1.1 Initial conformal antenna design, simulation and measurements in free space

One antenna type was investigated initially to better comprehend the simulation process and the involved specifications and properties, before adding highly lossy materials, such as body phantoms and human tissue. The simulation is followed by a simple manufacturing process, offering a quick and easy method to measure the prototype and to compare simulation to the measurement results.

To get a general idea of the performance of an antenna in free space, the analysis focused on a meander shape first, since this particular design has not previously been studied, to the best of the author's knowledge. There are, however, similar meander designs, such as the new chandelier meandered design from Izdebski *et al.* [65], and the new small conformal antenna for capsule endoscopy from Alrawashdeh *et al.* [7], as mentioned in Chapter 2. The simulations were performed with the physical measurement technique in mind, so that simulation results can be validated by measurement values later on. This was important for ensuring the correct procedure for the following steps up to the final design. Figure 4.1 shows the simulated meander antenna configuration and the conformal antenna system.

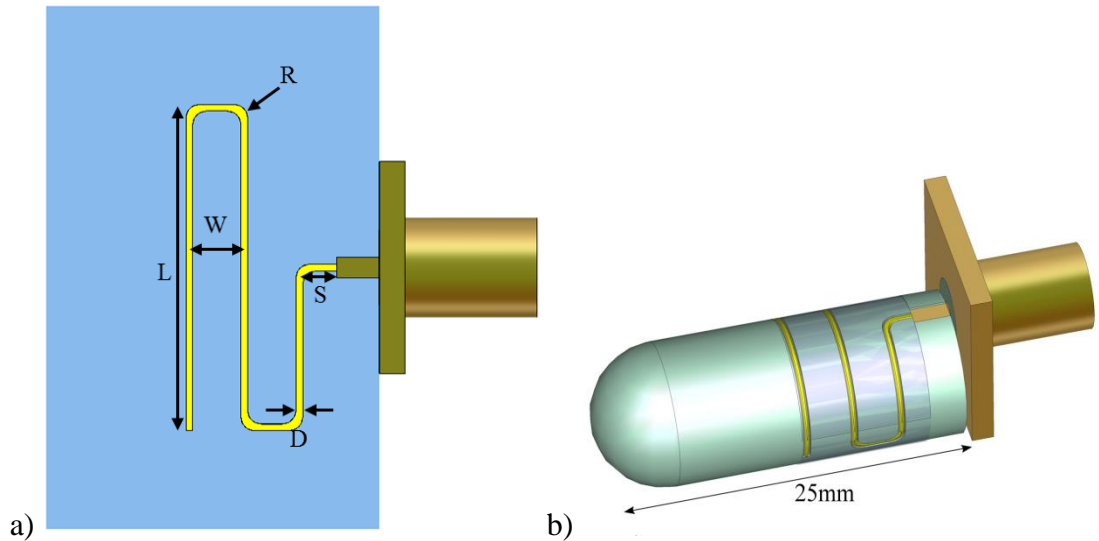


Figure 4.1: a) Meander antenna configuration ($D=0.4$ mm, $W=3.4$ mm, $L=19.6$ mm, $R=0.8$ mm, $S=2.05$ mm); b) Conformal antenna system (CST simulation)

To excite the antenna, a commercially available SubMiniature version A (SMA) connector was connected to the copper wire. The parts of the system, capsule material

and material interfaces, were incorporated into the simulation along with important material properties, such as frequency-dependent dispersive dielectric coefficients and conductivities. Optimisation sweeps were performed to find the best spacing between the individual strands and the length of the wire. Initially, to keep the antenna design simple and easy to manufacture, a single turn was chosen so that only a small part of the shell surface area was occupied. In reference to Figure 4.1, the whole antenna length is 58 mm. The calculated resonance frequency f_0 in free-space is approximately 5.17 GHz using (20):

$$f_0 = \frac{c}{\lambda} \quad (20)$$

A 3D model of the capsule (25 mm length \times 10 mm diameter) made of a photopolymer ($\epsilon_r = 2.8$, loss tangent, $\tan \delta = 0.02$), connector and a layer of LoctiteTM ($\epsilon_r = 2.42$, loss tangent $\tan \delta = 0.01$) was generated using CST, while a meandered dipole copper antenna with one turn was curved to wrap around the surface of the shell.

After optimisation of the antenna design in CST, five capsules were additively manufactured from Vero White polymer using the Stratasys Objet Connex 500. The high print resolution of the 3D printer, $42 \times 42 \mu\text{m}^2$ (600 dpi \times 600 dpi), in the x-y plane and 16 μm layer thickness along the z-axis direction allows the creation of grooves on the external surface of the capsule, which can be reliably shaped into the desired antenna geometry. The copper wire was then threaded along the meander and fixed in place using Loctite 401 adhesive. The SMA connector was attached to the base of the capsule and joined to the wire using a solder connection (Multicore 60/40 tin/lead). This ensured a good electrical contact with the antenna. To finish the fabrication process, the antenna was encapsulated with Loctite 401 to make sure it did not touch the surrounding material. Figure 4.2 shows the manufactured antenna prototype.

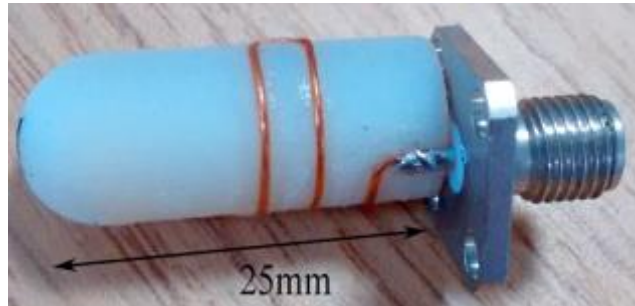


Figure 4.2: Manufactured meander antenna prototype

The frequency domain solver of the CST software was used to characterise the performance of the antenna in free-space. The antenna system was then connected to a

Vector Network Analyser 8510 (HP) and the reflection coefficient (S_{11}) measurements in free-space were carried out. Figure 4.3 shows the frequency response of the simulated antenna and of the VNA measurements.

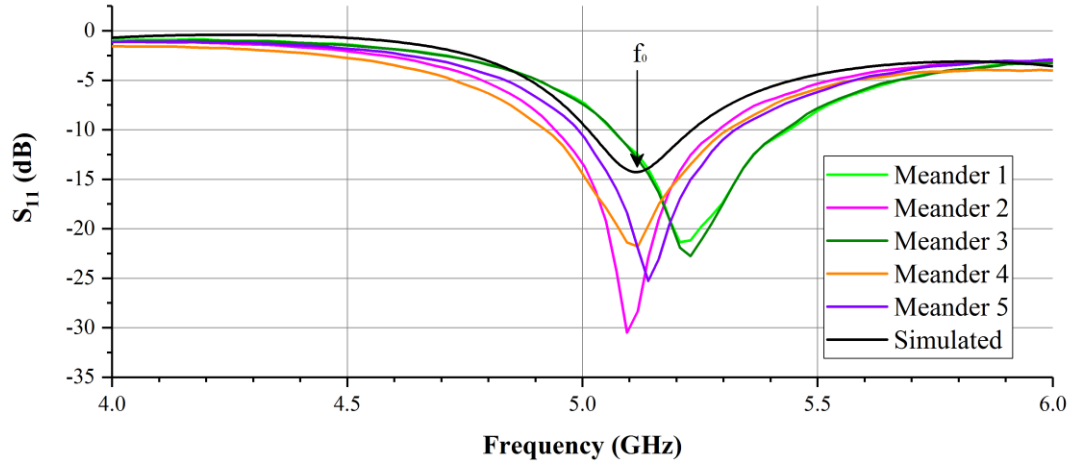


Figure 4.3: Frequency response of antenna system in free-space: Simulation and VNA measurements of 5 fabricated antennas numbered 1 to 5

The experimental measurements agree well with the simulation results in terms of resonance frequencies within an S_{11} parameter sweep. The simulated resonance frequency lies at 5.1 GHz, but the measured resonance frequencies of the different meander antenna range from 5.1 to 5.2 GHz. The measured -10 dB bandwidths of the antennas range from 300 to 370 MHz, whereas the simulated result shows a slightly lower bandwidth of 225 MHz. The simulated S_{11} parameter values and bandwidth differ from the measured results due to a possible impedance mismatch between the SMA and the antenna. This mismatch is due to the solder connection and the possibly unknown exact material properties within the simulation set-up. The S_{11} value at 5.1 GHz is -14 dB compared with -22 to -30 dB in the experimental measurements.

Figure 4.4 displays the radiation pattern of the simulated meander in free-space, including the gain and radiation efficiency. The simulated antenna has a total gain of 2.12 dBi with a directivity of 2.54 dBi. The radiation efficiency lies at -0.05 dB. The radiation pattern shows an increase in radiated power towards the rear end of the capsule, which is likely due to the attached SMA connector. The design process resulted nevertheless in a successful approach of a first antenna design. The reflection coefficient comparison of simulation and measurement show good agreement in free-space.

The next steps were:

1. To remove the bulky SMA connector
2. To change the solid capsule part to the full, hollow capsule to add electronics and additional components
3. To conduct experimental measurements of the antenna system inside a physical human tissue phantom
4. To design a helix antenna as a comparison to find an ideal antenna design
5. To choose and optimise the antenna design to achieve the required 433 MHz resonance frequency

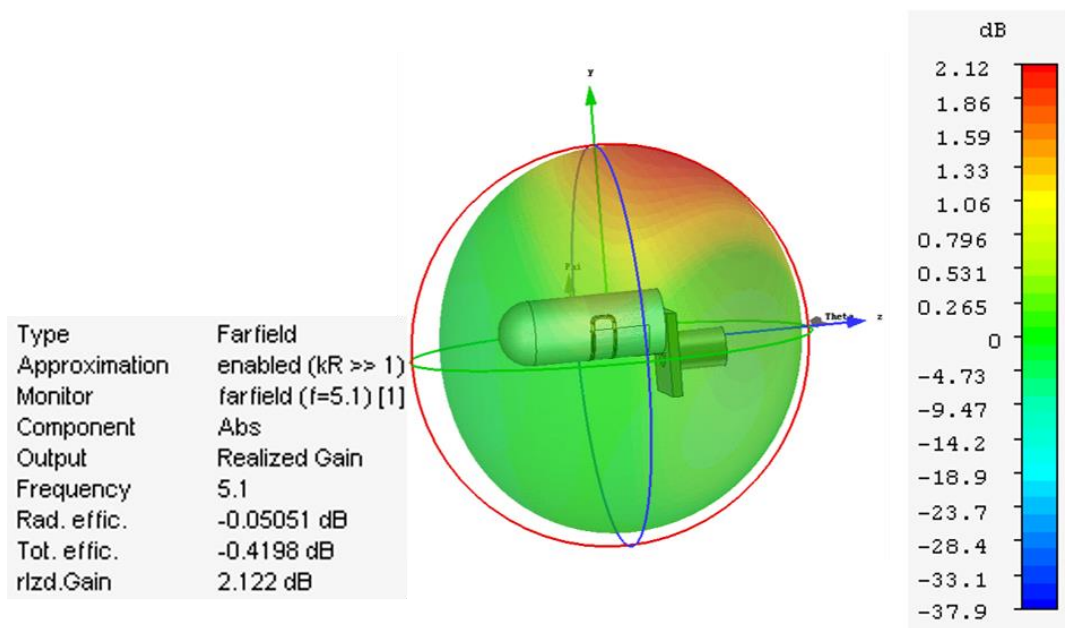


Figure 4.4: Radiation pattern, gain, radiation efficiency of meander in free-space simulation

4.1.2 Human body phantom material

Before continuing with the design of the antenna system, a body environment had to be generated to compare the antenna simulation results with experimental results obtained by testing the capsule antenna within a tissue phantom. It was also necessary to be able to reproduce the tests more than once, under the same conditions every time.

Previously, dry and liquid phantoms have been used to mimic different tissue properties as seen in [62, 137] and mentioned in Chapter 3. The phantom material used in these tests consists of a hydrophilic organic powder and degassed water (Super Stuff Bolus, RPD Inc., USA), which was mixed in a weight ratio of 6:1 (powder: water), thereby reproducing the electromagnetic properties of muscle tissue. The doughy consistency of

the phantom ensures that electronic equipment does not come into contact with any water, reducing the risk of a short circuit. Due to its gelatinous nature and low transmission frequency, a coaxial-type probe was used to evaluate the frequency-dependent complex permittivity and loss tangent of the phantom material. This ensured an accurate measurement over a wide bandwidth. Commercially available probes (e.g. Keysight N1501A dielectric probe kit) are expensive, and are often more reliable for measuring liquids and solids than gels. Measurements of the phantom dielectric properties were conducted at the National Physical Laboratory (NPL) using their custom-made coaxial sensor [146]. The measured dielectric properties are shown in Table 4.1. Muscle tissue causes the largest signal attenuation, due to its high permittivity ($\epsilon_r = 65$) at 433 MHz compared with fat ($\epsilon_r = 5.6$) or bone ($\epsilon_r = 13.1$). Therefore, it provides a worst-case scenario when investigating antenna radiation properties and channel propagation [147]. Advantages of this particular phantom include (1) its easy moulding into different shapes, (2) the possibility to simulate different tissues properties by changing water, (3) its long shelf life, and (4) the rapid and easy mode of fabrication.

TABLE 4.1: Measured dielectric properties of the phantom material

Frequency (GHz)	Real permittivity ϵ_r	Loss tangent $\tan \delta$
0.3505	66.03	0.84
0.403	65.67	0.75
0.452	65.44	0.68
0.501	65.11	0.62
0.55	64.95	0.58
0.6025	64.31	0.55
0.6515	64.16	0.51
0.7	64.08	0.48
0.753	64	0.46

4.1.3 Optimised conformal antenna designs within lossy phantom material

To further optimise the developed meander and to compare its performance, an additional helix-shaped antenna was modelled. The characteristics of both antennas were simulated to assess their performance within a human body tissue environment. The meander line monopole antenna is a new design for conformal capsule antennas, while the helix, sometimes referred to as spiral, has already been used as an internal antenna in the PillCam® and was reported in other studies, as mentioned in Chapter 2. Both designs allow the electrical length of the antenna to be extended, while ensuring

that the occupied external surface area of the capsule stays small [130]. The antennas were created from copper wire embedded into an additively manufactured capsule as previously described. A series of grooves in the shape of the meander and the helix respectively were embedded along the capsule to inlay the copper wire inside the shell of the capsule.

The helix antenna has an omnidirectional radiation pattern in free space, and previous studies have shown that the helix is less likely to be detuned in different dielectric body tissues [130]. It can be easily integrated along the pill curvature and can be designed at the required operating frequency of 433 MHz.

The 3D printed solid capsules were replaced by hollow equivalents to be able to add additional components at a later design stage. This capsule design aims to resemble the final design as much as possible. The bulky SMA connector was removed and the core of a commercially available coaxial cable with the connector removed at one end was soldered to the wire to excite the antenna and to provide the link to the VNA for further measurements. Figure 4.5 shows the helix and meander antenna configurations in CST with their respective dimensions.

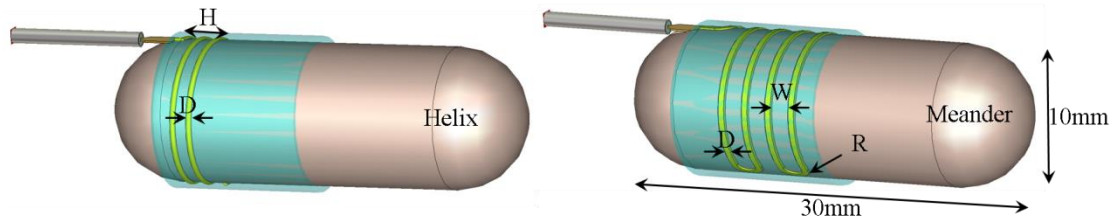


Figure 4.5: Capsule antenna configurations of the helix (left) and meander (right) (CST simulation) ($D = 0.4 \text{ mm}$; $H = 3 \text{ mm}$; $W = 1.8 \text{ mm}$; $R = 0.8 \text{ mm}$)

The 3D design of the capsule system (30 mm x 10 mm outer, 8.6 mm inner diameter) was simulated in CST. The pill consisted of a hollow photopolymer capsule ($\epsilon_r=2.8$, loss tangent, $\tan \delta=0.02$), coated with a thin, insulating layer of polyolefin ($\epsilon_r=2.3$, loss tangent $\tan \delta=0.01$), and the conformal meander line copper antenna on the external capsule surface. In reference to Figure 4.5, the wire had a diameter (D) of 0.4 mm, the width (W) was 1.8 mm and the length (L) of the long sections was 26.2 mm. The radius (R) of the corners was 0.8 mm. The helix antenna had a similar structure to that of the meander line antenna, and the same materials were used. The optimisation sweeps resulted in a final length of 84 mm, with 2.5 turns and a coil height (H) of 3 mm. The helix took up less space than the meander, with only 95 mm^2 of occupied surface area

compared with 314 mm^2 . The now optimised meander design occupied around 10 mm of the capsule length, leaving space for cameras and other modalities. The final length of the meander line antenna, excluding the attached cable, was 128.5 mm. Both systems were excited by a waveguide port which was defined at the end of a 50 mm long coax cable.

Five capsules were additively manufactured with each optimised antenna design, using VeroWhite polymer deposited by the Stratasys Objet Connex 500. The high print resolution achievable with this method ensures that the grooves guiding the copper wire produce an antenna with the correct shape and dimensions. After being guided into place, the copper wire was then fixed with a layer of heat-shrink tubing acting as an insulating layer. The coaxial cable was then soldered (Multicore 60/40 tin/lead) onto the end of each wire. Figure 4.6 shows the manufactured capsule antenna prototypes.



Figure 4.6: Manufactured prototypes (length = 30 mm; diameter = 10 mm) including insulation layer: meander (top); helix (bottom)

4.1.3.1 Simulation and measurement

The antennas were simulated within a homogeneous cubic muscle phantom model that was large enough to completely absorb the electromagnetic energy ($190 \times 190 \times 190 \text{ mm}^3$). The size of the cube was increased incrementally until no change of reflection coefficient could be observed, so that neither the size of the phantom nor its shape would influence antenna performance in terms of resonance frequency, radiation pattern and SAR. The cubic shape helped to reduce computational resources used.

The frequency-dependent dielectric properties of the materials were identified in advance by adjusting the simulation until the frequency response matched the measured results obtained using a VNA (HP, USA) in conjunction with the previously used meander antenna connected to an SMA feed as reference antenna (Section 4.1.1). The

measurement of the permittivity and loss tangent of the dielectric material was challenging due to the low frequencies and the required information over a large frequency range. The real permittivity ϵ_r and loss tangent $\tan \delta$ values can be found in Table 4.1. The magnetic permeability, μ , of the body tissue is assumed to be 1.

All parts of the system, such as the air gap caused by manufacturing tolerances between the antenna, insulation layer and cable were embedded into the simulation, to resemble the full device. Incorporating the dielectric material properties is important, since the lossy and frequency-dependent dispersive characteristics significantly influence the simulation result.

The time domain solver of the CST Microwave Studio software was used, because it offers enhanced-accuracy fast back-projection algorithm (FBPA) assistance to handle complex structures and reduces the time needed for each simulation. Frequency response measurements of the antennas within a body tissue phantom (RPD Inc. Super stuff bolus) of 280 mm diameter were obtained using a VNA. Figure 4.7 shows the antenna system set-up within a cubic single-layer phantom (190 mm long) in CST, alongside the real phantom material.



Figure 4.7: Antenna configuration in a body phantom simulation and measurement setup. The antenna capsule was covered with a second semi-spherical part of the phantom once placed in the middle of the first half

The experimental measurement results of the reflection coefficient curves agree with the simulation results, as seen in Figure 4.8. The resulting frequencies of both designs lie within the targeted ISM range. The average resonance frequencies of the meander and helical antennas are 449 MHz and 400 MHz, respectively. The difference in resonance frequency between different prototypes of the same antenna design is attributed to alignment issues during manual assembly and impedance variation due to the coaxial

connection and manufacturing tolerances of the 3D printed capsule and the antenna-to-cable connection.

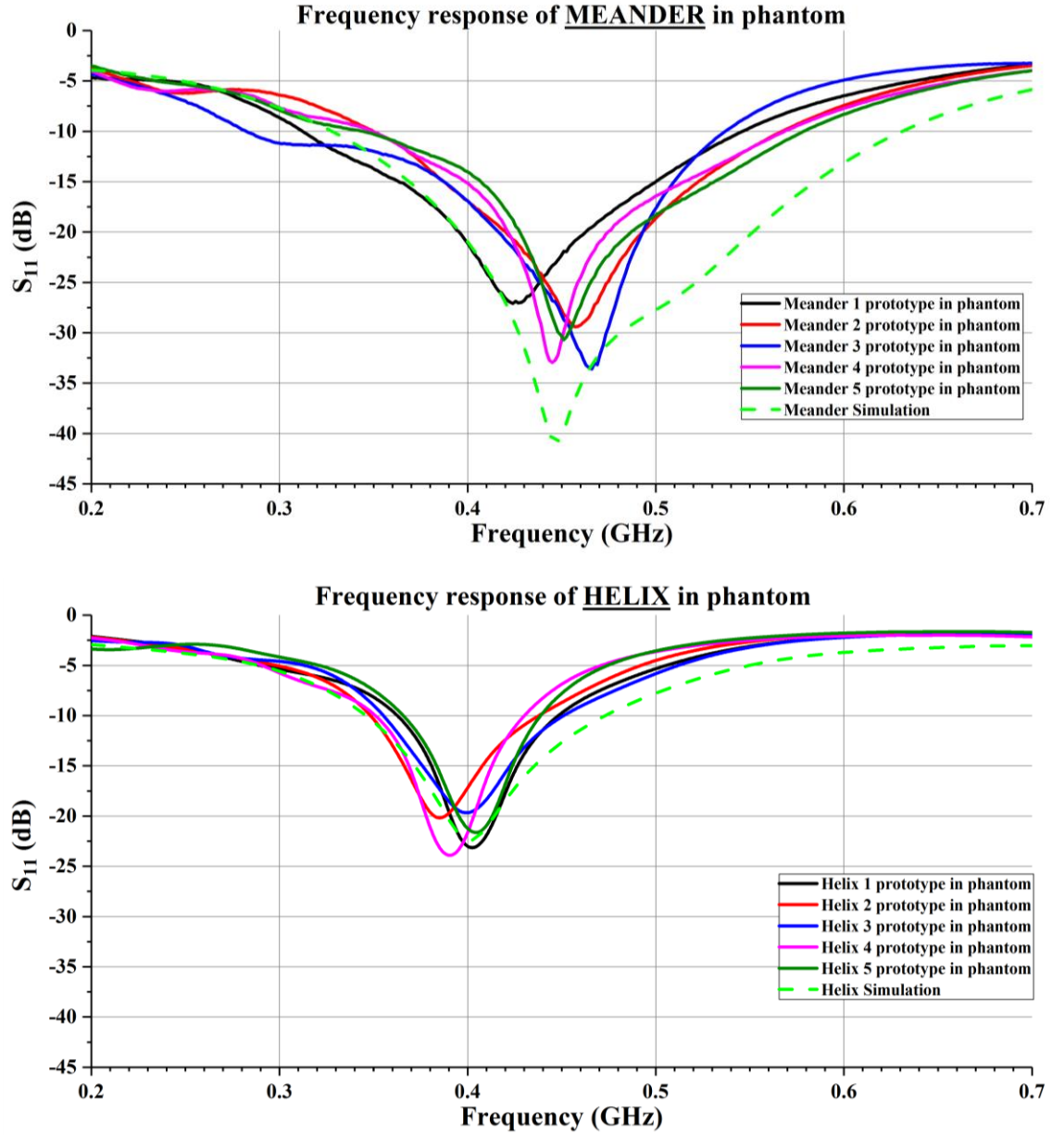


Figure 4.8: Frequency response of simulated vs. experimental meander (top) and helix (bottom) antennas in tissue phantom with muscle properties. Each antenna configuration was manufactured 5 times, numbered 1 to 5, together with a coax cable, covered by an insulation layer

The -10 dB bandwidths of the proposed prototype antennas range from an average of 231 MHz for the meander to 83 MHz for the helical antenna. The individual fractional bandwidths (BW divided by centre frequency) of 51.3% and 20.8% offer wideband characteristics, helping to maintain a reflection coefficient below -10 dB while the capsule travels through the different body materials. The configurations of both antennas display an almost omnidirectional radiation and very low radiation efficiencies of 0.09% (meander) and 0.004% (helix) for total gain values of -28 dBi and -41 dBi

respectively, which are common in ingestible antenna systems [44, 105]. The radiation pattern is affected by the geometry of the surrounding medium and will therefore never be fully spherical within the body [44].

4.1.3.2 Cable effect

The desired resonance frequency observed in the simulation was only achieved when the connected cable was embedded by 5 cm into the phantom, together with the capsule. When the cable length was immersed into the phantom, the resonance began to shift out of the frequency range.

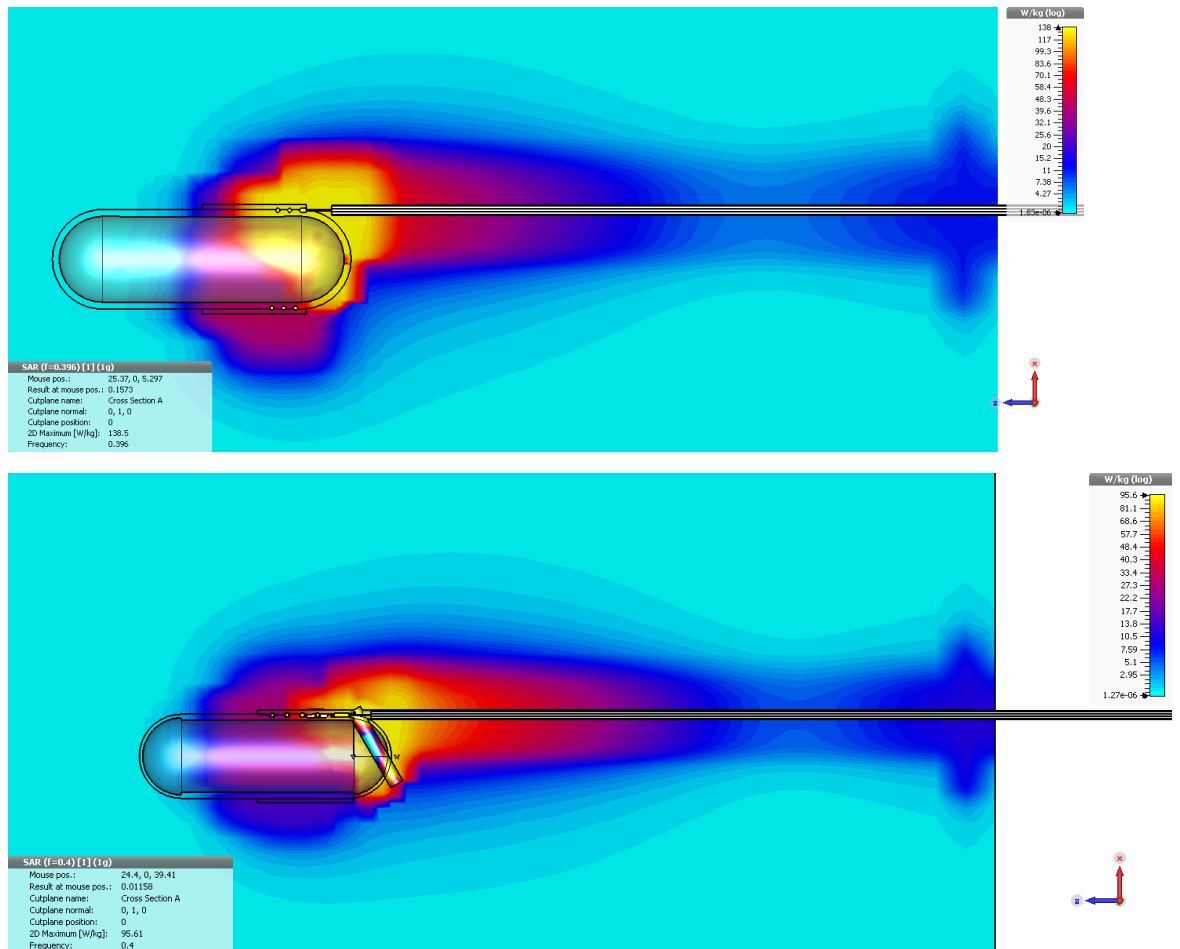


Figure 4.9: SAR simulation of helix (top) and meander (bottom) system, visualising the radiation along the attached cable. The cable is extending the length of the antenna and when removed, the resonance frequency will be higher.

When observing the SAR simulation of the full set-up, some radiation is visible along the connected cable, as seen in Figure 4.9. The connected coax cable influences the transmission, and is probably affecting the individual resonance of both antennas. It is part of the antenna itself, and extends the conducting length of it, therefore contributing to the radiation and shifting the frequency down [100]. Currents flow along the outside

the coaxial cable as it is an unbalanced feedline, and can radiate from the feedline into nearby electronics. This current is also called ‘common-mode’ current [148]. The effect of the cable was previously reported by Merli, and its influence simulated. Merli suggests de-embedding the cable in the case of ESAs radiating in the MHz range [64].

4.1.3.3 Summary of the antenna development

After fabricating and measuring the prototypes, it was observed that the helical antenna was more resistant to the detuning caused by structural changes during the assembly process and the cable effect than the meander line antenna. This can be seen in the variation in resonance frequencies in the frequency response graphs shown in Figure 4.8. The meander line antenna has a wider bandwidth than the helical antenna, and a higher gain and efficiency, but occupies more space on the capsule shell. Further work is needed to determine whether the low efficiencies achieved by both antenna configurations are still high enough to transmit signals to an external receiver for a wireless endoscopic capsule application. As for the helix, this will be treated in Chapters 6 and 7.

The simulation and measurements showed good agreement and display wide fractional bandwidths of 51.3% and 20.8% for high data rates under variable conditions. The omnidirectional radiation and the small size of the structures provide a good tool for data transmission in capsule endoscopy. The achieved resonance frequencies are not purely the result of the actual copper antenna length. The connected cable extends the length of the antenna and helps to shift the frequency to the desired MHz range. Considering the final device will be wireless, the removal of the cable would shorten the radiator length and shift the resonance frequency to a higher frequency in the GHz range. Therefore, the length of the radiating antenna needs to be adjusted.

The simulations and all their settings (material properties, etc.) agreed with the measurements, simplifying the next steps of the design process. In the future application described in Section 4.2, the antenna will be directly connected to the internal transmitter PCB, which will include a GND plane. When detaching the cable and adding a GND plane, a different feed port can be used. The next investigation step described in Section 4.2, will involve greater system integration by adding an internal Printed Circuit Board (PCB) with integrated microcontroller, transceiver and power supply to test the data transfer within tissue phantoms before progressing towards

translational trials. Replacing the current polyolefin sheath with a biocompatible coating is described in Section 4.2.

4.2 FINAL HELIX ANTENNA DESIGN

In the final step, the SMA cable was removed. The meander and helix antenna were both optimised, matching the conductor length to achieve 433 MHz within muscle tissue. The meander, however, increased the size of the antenna so much that the planned ultrasound array could not be embedded, since it covers almost the whole capsule shell. The helix, on the other hand, only occupies half of the capsule when radiating at 433 MHz.

Although the meander seemed to have a larger bandwidth (50 MHz) than the helix (20 MHz), the work was continued on the helix design only, due to time restrictions. For future work, slightly different meander designs could be developed to satisfy the desired size and performance restrictions. The flowchart in Figure 4.10 below gives a brief overview of the simulation and optimisation process:

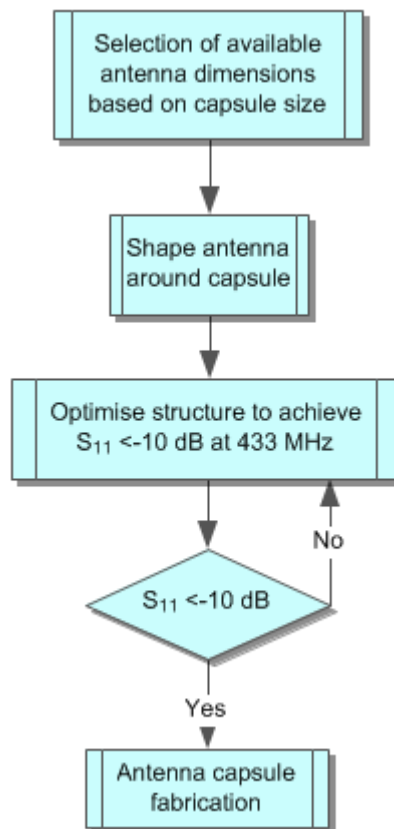


Figure 4.10: Simulation and optimisation process of the final antenna design

4.2.1 Simulation set-up and optimisation

Figure 4.11 shows the simulation set-up of the proposed final antenna design. Part of this set-up involved the parallel development of the internal electronics, which is explained in Chapter 5. All parts of the system, apart from the influence of the attached power and signal tethers, were considered in the simulation, including the connection of the antenna to the internal ground (GND) plane and the external insulation layer. The dielectric properties of all materials were measured prior to the simulations to integrate their lossy and frequency-dependent dispersive characteristics, which significantly influenced the simulation results.

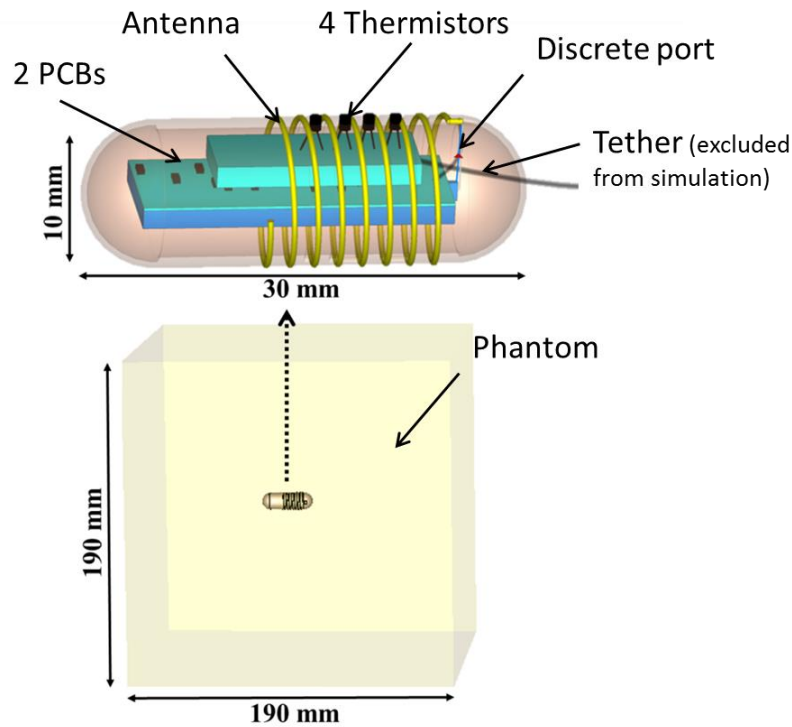


Figure 4.11: Simulation set-up of the helix antenna system within a cubic muscle tissue model

A discrete port was selected to feed the antenna and the frequency solver. The mesh cell adaptation was turned off so that the number of mesh cells did not increase too much. 2.89 Million cells were found to be the smallest necessary for accurate results. Field monitors (far-field, loss) at 433 MHz were set, in order to visualise the radiation pattern, surface current and power loss density as 2D/3D results. Post-processing settings and evaluations provided an overview of the expectable SAR values.

Using the optimisation tools from CST (Trust Region Framework Algorithm in ‘Optimiser’ setting), the optimal length of the antenna was found to be 7.75 turns made of 400 μm diameter copper wire, with a pitch of 1.6 mm and a radius of 4.8 mm. This is

equivalent to a wire length of 234 mm and helix height of 12.5 mm, respectively. Thus, more than half of the capsule area is available to integrate other modalities such as cameras and sensors.

4.2.2 Simulation results

The antenna has a wide bandwidth of 20 MHz, consistent over a wide variety of tissue types [43], and later shown in Figure 4.15. Figure 4.12 shows the frequency response of the helix in free-space:

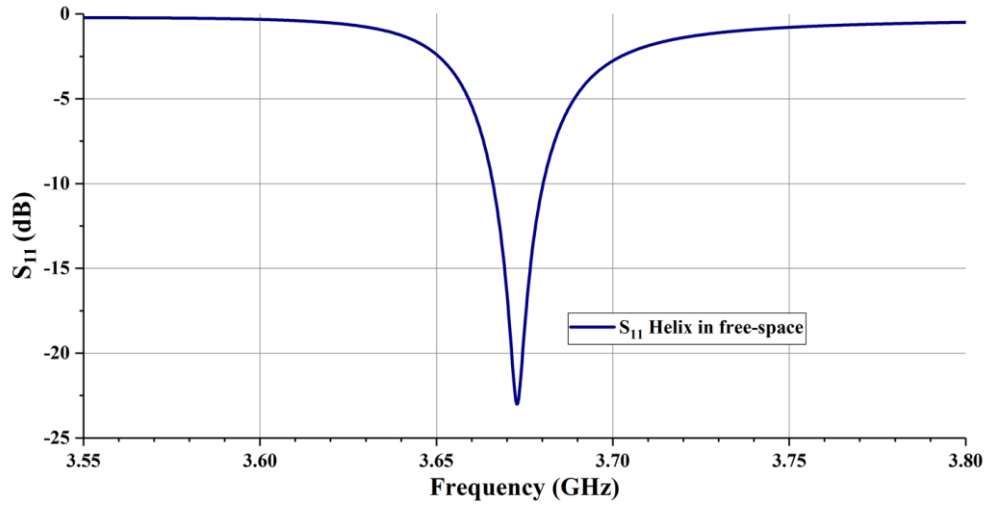


Figure 4.12: Helix S_{11} simulation in free-space

The resonance frequency is 3.67 GHz. Using the equation (21)

$$f' = \frac{f_0}{\sqrt{\epsilon\mu}} \quad (21)$$

with a relative permittivity ϵ_r of 64, and a relative permeability μ of 1 for muscle, a frequency of 0.459 GHz is calculated, giving us the estimated resonance frequency within a muscle tissue environment. This equation does not take into account the frequency-dependent material dispersion, and therefore only gives an approximation of the frequency shift. The simulated frequency of 433 MHz is lower than the calculated one, as shown in Figure 4.13.

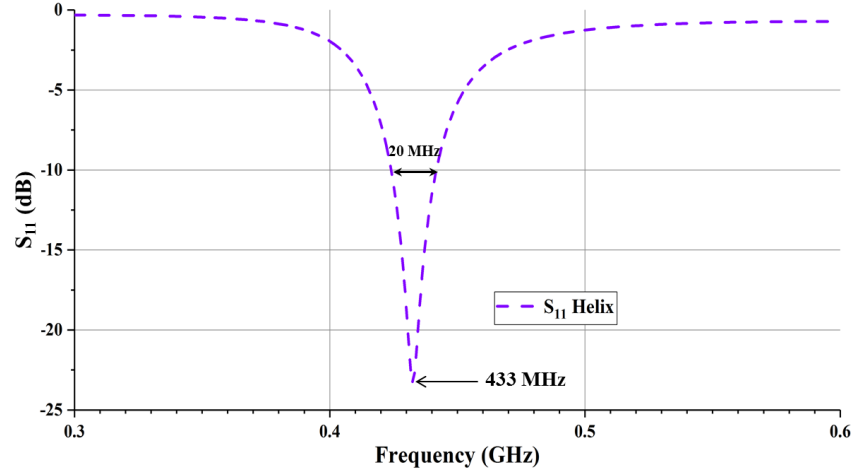


Figure 4.13: Helix S_{11} simulation result in muscle tissue phantom

The simulated radiation pattern of the antenna system, including the gain and radiation efficiency, is shown in Figure 4.14. The simulated antenna has a total gain of -40.9 dBi, with an almost omnidirectional radiation pattern, and a low efficiency of -41.2 dB, which is due to the large electromagnetic absorption by the human body [67].

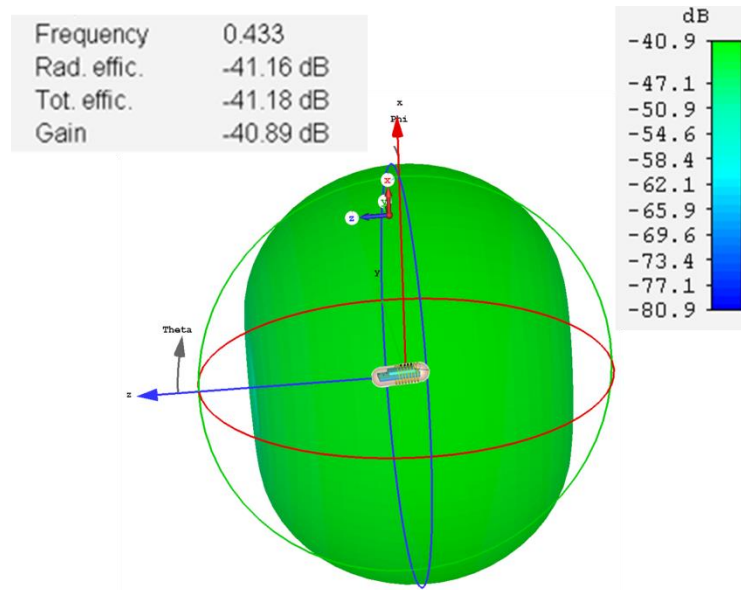


Figure 4.14: Radiation pattern of helix within phantom

Figure 4.15 shows the simulated resonance frequencies of the helix antenna embedded within the phantom that was used, compared with the skin, fat and muscle tissues CST provided. Since fat has a much lower relative permittivity ($\epsilon_r = 5.6$) and lower losses compared with phantom, skin and muscle tissue, the frequency is much higher

(554 MHz), and the bandwidth is much wider (50 MHz), as previously explained in Section 3.1.1 and 3.1.5.

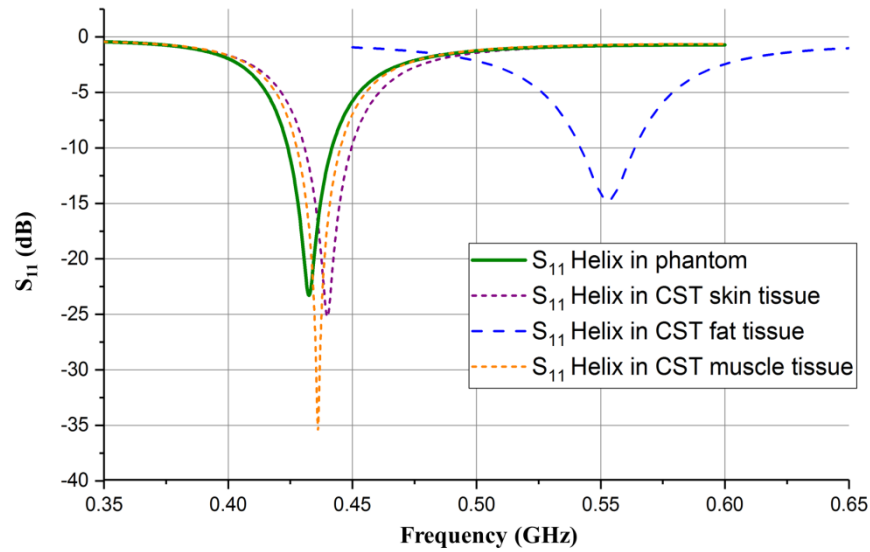


Figure 4.15: Simulated S_{11} comparison of helix antenna in skin, fat, and muscle material as well as the phantom material used. A clear shift in frequencies is visible, which is depending on the surrounding tissue.

Figure 4.16 shows the comparison between the simulated resonance frequencies of the full antenna system with the connected and disconnected internal GND plane, and the measured resonant frequency of the fabricated prototype within the phantom using a Programmable Network Analyser (PNA) N5225A (Agilent, USA). The GND plane is placed longitudinally inside the shell. In the assembled device, the antenna is connected to the centre-pin of the micro-SMA connector mounted on the PCB, while the GND is

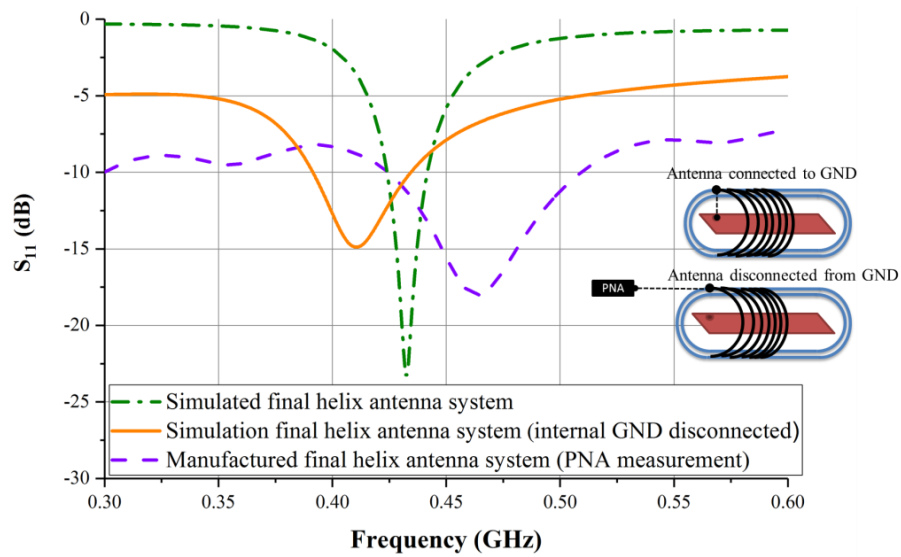


Figure 4.16: Full antenna system with connected and disconnected internal GND plane, and the measured resonant frequency of the fabricated prototype within the phantom. When the GND is disconnected from the antenna, losses are increased and resonance frequency shifts

connected to the outer shield of an SMA cable.

The antenna, when measured, was not connected to the assembled PCB system, since it was not possible to attach the PNA cable to the PCB. The simulated resonance frequency of the full system shows that it lies within the targeted ISM band at 433 MHz with a bandwidth of 20 MHz. This wide bandwidth characteristic helps to maintain a reflection coefficient below -10 dB while the capsule is travelling through different body tissues. When the GND in the simulation is disconnected, the frequency shifts down by 20 MHz. The measured device disconnected from the GND plane shows a shift to a higher frequency of 20 MHz. The difference in the S_{11} response between the simulated and measured results can be primarily attributed to two effects. In order to measure the response of the antenna, an additional SMA connector and a short coaxial cable (2 cm) have been added for obtaining the measurements from the PNA. The parasitics of the coaxial cable and the SMA could have contributed for the shift in the resonance frequency. This effect has also been noticed in a similar study in [64]. In addition the measurements with the PNA have been performed with the ground plane of the helix removed. It is known that the transmission and radiation modes of a helix antenna can vary depending on the geometry of the helix and these effective geometry parameters in turn depend on the effective dielectric properties of the phantom material. The effective dielectric properties of the tissues have been known to change depending on the condition of the porcine [149]. The coaxial cable geometry along with the helix could have contributed for the occurrence of combination of transmission and radiation modes, thereby increasing the measured effective bandwidth of the helix antenna. Differences between the simulation in terms of resonance frequency and bandwidth are due to the disconnection of the GND plane for our measurements. Attention should be drawn to the offset of the reflection coefficient (< 0 dB), which is due to the lack of the GND plane connection. In this case, most of the power was not radiated, but returned to the antenna system.

4.2.2.1 SAR

The electromagnetic radiation from the antenna must not heat local tissue more than 1°C above nominal core temperature [13] and it must comply with patient safety standards and regulatory requirements such as the IEEE C95.1-2005 [14]. Thermal transfer measurements were used as an indication of the Specific Absorption Rate (SAR), which should not exceed 1.6 W/kg for 1 g of tissue mass [14, 150]. SAR is a

measure of the rate at which the tissue absorbs energy when exposed to an RF electromagnetic field. Interaction of electromagnetic fields with biological tissue at MHz frequencies can cause thermal effects, due to the absorption of energy within the high-dielectric tissue. Ingestible antennas near human tissues can be a hazard when excited, therefore embedded thermistors were used to monitor any thermal effects. Simulations have also shown that the glass encapsulating the Negative Temperature Coefficient (NTC) thermistors and embedded into the capsule shell did not significantly affect antenna performance, and can therefore be ignored in future simulations. Figure 4.17 shows the SAR distribution of the simulated antenna system.

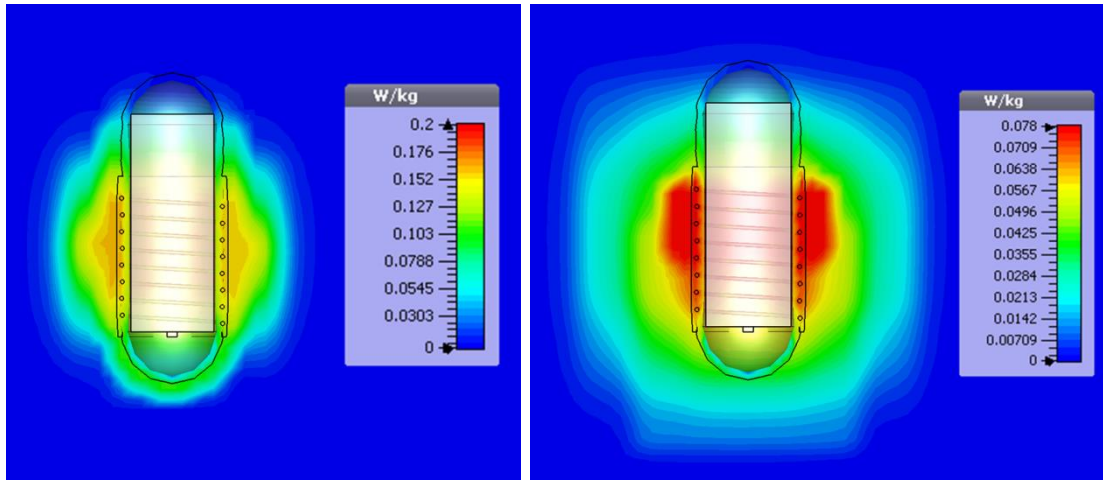


Figure 4.17: SAR distribution of the simulated antenna system embedded into phantom: max. SAR for 1 g of mass (left) and 10 g of mass (right) with 1 mW input power

The maximum possible power delivered to the antenna is 8 mW for an exposure limit of 1.6 W/kg and is 25.6 mW for a SAR limit of 2 W/kg. The highest input power of 10 mW, used for the developed telemetry system in this thesis, complies therefore with the SAR limitations.

4.2.3 Summary

The final conformal helix design was simulated within muscle phantom material, together with the internal GND plane and thermistors, and optimised to radiate at 433 MHz with a bandwidth of 20 MHz. It features an almost omnidirectional radiation pattern, and a low total gain and efficiency, which is typical for implantable and ingestible medical devices. The resonance frequency can shift depending on what type of tissue is surrounding the antenna. The largest shift of 120 MHz occurs when the tissue changes from muscle to fat.

The final device was fabricated and the antenna was measured using a PNA. Comparing simulated and measured results presented a slight offset concerning the resonance frequency, due to the measured antenna being disconnected from the internal GND plane.

Finally, the SAR simulations demonstrate values staying below the recommended SAR limits. The power delivered to the antenna can be 8 mW for the limit of 1.6 W/kg or 25.6 mW for the limit of 2 W/kg.

The realisation of the telemetry system is described in the following chapter.

CHAPTER 5 PACKAGING

This chapter deals with the packaging of the radiator to establish a complete ingestible capsule prototype. The packaging involves the manufacturing of the capsules and their integration with the necessary electronic components, including the RF transceiver, PCBs and thermistors. All the elements fit into the 3D printed housing. The final section covers the procedure of coating the capsule with a biocompatible layer. Figure 5.1 shows the design and manufacturing process of the telemetry system. The full system was connected to a tether bundle, which supplied power and retrieved the temperature data. The process is described in detail in the following sections. Section 5.1 describes the telemetry system assembly, involving the PCB design of the transceiver system and the setup of the data transmission program. Section 5.2 gives a step-by-step description of the moulding and epoxy coating process and Section 5.3 completes this chapter with a summary.

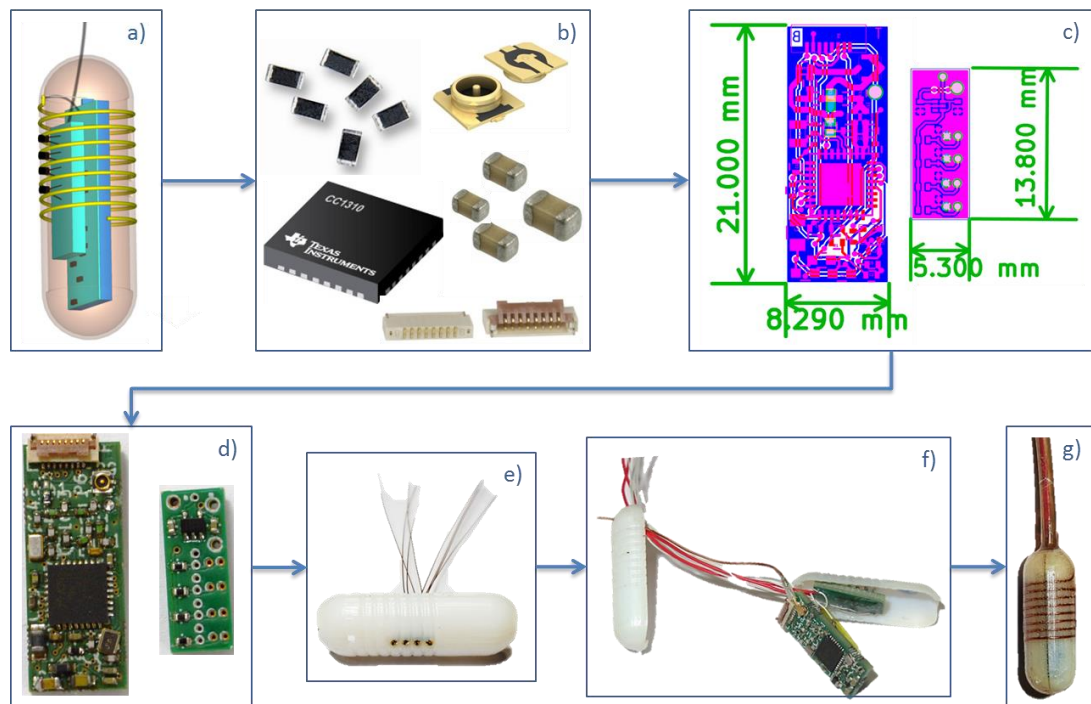


Figure 5.1: Transceiver system design process: a) Simulation of antenna system; b) Selection of system components (transceiver chip and additional electronic components according to reference design, plus antenna and programmable interconnects); c) PCB design of RF and thermistor board with open source programme KiCad Electronic Design Automation (EDA); d) Manufacture of boards and connection of electronic components; e) Attachment of NTC thermistors to the designated holes; f) Linking of boards, NTC circuit and tether connection; g) Antenna assembly, followed by the epoxy and parylene coating process (described in Section 5.2) and the connection to the PC's User Interface (UI)

5.1 TELEMETRY SYSTEM ASSEMBLY

Six capsule shells of 10 mm diameter and 30 mm in length were produced using VeroWhite polymer and the Polyjet additive manufacturing process on a Stratasys Objet500 Connex. The high print resolution of 600 dpi \times 600 dpi ($42 \times 42 \mu\text{m}^2$) in the x-y plane and 16 μm layer thickness along the z-axis direction allows the grooves created along the capsule's external surface to be reliably shaped into the desired antenna geometry as previously explained in Chapter 4. The wire was fixed in place using Loctite 401 adhesive. The internal diameter of the capsule was 8.5 mm to accommodate the PCBs made of FR-4 material, shown in Figure 5.2, and containing the electronic system for operating the antenna.

A 3 mm diameter opening was present at one end of the capsule shell so the tether could be attached, as seen in Figure 5.3. Due to space limitations and to reduce complexity, the temperature data was not transmitted wirelessly, but via a tether bundle, connected to an external data logging system. The use of a 3 m long tether meant that the capsule could be retrieved after the *in-vivo* studies had been completed and power could be transmitted without integrated batteries.

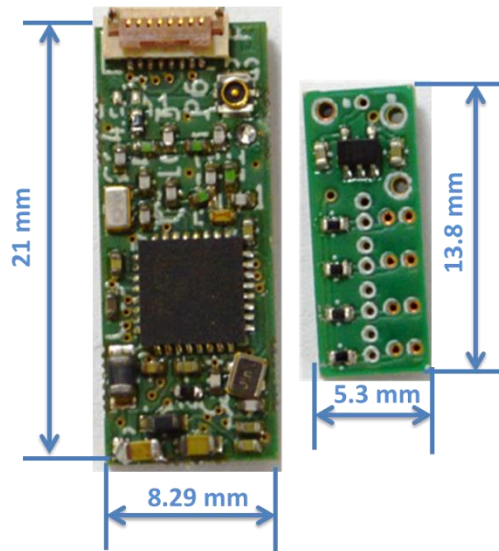


Figure 5.2: Two internal PCBs were manufactured: RF board (left) has the MCU and transmission line embedded and the thermistor board (right) connects to the power supply and the on-board thermistors

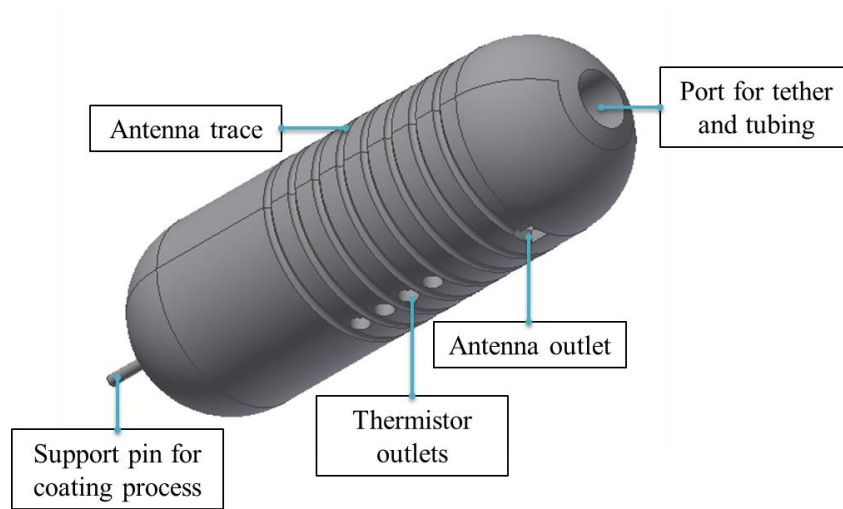


Figure 5.3: Computer model of the 3D printed capsule shell

5.1.1 Transceiver

The typical frame rate of CE devices is around two to six frames per second (fps), although many new devices such as the PillCam COLON2 can operate at 35 fps, thanks to the use of video compression and adaptive frame rate techniques [20, 26, 27, 151]. The frame size itself varies from 256×256 pixels to 1920×1080 pixels comprising 192 kB to 3,000 kB with 8-bit RGB colour depth [20, 23-25], depending on the imaging system used. Hence the approximate bandwidth of these capsule endoscopes ranges from 231 kHz to 2,341 kHz. The data rate ranges from 2 Mbps to 4 Mbps for very high data transmission. The data transmission rate must not be affected by changes in orientation, since the capsule travels through the GI tract via peristaltic motion - nor should it be affected by the heterogeneous nature of the tissue the signal propagates through.

Bearing this in mind, the transceiver chosen to control the system was an ARM® Cortex® M3-based wireless Microcontroller (MC) combined with an ultra-low power RF transceiver (CC1310, Texas Instruments (TI), USA), since it supports the required frequency bands and comes in small packages (4×4 , 5×5 or 7×7 mm²). The selected 5×5 mm² Microcontroller Unit (MCU) provides 32 pins, of which 15 are General Purpose Input/Output (GPIO) pins, with two unbalanced output pins leading to the transmission line circuit consisting of a 50 Ω impedance matching circuit. The pinout diagram is shown in Figure 5.4. The CC1310 operates within the necessary Sub-1 GHz RF bands and low current and power consumption modes, making it a useful device for future battery- powered solutions. The 2-Pin Compact Joint Test Action Group (cJTAG)

and JTAG Debugging interfaces feature a standard way of programing the MCU with the supplied programmes from TI. Finally, the high data rate of a maximum 4 Mbps and a programmable transmit output power of up to 15 dBm allow the wireless transmission of data for the ingestible capsule prototype experiments.

The main components and connections include the JTAG connection used to transfer the programme from the Code Composer Studio (CCS) provided by TI to the MCU, a 24 MHz and a 32 kHz crystal oscillator (Murata, Japan and AVX, USA) and finally the transmission line circuit (highlighted in orange in Figure 5.5) ending at the micro-SMA connector (JSC receptacle, Murata, Japan and AVX, USA).

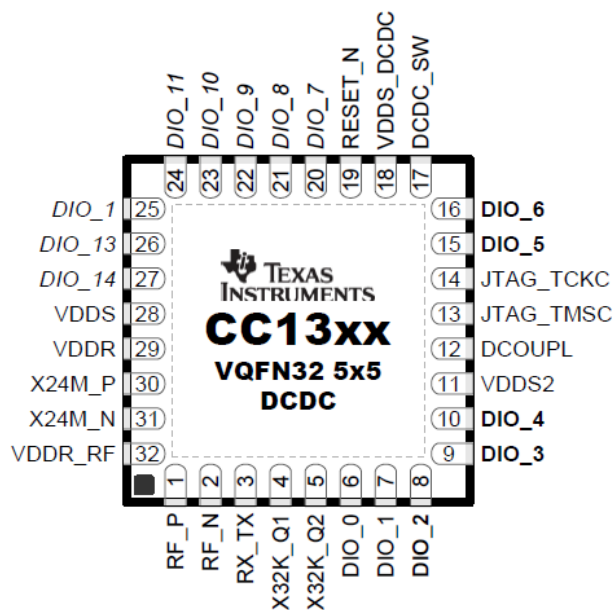


Figure 5.4:CC1310 RHB (5-mm × 5-mm) pinout, 0.5-mm pitch [152]

TI generally offers a very good documentation of its products and provides evaluation modules for most of their chips. This helped to speed up the design and testing process of the transceiver system. Table 5.1 summarises the required specifications for the transmitter choice.

TABLE 5.1: Required specifications of transmitters for CE

Transmitter requirements/considerations	
Frequency of operation	433 MHz
Output power level	≈ 15 dBm
Min. Data rate	100 kbps
Low power consumption	<10 mW
Digital Modulation	FSK modes
Sensitivity	≈ -95 dBm
Power amplification needed	No
Voltage regulator needed	None, if possible

5.1.2 PCB design

The reference design for the TI device and application notes for the CC1310 recommended a four-layer PCB stack-up, consisting of signal, GND, power and a GND/signal layer to achieve a $50\ \Omega$ match to the transmission line. The power lines should be on the power layer and all passive components on the top layer, with signal lines on top and bottom. Vias were also recommended to connect the signal to the GND layers. A $50\ \Omega$ impedance transmission line on a 1.596 mm PCB board with a track width of 0.15 mm and 0.3 mm and a PCB stack of four layers would ensure the antenna worked under ideal conditions. However, this design was not possible due to the high manufacturing costs.

Therefore, the design had to be changed. Figure 5.5 shows the system schematic of both PCB boards, together with the final manufactured transceiver system (manufactured by EuroCircuits, Belgium). The track width of the transmission line was changed to 0.5 mm to achieve the suggested $50\ \Omega$ impedance as far as was possible. The PCB stack was reduced to two layers, with the track dimensions and directions altered and some of the passive electronic components substituted to smaller components, while keeping the same electrical properties. The size of the Surface Mount Devices (SMD) ranges from 0402 to 0603 ($0.4 \times 0.2\ \text{mm}^2$ and $0.6 \times 0.3\ \text{mm}^2$), with 0402 being the smallest possible size available at Heriot-Watt University for manual assembly. The tracks could only be placed on the front and back of each board due to manufacturing limitations, which led to space restrictions for the track routing and component placements.

It is not an easy task to achieve the correct matching of $50\ \Omega$ to obtain maximum power transfer, even if a reference design is provided. The RF section is very sensitive to any changes. For this MCU, a Balanced-to-Unbalanced Transformer (BALUN) consisting of an LC circuit was recommended to change the unbalanced line and produce a balanced operation. A single BALUN component (Johanson Technology Inc, USA) was available for different frequency bands, but not for this specific design and frequency. Instead, an LC circuit and matching network to connect to the antenna was used, followed by the filter and antenna-matching circuit, as shown in Figure 5.6.

The PCB production guidelines, ranging from minimum via diameter of 0.45 mm and minimum distance of tracks and footprints to the edge of 0.25 mm, caused space constraints and limited PCB and matching network optimisation. The simulation of the final transmission line design, from MCU to micro-SMA (marked in orange in Figure 5.5), performed with the Advanced Design System (ADS) software showed a final impedance of $58\ \Omega$, which was an acceptable result for the antenna to work at the required frequency band.

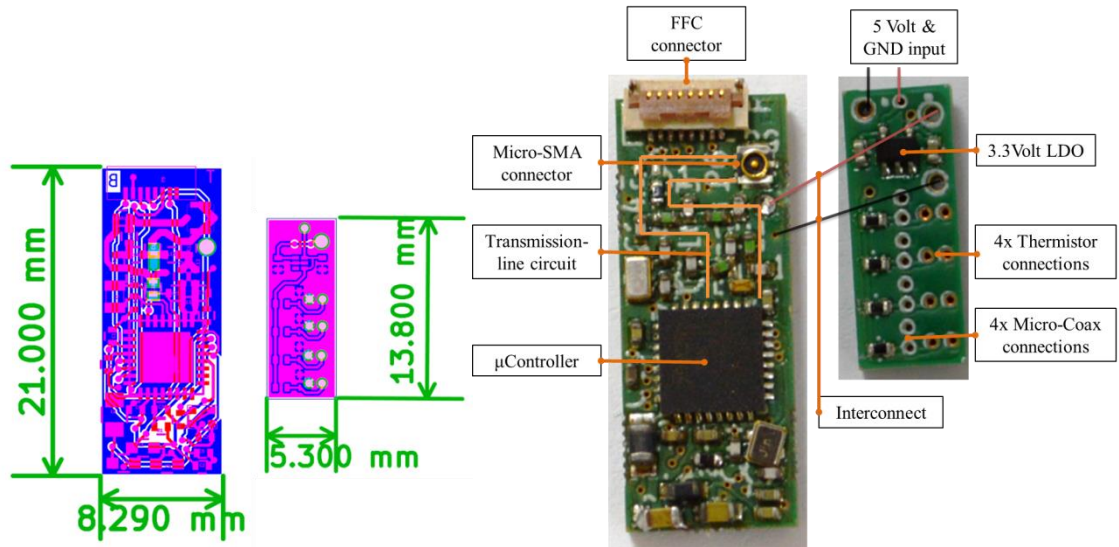


Figure 5.5: System schematic of both PCB boards (left); manufactured and assembled PCB boards (right)

5.1.2.1 Circuit assembly

Two PCBs per capsule were designed. The RF board ($8.29 \times 21 \times 1.54\ \text{mm}^3$) contained the antenna connection, matching network and programmable MCU. The thermistor board ($5.3 \times 13.8 \times 1.54\ \text{mm}^3$) comprised the Low Dropout (LDO) Voltage regulator (ON Semiconductor, USA), which converted the 5 V supplied via the tether to 3.3 V, thermistor circuit connections and power supply. A Light Emitting Diode (LED) was

mounted on the rear side of the RF board and connected to one MCU output. This allowed the successful programme transfer from the PC to the MCU to be tested.

Some components had to be soldered manually (SMD291AX10 solder paste, Chip Quik, US), but most were soldered with the help of a stencil from the PCB manufacturing company (EuroCircuits, Belgium) and a reflow oven (Heriot-Watt University).

Wireless connectivity is important to maintain the overall versatility of the endoscopic capsule [150]. However, the transceiver system introduced in this thesis was tethered to enable the power supply needed to operate the MCU, and to retrieve the capsule, while still maintaining wireless data transmission. The tether bundle consisted of four 42 AWG micro-coax cables and two 30 AWG single-core cables (all from AlphaWire, USA), which were inserted into biocompatible Teflon tubing of inner diameter 3 mm and outer diameter 4 mm (Adtech, USA), to help to stabilise the weak connections. The single-core cable was used for power transmission, while the micro-coaxial cable was used for temperature data transmission. Figure 5.7 shows the cable connections of the PCBs.

Tensile tests of the capsule-teflon tubing connection were performed to determine failure of the connection. A dummy capsule was held in the machine (Instron 3367, USA) and pulled apart at a rate of 1 mm/min. The maximum stress before detachment of the Teflon tube was measured to be 1 MPa, which is much higher than the maximum measured retrieval tension of 0.17 MPa acting on the tether during the *in-vivo* experiments.

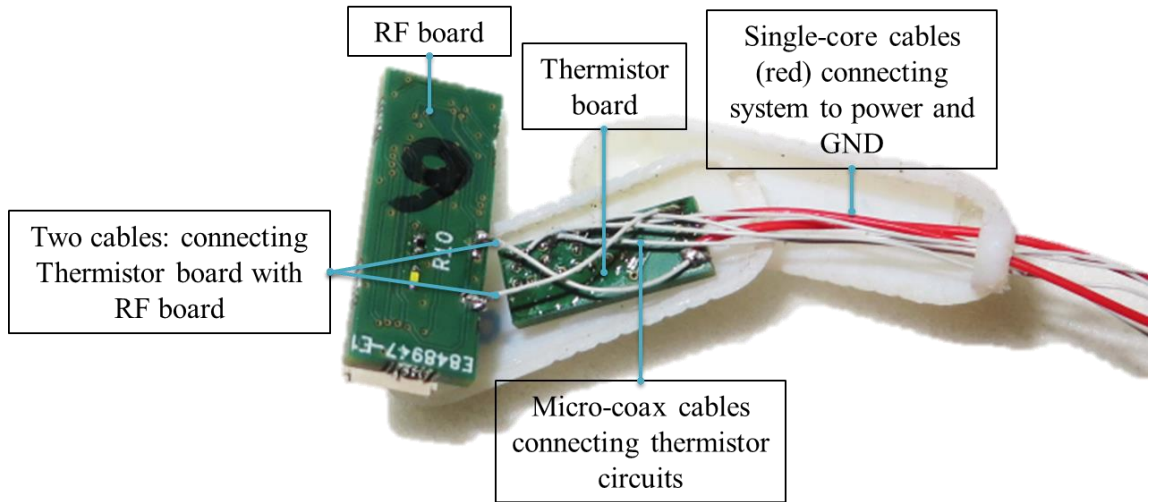


Figure 5.7: Interconnections of both PCBs and tether connections

After gluing the four NTC thermistors (B57540G1 from TDK Group, Japan) into the matching holes located in the capsule shell between the antenna tracks using adhesive EP42HT-2Med (Masterbond, USA), each thermistor leg was soldered to the thermistor circuit together with one micro-coaxial cable for each thermistor. The coaxial cables consisted of a GND sheath and seven internal conductive strands, which were separated and soldered to the corresponding solder patches of the thermistor circuit (voltage divider circuit).

One single-core wire was soldered to the input of the LDO and another, which acted as a GND cable, to a GND pad on the thermistor board. The RF board was connected with two pieces of micro-coaxial cables to the thermistor board. One connection linked the output of the LDO to the power input of the MCU, while the second cable joined the GND connection. The enamelled copper wire antenna (diameter 0.4 mm) (Block, USA) was soldered to a micro SMA cable (Murata Manufacturing Co Ltd, Japan), which was then attached to the matching micro-SMA connector (type JSC series), shown in Figure 5.8.

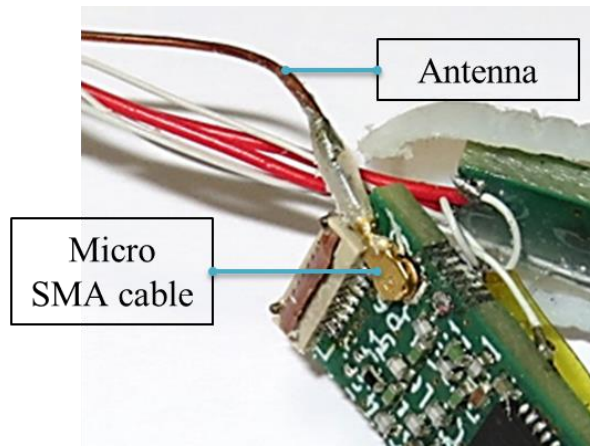


Figure 5.8: Antenna connection via a micro SMA cable

After the PCBs had been assembled, both parts of the capsule were aligned and sealed using EP42HT-2Med, a USP Class VI biocompatible epoxy (Master Bond Inc, USA). After curing, the copper wire was threaded along the grooves of the shell to create the antenna. The capsules were then coated to avoid any leaks and to fix the tubing in place using the same biocompatible epoxy mentioned previously. In addition, this epoxy layer helps reduce the SAR and the power that the body absorbs [107]. The coating process is described in Section 5.2.1.

5.1.2.2 Interconnection to User Interface

The two power cables and the four temperature data cables were soldered to a Low-Voltage Differential Signalling (LVDS) connector DF80 (Hirose Electric Co. Ltd, Japan). This connector was attached to a custom-made adapter with an on/off switch. This allows the experiment to be terminated immediately if capsule failure is detected, or if the surrounding tissue temperature exceeds 40°C. The adapter allowed communication between the capsules and the myRIO 1900 portable embedded device hardware (National Instruments, USA), which is controlled via USB with a LabVIEW UI (National Instruments, USA) on a Windows laptop. The myRIO provided a 5 V power supply to the capsule via the tether through the output power pin following connection to the laptop, and the thermistor connections were connected to four analogue inputs of the myRIO. The entire assembling process is illustrated in Figure 5.9.

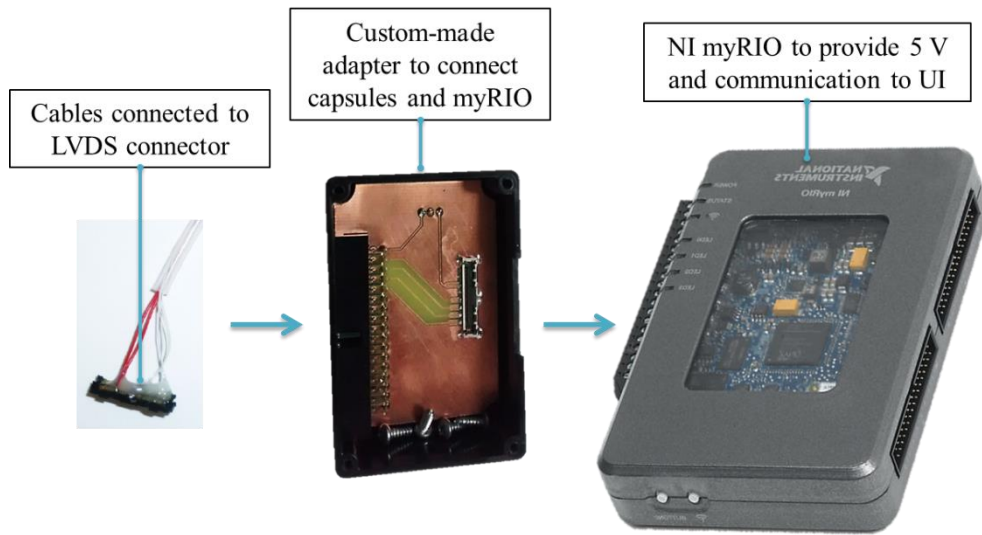


Figure 5.9: Connection of capsule system via an adapter to the NI myRIO

5.1.3 Base station

The base station is a commercially available receiver module, CC1110 (TI, USA), including an antenna, a control unit and an evaluation board (SmartRF Transceiver Evaluation Board (TRxEB, TI, USA), that was connected via USB to a MS Windows laptop. The CC1110 is a low-power SoC (System-on-Chip) with 8051 MCU, Memory and Sub-1 GHz RF Transceiver. The SmartRF Studio firmware (TI, USA) controlled the receiver parameters and monitored and collected information about Packet Error Rate (PER) and Bit Error Rate (BER) data. The receiver (Rx) filter bandwidth was set to 541 kHz and the channel spacing to 200 kHz - all other parameters were selected to match those of the transceiver (Tx). The base station is shown in Figure 5.10. Under ideal conditions, including a specifically designed firmware to suit the purpose of high-speed data reception and a high sensitivity of -95 dBm at 250 Kbaud, the Rx would be able to receive 32.25 Kbytes/s (256 kbps). By using the supplied TI firmware and hardware, the maximum amount of received data was limited to 2.04 Kbytes/s (16.32 Kbps). Developing the necessary firmware would improve the data rate, but this would exceed the scope of this PhD.

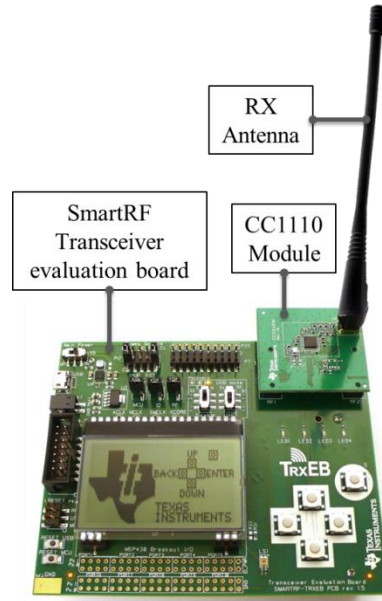


Figure 5.10: Base station module

5.1.4 Programming

Before the capsule systems were fully assembled, the programme code for the RF board was transferred to the CC1310 MCU. A programmer cable PCA100 (Microsemi, USA) was connected to the JTAG interface (FFC connector) on the RF board. To the PCA100 cable, a debugger and emulator module XDS100v3 (Olimex, Bulgaria) was connected, as shown in Figure 5.11 and attached via USB to the Code Composer Studio (CCS) (TI, USA) on the PC.

The MCU was programmed to send data packets composed of a message header, a package counter, a time stamp and the Received Signal Strength Indicator (RSSI), as shown in Table 5.2. The maximum data payload was 255 bytes per packet. Eight packets per second were transmitted, resulting in 16.32 Kbps. For a standard capsule endoscopy image frame of 65 Kbytes (eight-bit image, 256 x 256 pixels), it takes 32 seconds to deliver one frame (0.031 fps).

TABLE 5.2: Programmed data packet set up with message header, package counter, time stamp and RSSI

16:12:53.015	0001	1@SONOPILL1@@SONOPILL1@@...	-23
--------------	------	-----------------------------	-----

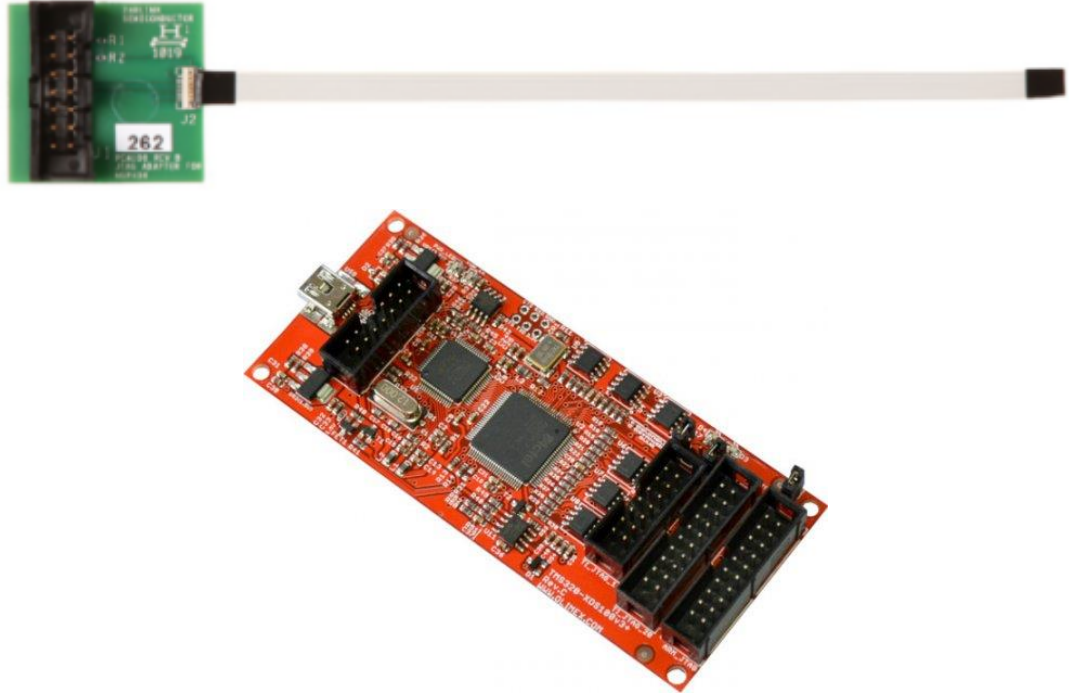


Figure 5.11: Programmer cable (top) and XDS100v3 debugger and emulator (bottom)

Considering the data rate (4 Mbps) of the CC1310 under ideal conditions, a transmission of 500 Kbytes/s and a frame rate of 7.7 fps would be possible. This can be incorporated into future work. Three capsules (RFCap5, RFCap6, RFCap 7 = Group I) were programmed to radiate at a constant power of 0 dBm or 1 mW over an infinite period of time. The other three capsules (RFCap1, RFCap3, RFCap4 = Group II) were programmed to transmit data at multiple power levels of -10, 0, 6 and 10 dBm or 0.1, 1, 4 and 10 mW. The power levels of the transmission signal remained static for five minutes and 20 seconds, allowing for the transmission of 10 frames of a 65 Kbytes image, and increased to the next power level after a five-minute off-period.

The transceiver CC1310 offers a wide range of data rates from 625 bps to 4 Mbps and an automatic Cyclic Redundancy Check (CRC). The modulation format used was the GFSK for the carrier frequency of 433 MHz with a deviation of 127 kHz. Equally, data compression was not taken into account, due to the time constraints and limited scope of this PhD.

The code was initially tested with a CC1310 LaunchPad development kit (TI, USA). The CC1310 version on the board was the 7×7 mm MCU, therefore the code had to be changed accordingly. To eliminate any possible mistakes made during the design and assembly of the PCBs, a simple code to flash the LED onto the back of the RF board was first transferred to the CC1310 LaunchPad, to check whether the code was correct,

and then transferred to the RF boards. With the help of this test, a few alterations on the boards were made until the LED code worked. The final code for transferring the data packets was tested with the LaunchPad, together with a connected 433 MHz antenna, and the previously mentioned base station module attached to the SmartRF User Interface (UI). When the code was running, it was transferred to the RF boards to reveal a few more necessary alterations on the MCU solder connections. Once the boards were fixed, all capsule devices were programmed accordingly.

5.1.4.1 Thermistors

While wireless RF data packets were transmitted, the temperature of the surrounding tissue was continuously monitored via the embedded thermistors, and the temperature data was sent via the attached tether.

Four thermistors were embedded into the capsule shell so that any temperature rise in the surrounding tissue near the antenna could be measured, since traditional SAR measurements near the antenna were not possible during the *in-vivo* trials. The thermistor assembly is shown in Figure 5.12. The thermistors were connected via the myRIO to the computer, where they were continuously monitored during the experiments using a LabVIEW UI. The LabVIEW UI shows the up-to-date temperature value, as well as a graph for each thermistor value. The temperature was updated every second. The LabVIEW UI is shown in Figure 5.13.

For patient safety, the experiment could be immediately aborted if there were evidence of overheating (temperatures in excess of 40°C) or failure of thermistors, which might signify loss of hermetic sealing or a lack of signal.

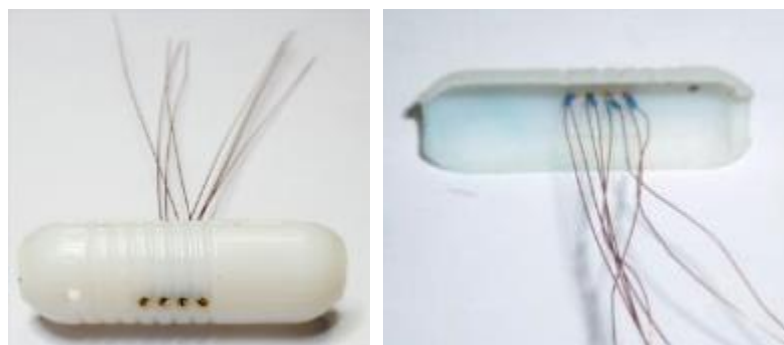


Figure 5.12: Thermistor assembly inside capsule shell

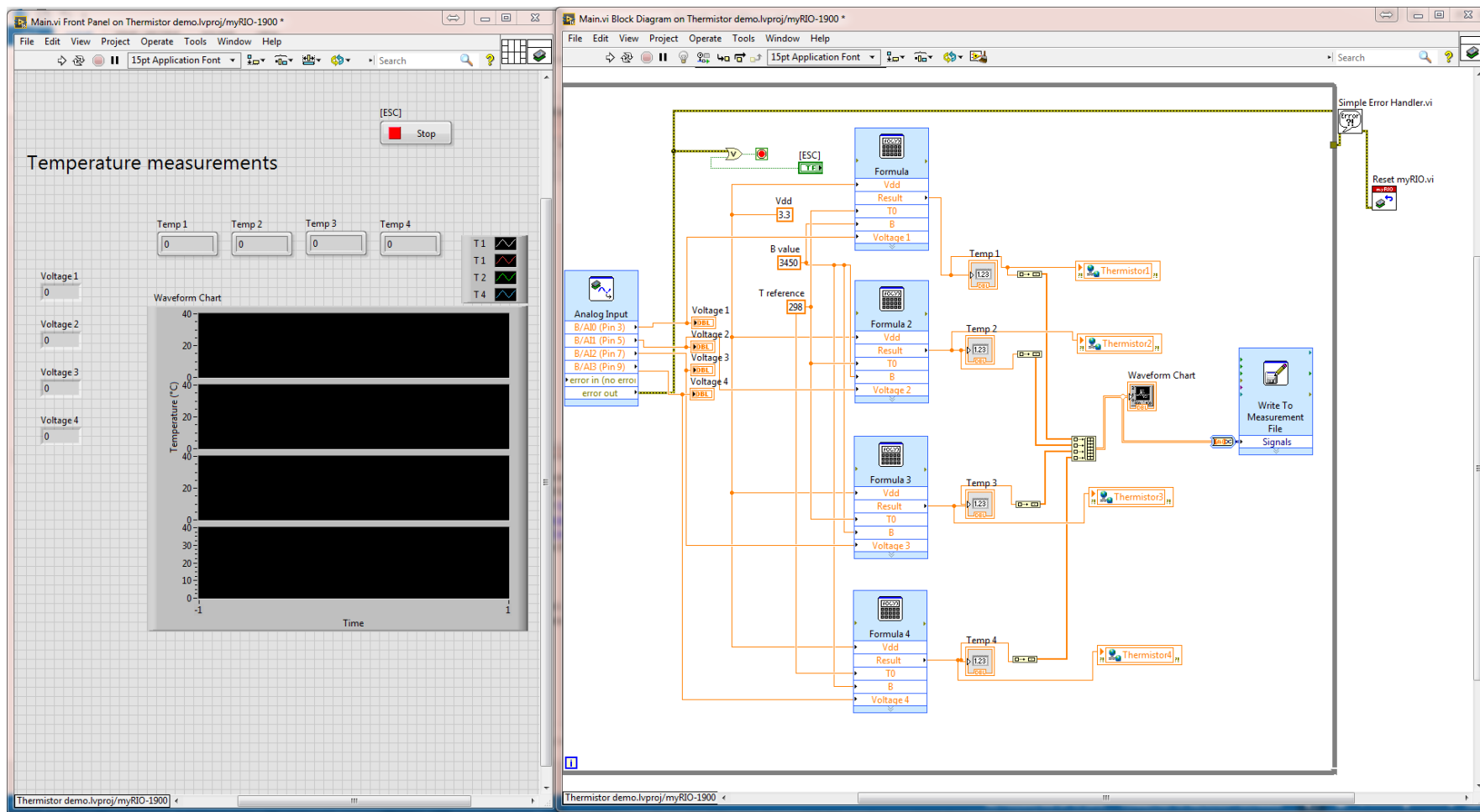


Figure 5.13: LabVIEW UI for monitoring the temperature measured by the on-board thermistors

5.2 INSULATION LAYER

The conformal antenna does not use the internal volume of the capsule but it does require additional coating to protect the antenna from the surrounding tissue and maintain biocompatibility [9, 10].

5.2.1 Biocompatible coating – moulding process

As previously investigated by Merli & Skrivervik, the high dielectric insulation layer, considered part of the emitter antenna system, lowers the attenuation of electromagnetic fields through the layers of the body and can therefore help improve antenna performance within lossy materials [10]. However, the insulation layer used for this device is very thin (≈ 0.3 mm), and its benefit in increasing radiation efficiency is relatively small [44]. In the first prototypes, either a layer of Loctite ($\epsilon_r = 2.42$, loss tangent $\tan \delta = 0.01$) or polyolefin ($\epsilon_r = 2.3$, loss tangent $\tan \delta = 0.01$) was used as an antenna coating to protect it from the surrounding material. To test the final prototype in a porcine model, the device had to conform to ethical regulations. Biocompatible epoxy, EP42HT-2Med USPUSP Class VI biocompatible epoxy (Master Bond Inc., USA), was chosen to hermetically seal the capsule. Before application, the epoxy was tested for any outgassing effects. Outgassing occurs when gas is released from solid materials. For example, volatile products can become trapped during the production of polymer materials. These gases, when released, may be harmful to the patient and the functioning of the medical device. A dummy device was covered with epoxy and after curing was manually crushed using a hammer. The resulting fragments were thoroughly mixed and a 20 mg sample of this material underwent Thermogravimetric Analysis (TGA). The sample was kept at 25°C for 30 minutes before the temperature was increased to 40°C at a rate of $5^\circ\text{C}/\text{min}$. The temperature was held at 40°C for 6 hours, and the mass monitored. The output from the TGA was fed into a Cirrus Mini-Lab gas chromatography-mass spectroscopy (GC-MS) system, where the outgassing was analysed to determine the relative composition of the constituent gases. The majority of detected gasses consisted of water vapour, but with ammonia being the second largest concentration. Ammonia can potentially be harmful, but the measured 34.49 ppm is below the no observable adverse effect limit (NOAEL) of 50 ppm set out by the Agency for Toxic Substances and Disease Registry of the Centre for Disease Control [153].




To guarantee an even distribution of the epoxy over the full length of the capsule, particularly across the antenna, moulds were manufactured to produce a uniform 400 μm thick film. These were created using two additively manufactured forms made of VeroWhite polymer (Stratasys, USA), and filled with a silicone elastomer Sylgard 184 (Dow Corning, USA). Three different polymer releasers were tested (ROCOL Foodlube WD spray, ROCOL mould-release spray, Ambersil Polymer remover), with Ambersil (USA) showing the best outcome for removing the cured silicone pieces.

The cured flexible moulds were sprayed with the polymer remover (Ambersil), and the assembled capsules were placed into one part of the cured mould. The second part was manually aligned with the other half and secured with a clamp. To ensure its even coverage with minimal air bubbles, the epoxy was degassed before use by placing the filled syringe into a bell jar and operating a vacuum pump in 30-second on/off cycles until the gas bubbles disappeared. The epoxy was then injected into the mould with a syringe until the cavity was completely filled and cured for three hours at 55°C. Afterwards, the mould was removed from the capsule. The epoxy film thickness was measured using a digital caliper to be between 400 and 500 μm . The final step involved depositing an 8 μm thick conformal layer of Parylene-C (USP class VI polymer) onto the external surface of the Verowhite capsules, using a SCS PDS 2010 vacuum deposition tool. Parylene-C is a commonly used biocompatible and biostable material known for its dry lubricant properties. The reduction of friction between the capsule and the surrounding tissue should ensure ease of insertion and movement along the GI tract. The deposition process was conducted at the Institute for Integrated Micro and Nano Systems (IMNS) at Edinburgh University.

Humidity tests have previously been performed on a dummy capsule consisting of an empty, standardised capsule coated with an 8 μm layer of Parylene-C for use in any destructive tests. For the humidity ingress tests, the capsule incorporated a small PCB containing a humidity sensor. The capsule was submersed into a beaker with water (37°C) and the change in humidity was monitored for 72 hours by Labview RealTime module. An increase in humidity was detected, which suggested adding the biocompatible epoxy to the full device to ensure hermeticity.

A step-by-step description of the moulding and epoxy coating process is given in Table 5.3.

TABLE 5.3: Step-by-step of moulding and coating process

1. Design of 3D print moulds in AutoDesk inventor	
2. Manufacturing of moulds with 3D printer	
3. Preparing the silicone moulds a) Mixing silicone elastomer Sylgard 184 (10:1 weight ratio) b) Degassing in plastic tub → 30s on/off for a few cycles	
4. Before pouring mixture, the 3D printed mould was sprayed with a mould releaser – 3 were tested	<ul style="list-style-type: none"> - Rocol Foodlube WD spray - Rocol Mould release spray - Ambersil Polymer remover → best outcome for removing the moulds
5. Fabricating 2 pairs of silicone moulds a) Pouring mixture into 3D printed moulds b) Repeating degassing method c) Moulds on hot plate (55°C for 6 hours)	
6. Preparing the epoxy coating a) Mixing 2 components epoxy (1:2.5 weight ratio) b) Degassing in plastic tub → 30s on/off for a few cycles c) Filling epoxy mix into syringe, avoiding bubble generation d) Degassing in syringe → 30s on, 30s off for a few cycles	
7. Preparing capsules and moulds a) Spraying of cured silicone moulds with polymer remover b) Placing assembled capsules inside one part of mould c) Manually aligning the other half and securing with a clamp	
8. Coating procedure a) Injecting epoxy into mould b) Leaving mould on hot plate (55°C for 3 hours)	Layer thickness of 0.3µm

5.3 SUMMARY

In this chapter the successful assembly process of a complete ingestible capsule prototype was presented. The 3D printed housing offered enough space to integrate the two necessary PCBs with attached thermistors, as well as embedded tracks to support the antenna structure. It features an opening, so the tether bundle could be attached. The tether bundle served as power supply, temperature data transmitter and retrieval tool for the *in-vivo* experiments. The tethers were embedded into a biocompatible Teflon tubing to stabilise the connections and isolate them from any tissue contact.

Selection of system components depended on the individual size of the components, availability, costs and, concerning the transceiver chip, integrability in terms of the required specifications. The electronic circuit was designed and the PCBs were manufactured, assembled and programmed. The MCU was programmed to send data packets to a receiver with two different transmission modes. Three prototypes transmitted at a constant power of 0 dBm or 1 mW over an infinite period of time. The other three capsules were programmed to transmit data at multiple power levels of -10, 0, 6 and 10 dBm or 0.1, 1, 4 and 10 mW. The completed devices could individually be connected to the NI hardware and the LabVIEW UI on the laptop, sending the data packets to the TI receiver module. The maximum amount of received data was limited to 2.04 Kbytes/s (16.32 kbps).

After the completion of the prototype assembly a detailed description of the biocompatible coating process was given. The epoxy was previously tested for outgassing effects, resulting in maximum values below the set cutoff limits.

The moulding process provided an effective way of evenly covering the surface of the shells, fixing the tether bundle to the device, sealing the complete prototype and insulating it from the surrounding tissue. The epoxy coating was followed by a parylene coating process to fully conform to health and safety regulations to protect the antenna from the surrounding tissue and maintain biocompatibility of the ingestible device.

In the following chapter the device prototypes are tested for their functioning in *in-vitro* experiments.

CHAPTER 6 *IN-VITRO* EVALUATION

Following the successful design and manufacture of the capsule devices, *in-vitro* tests were performed to check the functionality of the complete device, and to validate radiation characteristics before *in-vivo* experiments were undertaken using animal models. The measurements were performed in an anechoic chamber, using the same equipment that would be employed in the *in-vivo* trials to follow. All six prototypes were tested, and the experiments provided an opportunity to practice the various procedures for the trials ahead.

This part of the thesis evaluates the telemetry prototypes with dielectric muscle tissue properties within the phantom material. This chapter is organised as follows: the configuration of the phantom test set-up is explained in Section 6.1. Firstly, the phantom material was prepared, followed by the receiver arrangement. The capsule devices were connected and inserted into the phantom. Section 6.2 describes the investigation of the performance of the capsule. Data transmission over a longer period of time, transmission performance over an increasing distance between Rx and Tx and radiation distribution were all measured and tested. Section 6.3 discusses the results. The link budget analysis mentioned in Section 3.1.7 is executed in Section 6.4 to find out the estimated signal attenuation and losses. Finally, Section 6.5 finishes by summarising the recorded results.

6.1 PHANTOM CHARACTERISATION

The simplified, cubic single-layer body model used in the simulations did not fully represent the properties of a multi-layered human body structure. The model provided nevertheless a simple but effective evaluation method for antenna performance and optimisation during the simulation analysis. For the phantom experiments, a spherical phantom of a similar size to the simulation set-up with the same material properties was used. The spherical form was chosen as it was easier to shape when preparing the phantom. The shape also ensured an even amount of phantom material mass surrounded the radiator, to perform the radiation pattern measurements, as well as testing the data transmission performance of all manufactured devices before the *in-vivo* tests. The shape and size of the phantom should not affect the radiation characteristics in terms of resonance frequency and SAR value.

6.1.1 *In-vitro* test set-up

As mentioned in Section 4.1.3, the body phantom used in these tests consisted of a mix of hydrophilic organic powder and degassed water, forming a doughy material that reproduced approximately the electromagnetic properties of the material used in the simulations. To investigate the performance of the antenna system, two 28 cm diameter semi-spherical moulds were used, each filled with the prepared phantom material. The moulds were placed in two manufactured square boxes (side length 31 cm). The two boxes facilitated a ‘stamp sheet’ which imprints the capsule position in the middle of the phantom every time it is tested to ensure that the experiments can be repeated. The stamp was placed onto one semi-spherical phantom piece and, after its removal, one capsule was placed within the indented, recessed outline within the tissue phantom. This fixed the position of the capsule within the tissue phantom for each experiment. The second phantom part was placed on top so that the capsules were evenly surrounded by the dielectric material. Figure 6.1 visualises the individual stages of this process.

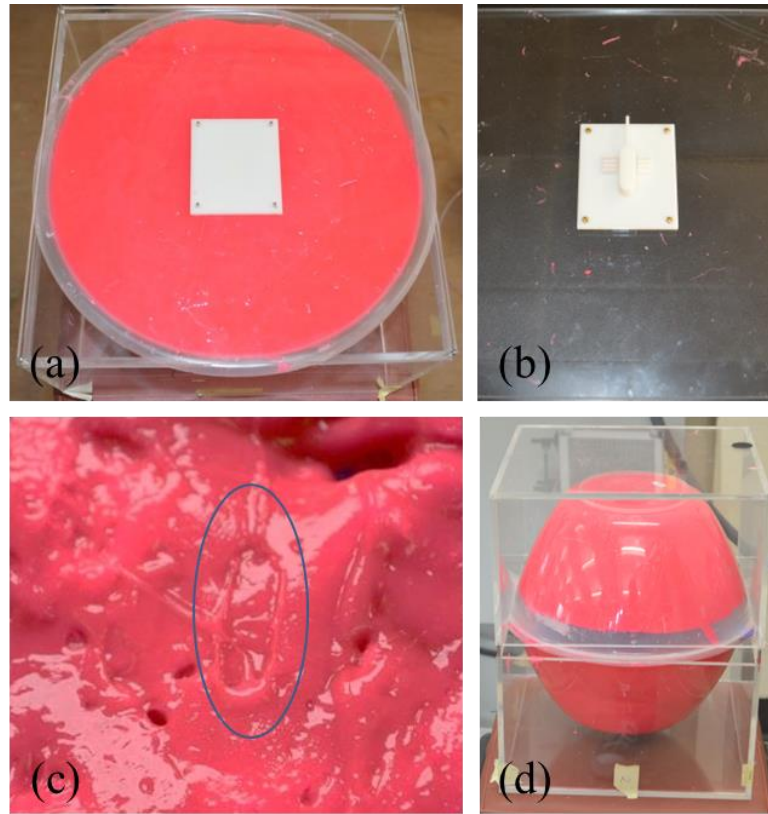


Figure 6.1: a) One semi-spherical mould with stamp placed on top; b) Stamp sheet; c) Imprinted phantom part; d) Finished phantom set-up

Once placed inside the phantom, the capsule tether was connected to the custom-made adapter, which communicated with the NI myRIO and the MS Windows laptop

positioned on a mobile trolley. Figure 6.2 shows the trolley set-up, which will also be used for the subsequent *in-vivo* experiments. The CC1110 receiver module (TI, USA) was connected via USB to the laptop, while the SmartRF Studio firmware (TI, USA) was used to control the Rx parameters, and to monitor and collect information about Packet Error Rate (PER) and Bit Error Rate (BER) data. The Received Signal Strength (RSSI) over distance, as well as the radiation pattern in horizontal and vertical orientations of each capsule antenna, was recorded to analyse the extent to which the distance between Tx, Rx and the orientation influenced the signal strength.

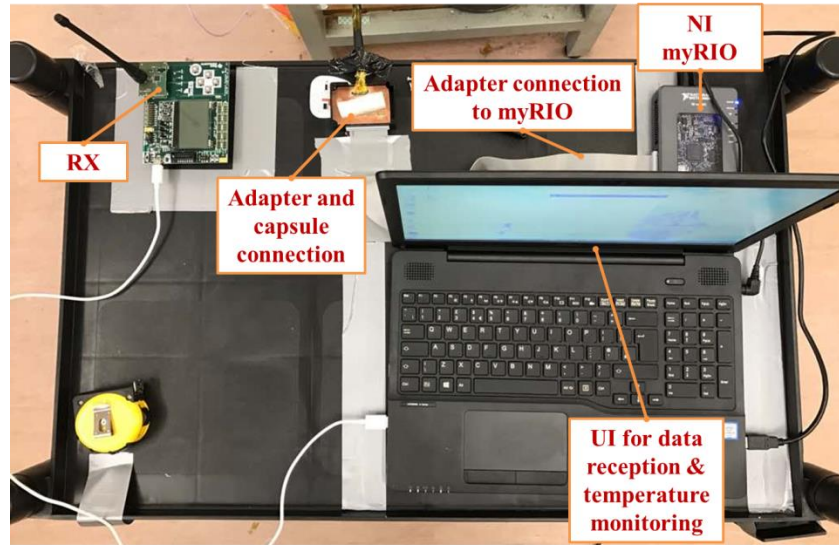


Figure 6.2: Experimental trolley set-up of the Tx/Rx system: The Rx is connected via an USB cable to the laptop and controlled through the SmartRF studio software from Labview, which records the received data packets. The capsule prototypes are connected to the adapter, which is connected to the NI myRIO. The NI myRIO supplies the power to the capsules and is controlled by the developed Labview UI, which is also monitoring the temperature data [154]

6.2 MEASUREMENTS

This section describes the measurement performance of the proposed data telemetry system. The six fabricated capsules were divided into two groups of three, according to their transmission settings. One capsule (Cap2) served as dummy capsule, to be able to test different programs and soldering processes, as well as pre-test the coating process. The capsules programmed with the constant output level of 0 dBm or 1 mW made up Group I (Cap5, Cap6, Cap7), while the other three capsules programmed to transmit at multiple power levels starting at -10 dBm or 0.1 mW were in Group II (Cap1, Cap3, Cap4). The capsule settings are summarised in Table 6.1. The experiments took place in an anechoic chamber. Figure 6.3 shows the experimental set-up of the trolley and the phantom system.

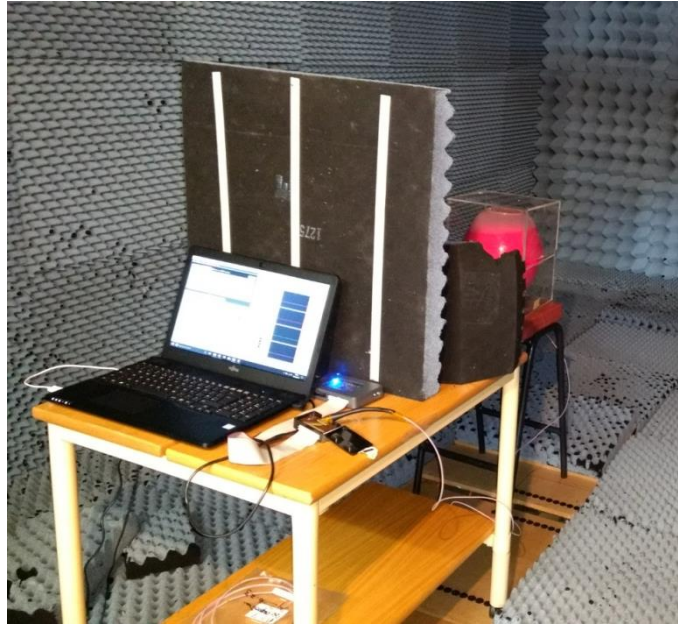


Figure 6.3: Trolley set-up in anechoic chamber: The phantom with embedded prototypes and the Rx base station is placed on a chair behind the absorber. The laptop is placed on a trolley on the other side

The laptop, TI myRIO and adapter were placed on the trolley and the Rx module and phantom were placed behind an absorber part within the anechoic chamber, to reduce reflections of the EM waves. This setup also reduces the interference of EM waves with other electronic devices.

TABLE 6.1: Capsule settings

	Capsule name	Data transmission program
Group I	Cap5, Cap6, Cap7	Constant power level: 0 dBm (1 mW)
Group II	Cap1, Cap3, Cap4	Multiple power levels: -10, 0, 6, 10 dBm (0.1, 1, 4 and 10 mW)

6.2.1 Data transmission set up

All capsules were tested to check whether they functioned correctly. Group I capsules were inserted horizontally and each was transmitting data for 5 minutes. The Rx was placed 60 cm from the center of the phantom where the capsule was located. Signal strength, PER and BER were recorded, and the RSSI graph is shown in Figure 6.4 for all three capsules.

The other capsules in Group II (inserted horizontally) were tested for the full length of their programmed transmission cycle (37 minutes) to ensure each power increase was working correctly. The Rx was again placed 60 cm away from the center of the phantom. Figure 6.5 shows the RSSI results of the three capsules.

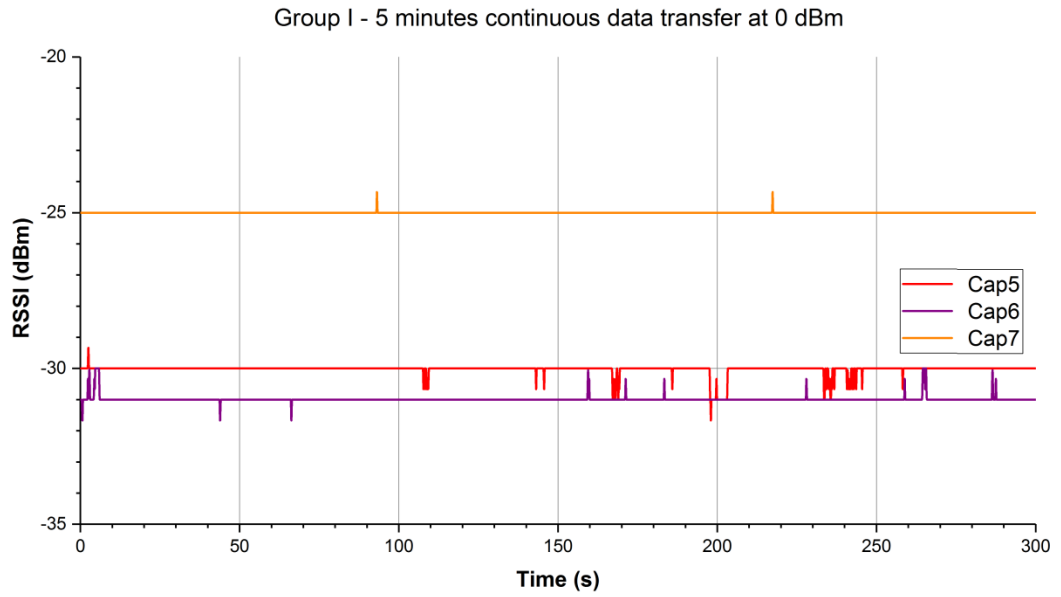


Figure 6.4: Group I data transmission shows a steady signal strength

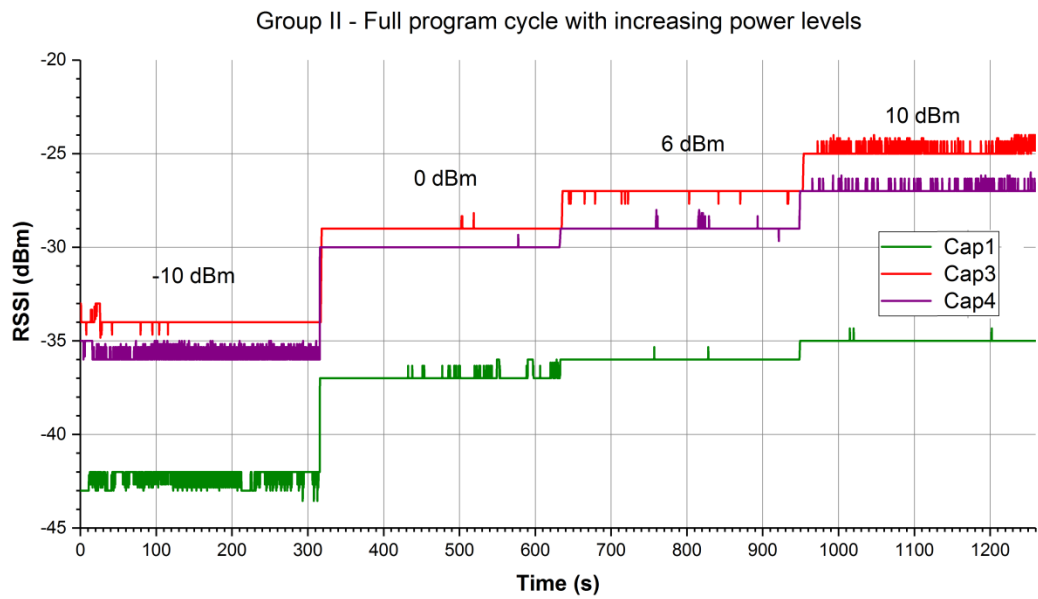


Figure 6.5: Signal strength of Group II with gradually increasing power output

6.2.2 Distance measurements

For distance measurements, the phantom box was placed on a stool and the trolley was placed next to a measurement tape. The capsules were horizontally (x- and y-plane) inserted into the phantom pointing towards the Rx, and the separation of the Rx and Tx was increased in 10 cm stages from 20 to 60 cm. The data was recorded for 20 seconds

at each stage. Figure 6.6 shows the gradually decreasing strength of the signal from the capsules.

The minimum distance of 20 cm was chosen since this is the estimated distance between a receiver attached to the body and the ingested capsule travelling inside it. The maximum distance of 60 cm was the approximate distance between the CC1110 Rx and the capsule during the following *in-vivo* trials.

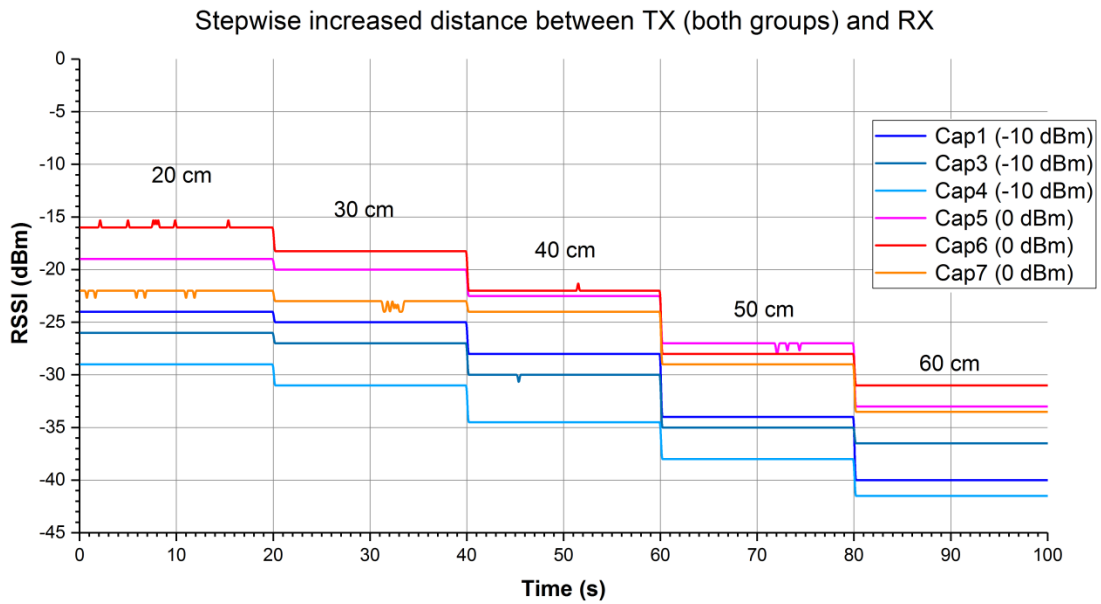


Figure 6.6: Decreasing RSSI over increasing separation distance, with Group I capsules having a transmit power of 0 dBm and Group II capsules -10 dBm

6.2.3 Radiation pattern

To observe the effect of capsule orientation on signal strength, the capsules were inserted horizontally (x- and y-plane) into the phantom. The phantom setup over was turned, so that the capsules were vertically orientated along the z-axis, pointing downwards, with the tether connection pointing upwards. The Rx was moved in 45° stages around the Tx at a distance of 60 cm. At each stage, the RSSI was measured for 10 seconds, and eight data points in each plane were taken to gain an insight into the signal distribution around the capsules. Figure 6.7 shows the radiation distribution of the capsule antenna.

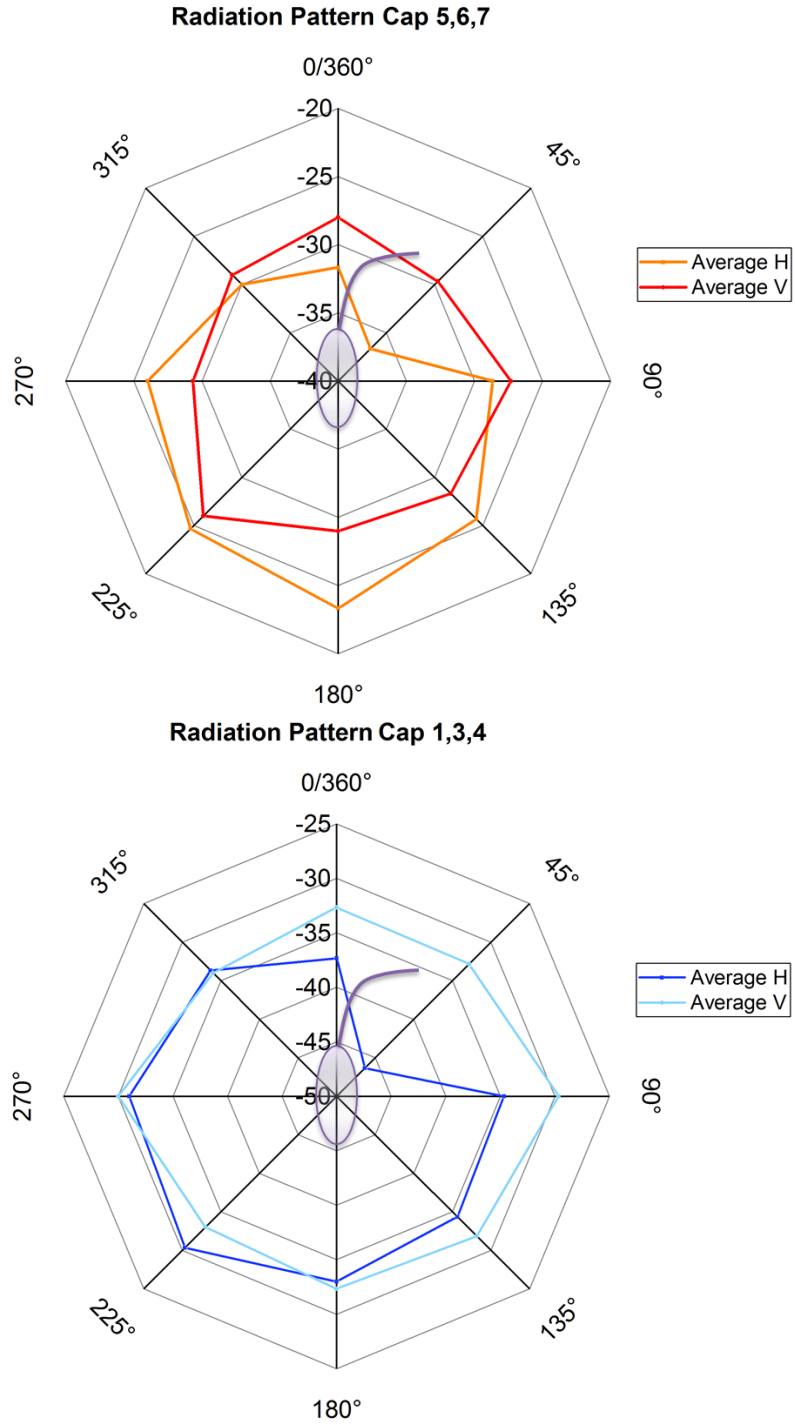


Figure 6.7: Radiation pattern for Group I capsules (top) and Group II capsules (bottom). An average of the measured RSSI of each capsule group was taken in horizontal (H) and vertical (V) plane

6.3 RESULTS AND DISCUSSION

6.3.1 Data transmission

Each capsule in Group I transmitted without interruption for 5 minutes. All packets transmitted and received were free from errors and resulted in a PER of less than 10^{-3}

and a BER of less than 10^{-5} , sufficient for a low-error data transfer with this length and number of data packets [57, 59, 155]. The PER and BER tests examine channel conditions during data transmission, as well as data collection efficiency. Kim *et al.* [156] state that the PER quantifies data transmission efficiency, and packet errors can be caused either by complete packet loss and/or bit errors. Every false or missing packet increases the PER. One failure in 1,000 transmitted packets is therefore considered a satisfactory outcome. The BER defines the number of faulty bits occurring during data transmission. A BER of less than or equal to the 10^{-5} threshold demonstrates a tolerable performance for maintaining a good image quality.

The signal strength remained steady and ranged between -25 dBm for capsule 7, -30 dBm for capsule 5 and -31 dBm for capsule 6.

The same experimental set-up was used with the Group II capsules transmitting at a gradually increasing power level. Uninterrupted data was transmitted for a duration of 37 minutes for each capsule, once only. The PER of these capsules varied from 0 to 10^{-3} , while the BER was recorded as less than 10^{-5} for all power levels. Higher transmission power levels lead to a lower BER and therefore higher image quality [157]. The RSSI increased by 5 dBm from -10 to 0 dBm, 2 dBm from 0 to 6 dBm and 2 to 3 dBm from 6 to 10 dBm.

The variation in signal strength is thought to be caused by manufacturing tolerances and detuning effects of the internal electrical components. In the measurements, only complete packet losses occurred. Each packet was successfully created and transmitted to the Rx.

6.3.2 Distance

During the distance measurements, a decrease in RSSI was observed when measuring the signal attenuation over distance for every 10 cm separation from the phantom, as shown in Figure 6.6. Table 6.1 summarises the individual decrease in signal strength.

TABLE 6.2: Decrease in RSSI per 10 cm separation step

		RSSI decrease in dBm			
	Step	20-30 cm	30-40 cm	40-50 cm	50-60 cm
Group II	Cap 1	1	3	6	6
	Cap 3	1	3	5	1.5
	Cap 4	2	3.5	3.5	3.5
Group I	Cap 5	1	5.5	4.5	6
	Cap 6	2.25	3.75	6	3
	Cap 7	1	1	5	4.5

The further away the Rx is moved, the larger the decrease in RSSI. The received signal decreases from 20 to 60 cm by an average of 14.5 dBm for Group I and -13 dBm for Group II. At a distance of 60 cm, the comparable distance to the set-up of the *in-vivo* trials, the average power of the Group I capsules in the phantom between Rx and Tx was -32.5 dBm - for Group II it was -39.3 dBm. The RSSI is generally lower for Group II capsules due to the first programmed power level of -10 dBm.

The variation in signal was more significant for the Group II capsules running at a lower power, and also steeper than the attenuation of Group I. In terms of the change of signal strength over distance between the Rx and Tx, an attenuation of the signal with increasing distance was measured as expected.

6.3.3 Radiation pattern

Figure 6.7 shows the radiation distribution of the capsule antenna. A lower RSSI in the horizontal plane can be observed at 0° to 45° at the location of the tether and where the antenna is internally attached to the PCBs. The vertical plane shows a more circular radiation distribution.

Due to the large angular steps of the experimental set-up, no possible side lobes could be detected. Compared with the almost omnidirectional pattern of the simulations, the radiation pattern examined within the phantom showed a large drop in power at the tether and internal antenna connection. This effect was the combination of two factors: 1) the electric fields originating from the current running through the tether, which interfered with the fields of the capsule antenna and 2) the 2 mm extension of the antenna to connect to the internal PCB, which alters the antenna geometry slightly. The simulation, on the other hand, used an ideal discrete port as a feeding point, connected

to the GND plane, since it was not possible to simulate the full system with the tether included. Therefore the simulated radiation pattern originated from ideal conditions and the influence of the tether was not examined.

The expected slight drop in RSSI towards both ends of the capsules, as seen in the simulated radiation pattern (Figure 4.14), was not observed. This can be due to measurement setup and the relative position of the Rx to the Tx. It is possible that the Rx was slightly higher or lower positioned and therefore missed the drop in RSSI.

This result indicates that the orientation of the capsule within the small bowel can affect the measured signal strength, which can be seen in the drop of RSSI of up to -18 dBm within the phantom. Future applications will be completely wireless and unaffected by a tether; hence the measured radiation pattern is more likely to represent the almost omnidirectional radiation of the simulated device.

6.3.4 SAR/Temperature measurements

Throughout the *in-vitro* experiments the LabVIEW programme responsible for the monitoring of the temperature by the thermistors was run to ensure its correct operation over the full length of the experiments. No increase in temperature was noted during any of the phantom experiments.

To test the correct temperature response of the thermistors, a thermometer was inserted into the phantom to take a reference temperature. Each individual thermistor was observed on every capsule. The thermistors on Group II capsules all functioned correctly. However, one thermistor on two Group I capsules failed, with one capsule remaining fully functioning. It is noted that three working thermistors on the capsules still fulfill the trials' safety requirements. It is probable that a thermistor did not work because of the interconnection on the internal RF PCB, which was problematic during the assembly process. It is assumed that, while both capsule parts were being combined, internal connections became disconnected. Figure 6.8 illustrates a screenshot of the thermistor measurements UI and the data transfer UI.

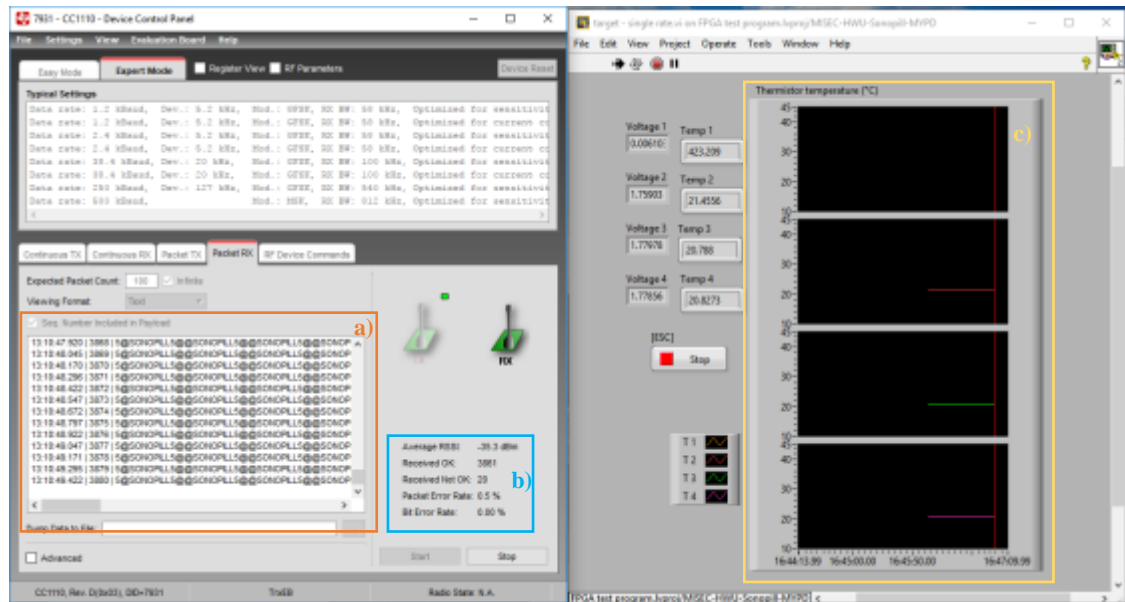


Figure 6.8: Screenshot of the data (left) and temperature measurement UI (right): a) The text box shows the received data packets, b) BER and PER data, c) visualisation of the temperature monitor

The left hand side of the screen shows the information about data packages received by the Rx, PER and BER. The right hand side presents the LabVIEW UI showing the temperature measured by the thermistors in real time. In cases when any overheating occurred the experiment could be aborted immediately.

6.4 SUMMARY

The most important conclusions of the Chapter can be summarised as follows. Both capsule groups show their successful operation and demonstrate a PER and BER below 10^{-3} and 10^{-5} , respectively, and stay within the safety regulations as no temperature increase was detected.

Orientation and distance of the capsules to the Rx and the transmission power level affect the signal received by the Rx and need to be accounted for in future experiments. Especially the tether connection distorts the signal and also forces the capsule into positions, which would not occur with tether-less devices.

The calculated FSPL for the transmission from within the phantom with muscle properties adds up to 32.74 dB and the PL is expected to be around -70 dBm. This PL value is likely going to change when transmission from within human or animal bodies is considered. It can be higher or lower depending on the types of surrounding tissue.

The validation of the system is performed in *in-vivo* experiments, which are described in the next chapter.

CHAPTER 7 *IN-VIVO* CHARACTERISATION

After the successful completion of the *in-vitro* tests of the capsule, the performance of the capsule antenna was examined using *in-vivo* porcine models to validate the functionality of the telemetry system under real tissue conditions. Data transfer was tested to analyse the performance of the telemetry system with different data transmission modes and to assess the influence of the porcine body tissue on the received signal. Thermistor measurements of the transmission devices offer a check-up of temperature restrictions that need to comply with safety regulations.

All the components used in the *in-vitro* tests were transferred to the location of the porcine trials (Roslin Institute, Roslin, UK). These tests were conducted here in collaboration with the Wellcome Trust Critical Care Laboratory for Large Animals under licence from the Home Office (PPL 70/8812). The age of the three pigs ranged from three to five months, while their weights varied between 56 kg and 64 kg. The experiments were performed over two consecutive days. One euthanised pig (PM1) (lying on its right side) was used on the first day. Two live pigs (PigsX and Y) and the later euthanised PigY (=PM2) (all lying on their backs) were used on the second day.

The chapter of the thesis describes the procedure of the two-day porcine trials. The chapter is organised as follows: Section 7.1 presents the set-up of the experiment and outlines how the pigs and equipment were prepared, together with the individual configuration of the two different groups of capsules. Sections 7.1.1 and 7.1.2 describe the procedure for each complete transmission mode measurement, followed by a discussion of the results in 7.2. The data transmission results of the live pigs are compared with those for the dead ones and the phantom test results. A brief discussion of the temperature measurements is presented in 7.2.2.3.

7.1 PIG PREPARATION AND TRIAL PROCEDURE

The set-up for the experiments is represented in Figure 7.1, and a summary of the characteristics of the pigs and the experimental conditions under which they are subjected are given in Table 7.1, in which the abbreviation PM stands for post-mortem.

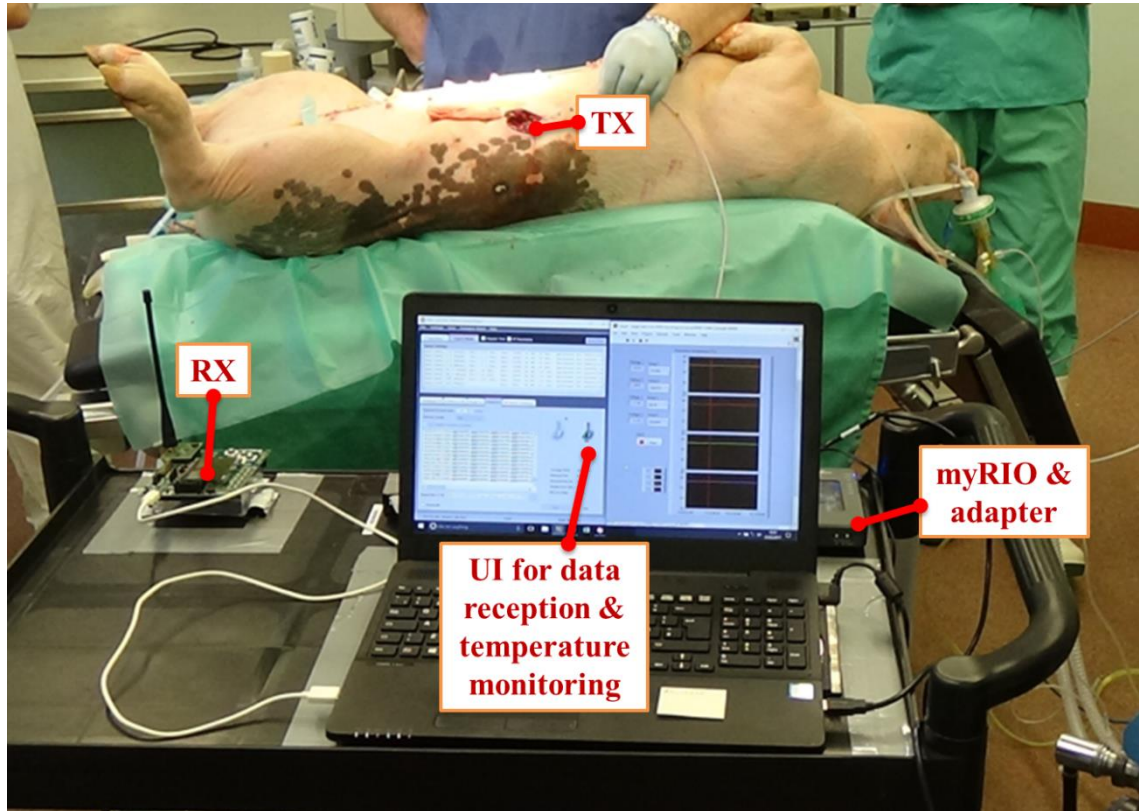


Figure 7.1: Porcine trial set-up - capsule (Tx) inserted via the created stoma; Rx, laptop for data recording and TI adapter placed on trolley next to pig

TABLE 7.1: Pig experimental set-up

	PM1	PigX	PigY = PM2
Age (months)	3	4	5
Weight (kg)	56	60	64
Distance between stoma and Rx (cm)	55	62	70

Shortly after the stoma had been created, the pigs were prepared for the experiments inside the operating theatres and the equipment was set up. An ultrasound system (Siemens Sonoline Antares) was available to examine the position of the capsules within the small bowel. All life functions were constantly monitored using a compact monitor module (Ohmeda Compact, Datex, USA), and anaesthesia was maintained

using an anaesthesia system (Ohmeda Excel 210 SE Anaesthesia Machine, Datex, USA) including a respiratory system with a respiratory rate of 20 breaths/min for PigX and 24 breaths/min for PigY. Anaesthesia was induced with isoflurane (Isoflo Zoetis, Surrey, UK), vaporised in oxygen and nitrous oxide administered via a Bain breathing system and face mask. A cannula was placed in the auricular vein and the trachea was intubated. Anaesthesia was maintained using isoflurane. Ringer's lactate solution (Aquapharm No 11; Animalcare, North Yorkshire, UK) was administered at $10 \text{ ml.kg}^{-1}.\text{h}^{-1}$ throughout the study. The pigs' lungs were mechanically ventilated to maintain normocapnia. An experienced veterinary anaesthetist monitored vital signs during the experiment. Once the experiments were complete, the animals were euthanised without recovery from anaesthesia using pentobarbital.

The experimental system was fixed to a trolley, to facilitate portability between venues. The RF equipment trolley was placed as close as possible to the pigs to minimise the transmission distance, which varied between 55 cm (PM1), 62 cm (PigX) and 70 cm (PigY, PM2). Four capsules were tested *in-vivo* over the two days.

The antennas of Group I transmitted with a constant output power level of 0 dBm (1 mW) while being manually moved along the small bowel during the porcine tests. The antennas of Group II transmitted at different output power levels, while the capsule remained motionless within the small bowel. The transmitted power levels were 0.1, 1, 4 and 10 mW (-10, 0, 6 and 10 dBm). The power levels remained constant for 5 minutes and 20 seconds. This time frame corresponds to the length of submission of two frames of 326 kBytes. After this time, the antennas switched off for five minutes before the power was raised to the next level.

7.1.1 Static power – Group I

The influence of the capsule movement and the surrounding tissue mass/type on the RSSI, PER and BER was investigated, while the four on-board thermistors monitored any potential temperature increase.

Before the first capsule was inserted, distance markers were placed on the pigs' skin at 2, 4, 6 and 8 cm from the stoma to allow for a more repeatable withdrawal rate, as shown in Figures 7.2 and 7.3.



Figure 7.2: Pig set-up at the start of the experiments – The capsules are inserted and the distance markers next to the stoma and tape marker on the tubing to allow for a more repeatable withdrawal rate

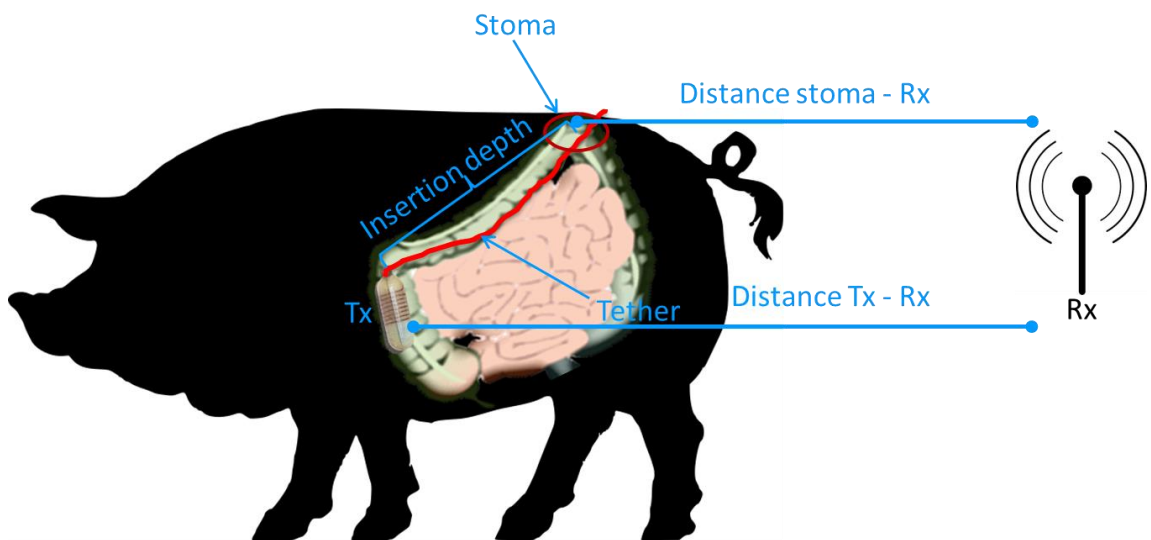


Figure 7.3: Visualisation of the different distances involved in the measurements: The insertion depth shows how far the capsule is inserted; the distance from Rx to stoma is steady (PM1 = 55 cm, PigX = 62 cm, PigY/PM2 = 70 cm); the distance between Tx and Rx is determined by the location of the capsule inside the pigs' body

The tubing was marked with KaptonTM tape at the 60 cm mark to log the insertion depth and return to approximately the same location, at which point the measurement was repeated. The capsule was inserted through the stoma 60 cm deep into the small bowel to keep it enclosed by as much body mass as possible, providing a worst-case scenario where many different tissue layers surround the antenna system. A 0.9% by volume saline drip at the stoma entrance provided lubrication to make it easier to insert the capsules, and a thermometer was inserted 60 cm past this point to record the internal temperature of the small bowel before and after each experiment.

The location of the insertion of the capsule was initially scanned with transcutaneous ultrasound to identify the tissue types present at the capsule location. The ultrasound image can be seen in Figure 7.4. It was difficult to obtain clear ultrasound images due to the type of ultrasound probe and the skills of the operator; therefore only one image was taken to identify the tissue surrounding it. Figure 7.5 shows an endoscopy image of one of the capsules, obtained within the small bowel of PM2.

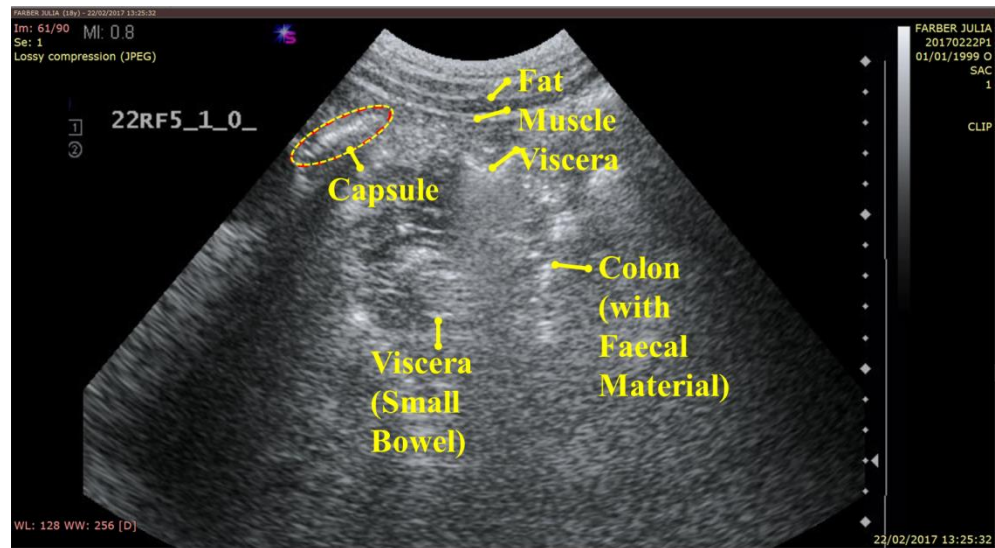


Figure 7.4: Ultrasound image of capsule inserted in the small bowel and its surrounding body tissue layers

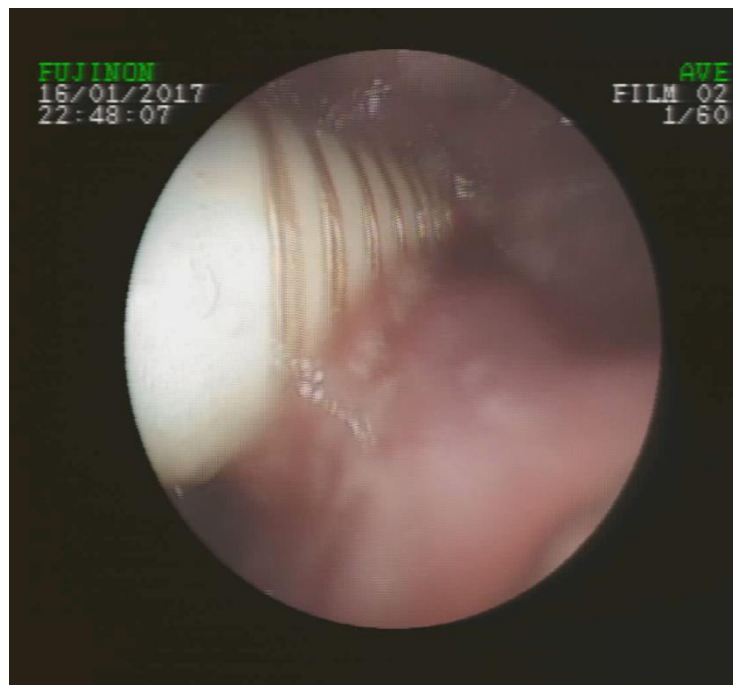


Figure 7.5: Endoscopy image of capsule within the small bowel of PM2

The capsule was then slowly withdrawn along the distance markers with a velocity of 2.7 mm/s. After reaching the 8 cm mark, the capsule was stationary for 20 seconds. Subsequently, the process was repeated twice. Time stamps were recorded to relate the

capsule location to the RF signal strength recordings. The experiment was performed twice with two capsules each time, and the temperature and RF data were continuously logged in Microsoft Excel files. The receiver UI detected any Cyclic Redundancy Check (CRC) errors and calculated the PER automatically. Transmission began as soon as the capsules were powered up by the laptop software and, as previously stated, could be aborted at any time via a 'kill' switch on the trolley. The overall time period for this part of the experiment was approximately 45 minutes per pig and 16 data sets were recorded. This experiment is able to gather data about PER, BER and the change of signal power efficiency under normal operating conditions in the small bowel.

7.1.2 Variable power – Group II

The next experiment was conducted with the capsules operating at variable output power levels (0.1, 1, 4 and 10 mW or -10, 0, 6 and 10 dBm) while fixed in one location. One reason to perform this type of experiment was to gather data about thermal transfer under abnormal operating conditions where the pill is retained to test the possible temperature increase of tissue surrounding the antenna [160]. Another was to find the lowest transmission power that still allows for a wireless connection at a low error rate. Temperature, PER, BER and RSSI were recorded.

The same set-up was used as in the previous experiments. The capsule was inserted through the stoma up to 60 cm deep, and the tubing was fixed in place with tape. The power levels were increased in stages, with an off-period of five minutes between each increase. The pause served as recovery for the porcine tissue in case any temperature increase had occurred during signal transmission.

7.2 RESULTS AND DISCUSSION

7.2.1 Static power – Group I

The first part of the experiments involved two RF capsules transmitting data at a single, constant power level while being gradually withdrawn from the small bowel. This experiment was used to gather data about PER, BER and the change of RSSI data under normal operating conditions in the small bowel. Additionally, the temperature measurements were observed and data was collected. Figures 7.6 to 7.8 show the resulting graphs of the measurements of two Group I capsules inserted into both living and post- mortem pigs. All graphs indicate the change of RSSI over insertion depth

from 60 cm to 36 cm within the small bowel. The higher the detected RSSI value, the less likely it is that data will get lost.

The capsule performance varied in terms of signal strength, but overall there was a consistent output, with a PER and BER of less than 10^{-5} in both types of pigs. This is a similar outcome to the phantom tests. In the following sections, the results of all living and euthanised pig trials are compared and discussed.

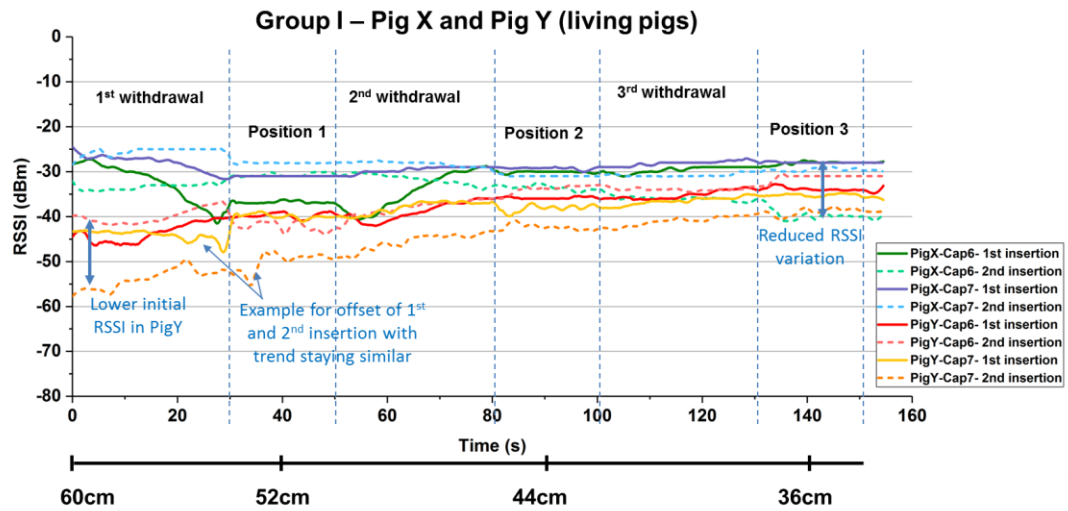


Figure 7.6: RSSI of two Group I capsules (two insertions each) in both living pigs (PigX and PigY)

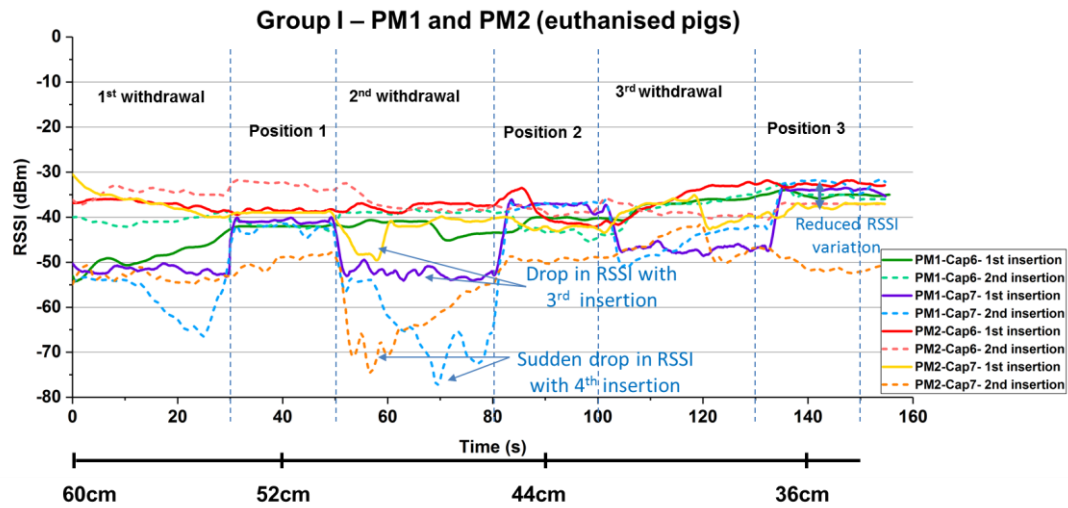


Figure 7.7: RSSI of two Group I capsules (two insertions each) in both euthanised pigs (PM1 and PM2)

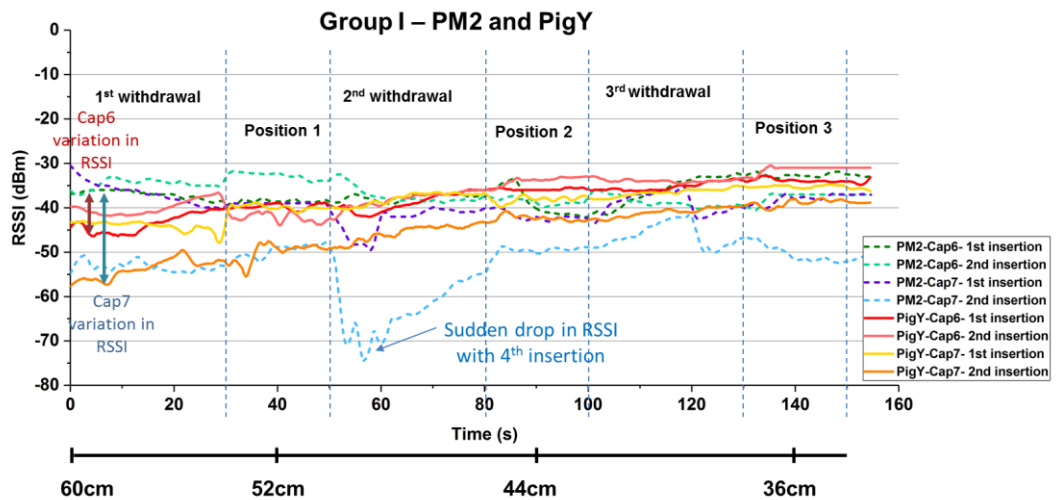


Figure 7.8: Comparison of RSSI of two Group I capsules (two insertions each) in PM2 and PigY

7.2.1.1 *Living pigs*

The results observed in Figure 7.6 of the Group I devices (Capsules 6 and 7) show that the variation in RSSI is at its highest when the capsule is inserted to the furthest point from the stoma at the start of the withdrawal process. The RSSI showed a variation from -24 dBm to -57.5 dBm in the living pigs; the variation for PigX ranges from -24 to -32 dBm and from 40 to -57.5 dBm for PigY. This effect is probably due to the increased insertion depth or increased tissue thickness and the resulting variation in permittivity of the various tissues compared with the area nearer the stoma. Different dielectric properties of the capsule-surrounding material lead to a shift in frequencies and a change in power absorption, causing a change in signal strength throughout the withdrawal process.

The measured signals from PigY had a much lower initial RSSI value than the ones from PigX. As previous phantom experiments revealed, the individual orientation of capsules and the longer distance between Rx and stoma of PigY of 8 cm influence signal strength. However, it was not possible to identify the exact location of the capsules. Additionally, a larger pig mass for PigY compared to PigX, and the relative position in terms of the various surrounding tissues, could have added to the decreased initial RSSI.

Towards the end of the withdrawal process, as the capsules approached the stoma, the variation of the signal power for all insertions decreased, ranging from -28 dBm to -40 dBm. This reduction in signal power variability was observed in each capsule, and could again be due to a number of factors such as increased dominance of a single tissue property, reduction in tissue mass surrounding the capsule or minimised distance to the Rx. The inserted capsules in PigY show an increase in RSSI over the duration of the withdrawal process, while the capsules in PigX remain steadier over the full length of the withdrawal. This is caused by the different internal anatomy of the pigs, location of the stoma and the previously mentioned effects.

During withdrawal, an increase and decrease in RSSI for each inserted capsule was noticed, but during the fixed position the signal remained mostly steady, with less variation in RSSI. The second insertion of each capsule showed an offset compared with the first run, but it more or less followed the pattern of the first insertion. The offset of each insertion, despite the use of the same capsule, was most likely to have

been caused by the natural movement of the small bowel, which alters with each insertion so that no two insertions are completely identical.

The RSSI observed during the trials was also lower than in the phantom tests, because more body mass surrounded the antenna inside the pig.

In general, the insertion and withdrawal process for the tethered capsules could be done easily, since the small bowel was well lubricated, making for easy manoeuvring.

7.2.1.2 Post-mortem pigs

Figure 7.7 repeats the offset of the first and second insertions while also showing a large variation in signal strength of -30 dBm to -55 dBm up to the last stable position of the withdrawal process. There, the variation is much less, -32 dBm to -37.5 dBm with one deviation, compared with the results for the living pigs. Although the Rx was placed 15 cm further away from PM2 than PM1, the signal strength measured was mostly stronger than the one from the PM1 insertions. Generally, signal strength shifted by about -6 dBm to a lower RSSI compared with the living pigs. One reason for this could be the fact, that PM1 has been longer dead than PM2, when the insertions were made.

The first two insertions and withdrawals gave similar results to those for the living pigs, but with the cessation of the living functions, the natural lubrication of the small bowel also stopped. It also started to contract, making insertion more difficult with each capsule. When the second capsule was inserted, at 70 minutes after time of death of PM1 and 45 minutes after time of death of PM2, it was very difficult to reach the 60 cm mark. The signal transmission results show a very marked signal strength drop during the first and second withdrawal sections, when the second capsule (Cap7) was inserted (these were the third and fourth insertions for each pig). In particular, the final insertion represented a very low shift to up to -78 dBm during the second withdrawal process. This is probably because the capsules were forced into position and then suddenly released when withdrawn. The orientation of the capsule had probably changed, causing a higher signal variation than in the previous runs. When the stable position was reached, the signal recovered again and remained steady.

7.2.1.3 Living and post-mortem pig comparison

Figure 7.8 shows a direct comparison of the change in RSSI in the same living and euthanised pigs (PigY and PM2) with the same body mass and distance to Rx. The Cap6 insertions represent constant and comparable signal strength throughout the

withdrawal process, with an initial variation of -34 dBm to -46 dBm, finishing with a -31 dBm to -37 dBm shift. Cap7 shows a lower RSSI in PigY, with a larger variation of -31 dBm to -58 dBm at the start and a steadily increasing signal strength throughout the withdrawal process until it finishes within the Cap6 range. The only major difference can be seen in the post-mortem pig (PM2), where Cap7 shows the drop in RSSI at the second withdrawal stage for the second insertion, as discussed in Section 7.2.1.2.

The small bowel of the euthanised PigX where the *in-vivo* capsule trial took place was excised during a post-mortem gross visualisation, as shown in Figure 7.9. This section of tissue was inspected for presence of burns, inflammation and cuts, and no evidence of tissue damage was observed.

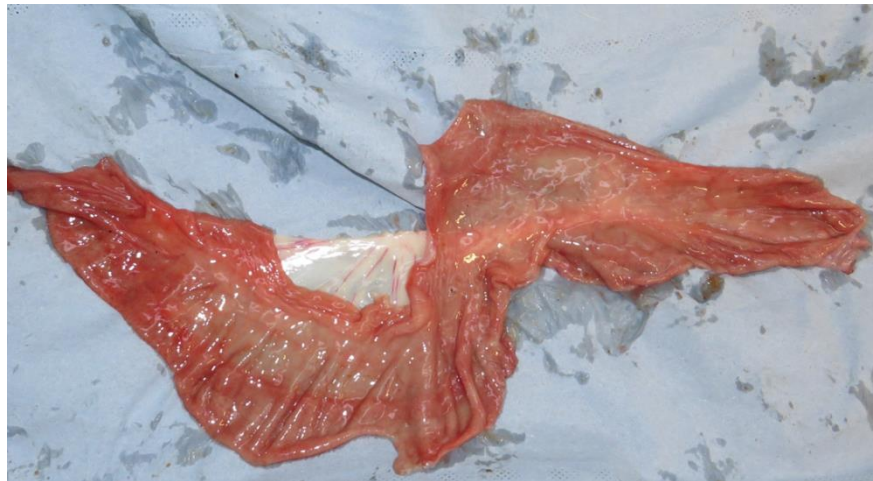


Figure 7.9: Removed section of the small bowel of PigX that was in contact with the transmitting capsules

7.2.1.4 Summary of static power level experiments

The variation in RSSI between the capsules was mainly due to orientation, but, equally, distance between Tx and Rx, manufacturing tolerances, position and pig anatomy also influenced the received signal strength. The capsules all varied with respect to signal strength, but all of them showed a very low PER and BER, even at a low RSSI of -75 dBm. The change in capsule orientation, as previously observed in the phantom tests, together with the dielectric tissue property variation, produced the largest detuning effects.

The signals were stronger and more consistent in the living pigs than in the euthanised animals. The experiments became more challenging to perform once the pig had been euthanised, since the lack of living functions stopped the lubrication of the small bowel

and let it contract, making each insertion more difficult as time went on. The post-mortem insertion results were less steady and strong signal attenuation was observed during the withdrawal sections of the 3rd and 4th insertion. When the capsule was kept in a steady position the power became more stable again.

No temperature increase was observed in any of the insertions. During the post-mortem experiments, temperature decreased, due to a lack of living functions.

These results strongly suggest that the concept of the conformal antenna offers a good alternative to other internal antennas in current CE systems.

7.2.2 Variable power – Group II

The second part of the experiments was conducted with the capsules operating at variable output power levels, while fixed in a single position. The experiment was performed twice, with a different capsule each time. The temperature and RF data were continuously logged in MS Excel files throughout this trial, and the experiment lasted approximately 80 mins per pig. Figures 7.10 to 7.12 show the resulting graphs of the measurements of the two Group II capsules inserted into both live and post-mortem pigs. The first three graphs indicate the change of RSSI over time within the small bowel. The fourth displays the signal strength for each power level with an approximate slope value for each curve. During these longer experiments, a PER and BER of less than 10^{-5} for every power level was observed for each inserted capsule. No temperature increase was observed by the on-board thermistors at any point during the investigation, and this conforms to SAR standards [14, 150].

Group II – PigX and PigY (living)

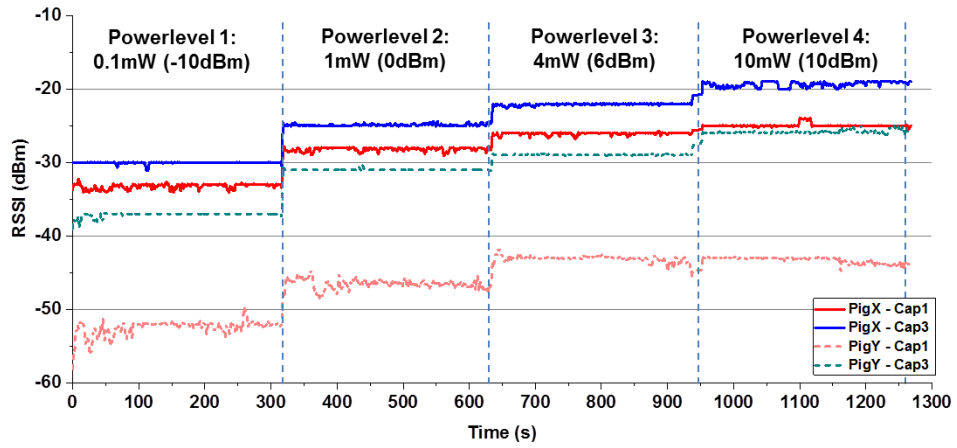


Figure 7.10: RSSI of two Group II capsules in both living pigs (PigX and PigY)

Group II – PM1 and PM2 (euthanised)

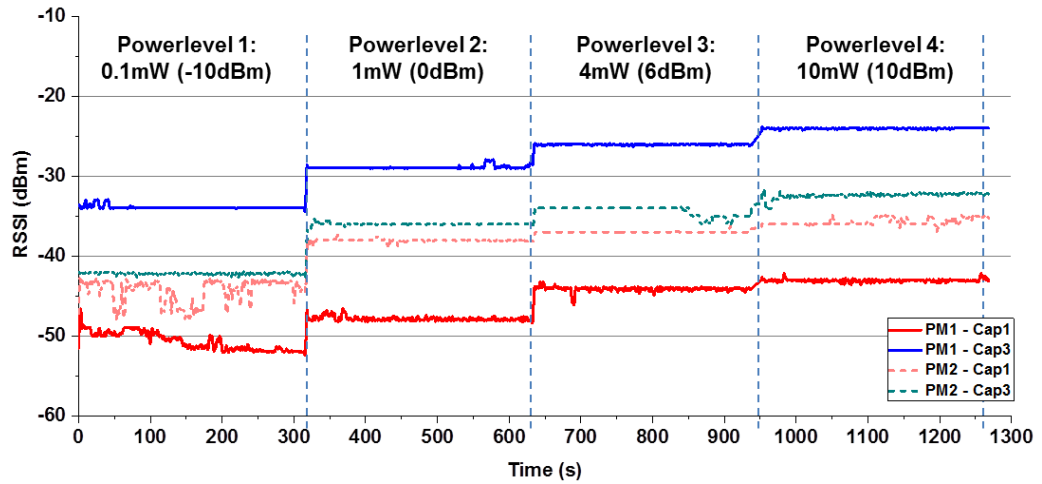


Figure 7.11: RSSI of two Group II capsules in both euthanised pigs (PM1 and PM2)

Group II – PM2 and PigY

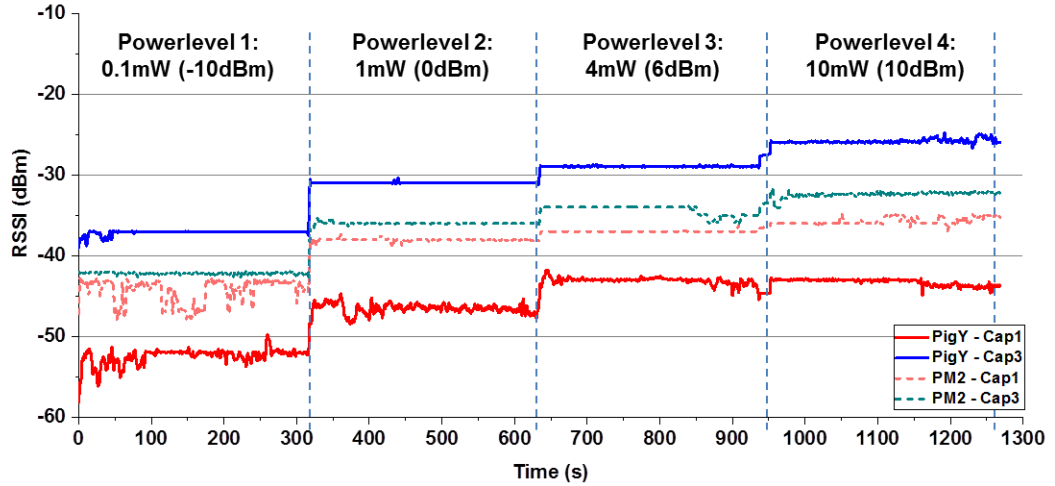


Figure 7.12: RSSI of two Group II capsules in PM2 and PigY (same pig)

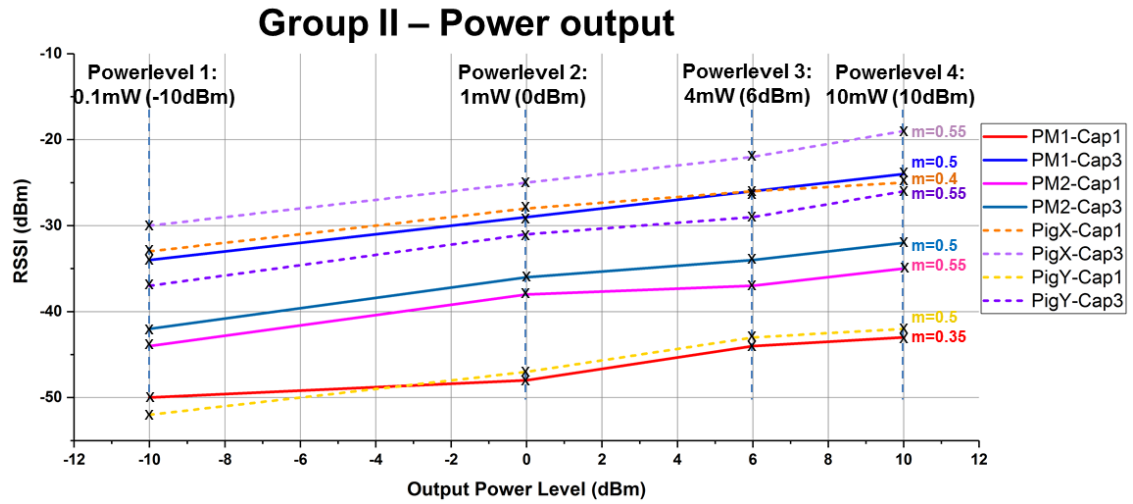


Figure 7.13: Signal strength indicator for each power level with an approximated slope value for each curve

7.2.2.1 Live pigs

Figure 7.10 illustrates the proportionate increase of the RSSI when the power level was increased in stages. The rise in power from the first (-10 dBm) to the second level (0 dBm) represents the biggest power increase of 5 dBm. The step from 0 to 6 dBm generated a 2 to 3 dBm increase, and the one from 6 to 10 dBm an increase of 2 dBm, confirming the observation of the phantom test. Figure 7.13 shows the approximate increase in signal strength, together with the slope value for each insertion. The signal increase shows almost linear behaviour throughout the power increase cycle.

The noisy signal at the start of some of the capsule insertions is due to concurrent activity on the laptop and movement close to the pig set-up, which led to a variation in the power the Rx module received.

As seen in the phantom test, the received signal strength of Cap1 is 9 dBm lower compared to Cap3. An offset between Cap1 and Cap3 of -3 dBm is also seen in PigX, increasing to -15 dBm in PigY. As previously reported in Section 7.2, the change in RSSI in the different pigs is caused by the different porcine anatomy and different surrounding tissue permittivities, capsule orientation post- insertion, the individual pigs' mass and the different distances between Tx and Rx. The placement distance between the Rx and PigX's stoma is extended by 8 cm for PigY which, according to the phantom tests, would cause a signal attenuation of -2 to -6 dBm at 60 cm for -10 dBm output power.

7.2.2.2 *Post-mortem pigs*

Figure 7.11 shows a similar trend in increasing RSSI that was seen in the live pigs, PigX and PigY. Because rigor mortis was already advanced in the animals at the time of the experiment, the small bowel became less lubricated and more contracted with every insertion. So it was only just about possible to insert the devices as far as the 60 cm mark. Cap1 was the fifth and Cap3 the sixth insertion into both euthanised pigs.

The graph indicates shows signal attenuation for three of the four insertions within the euthanised pigs compared with the live animals. Only Cap1 in PM2 exhibits a shift of 8 dBm to a higher RSSI, although the distance between Rx and stoma in PigY is extended by 15 cm compared with PigX, so potential signal attenuation would be expected. The variation in capsule orientation, probably caused by the challenging insertion, is likely to have led to the shift in signal strength, which could be up to -18 dBm according to the phantom tests.

Cap1 displayed a noisy signal at the start of the cycle, Cap3 throughout the cycle, due to concurrent activity on the laptop and movement close to the pig set-up, as previously stated.

Figure 7.12 compares the same pig directly in live and post-mortem states. The signal strength of Cap3 is attenuated in PM2, but increased in Cap1, which could be attributed to the location and orientation of the capsules, although it refers to the same pig.

7.2.2.3 *Temperature measurements*

During all experiments, the on-board thermistors (A to D) detected only a very small temperature rise of less than 1°C. Figures 7.14 and 7.15 show the recorded temperature data during the Group II capsules experiments. The offset of each embedded on-board thermistor was caused by the individual position of the thermistor within the capsule shell. Some were pushed slightly further in than others, and are covered in more epoxy. A minimal temperature rise can be seen during the insertion of Cap1 in Pig Y, but the temperature generally remained steady, with no particular peaks observed.

The insertion of Cap3 into PM1 revealed a clear temperature drop, due to the greater time since death of PM1.

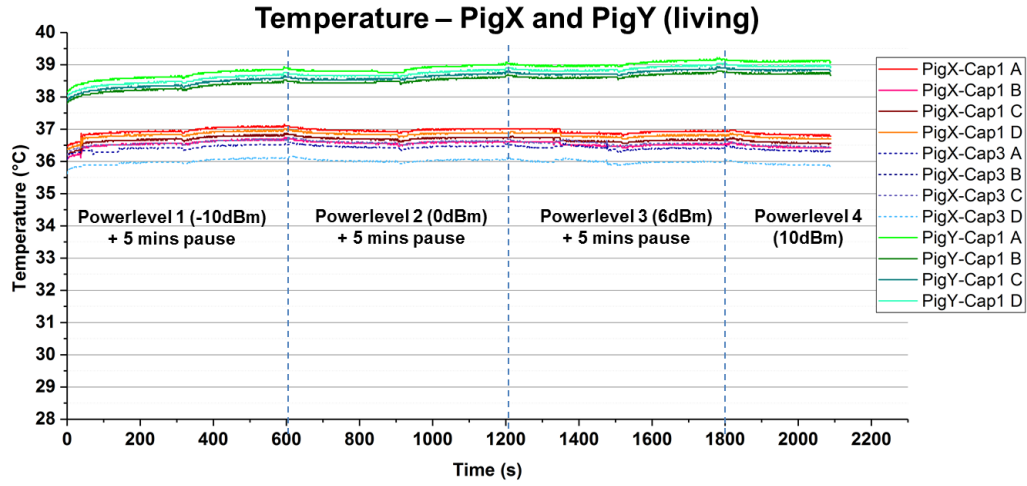


Figure 7.14: Measured temperature of the four on-board thermistors (A-D) over the full power increase cycle of each insertion into the live pigs

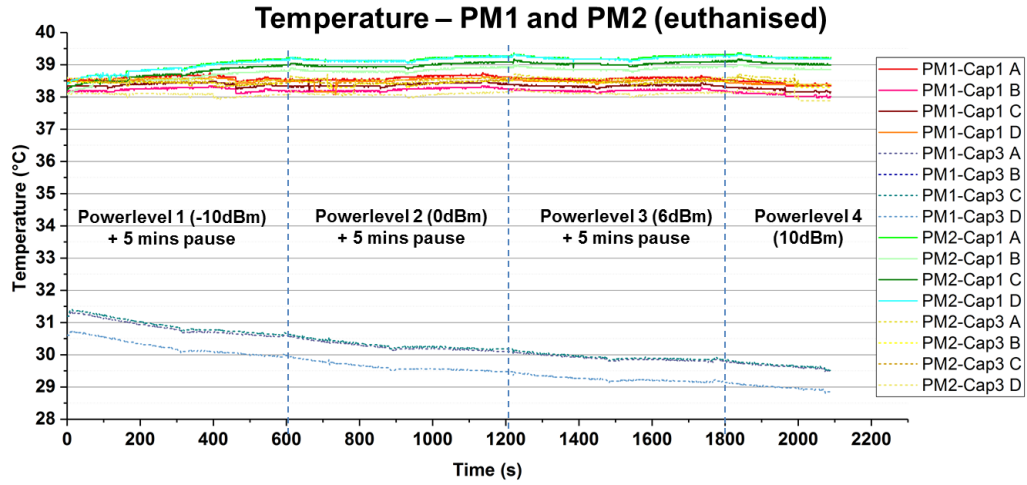


Figure 7.15: Measured temperature of the four on-board thermistors (A-D) over the full power increase cycle of each insertion into the euthanised pigs.

7.2.2.4 Summary

The increase in RSSI confirms the impact of the transmission power of the Tx on the transmitted signal strength. Good transmission performance was observed even at the lowest power of -10 dBm, as shown by the low number of lost or faulty data packets (PER and BER of less than 10^{-5}). Power could not be tested below -10 dBm, since this is the on-board transceiver module's lowest programmable power level.

In each pig type, the Cap1 data transmission displayed lower signal strength than Cap3, in keeping with the phantom experiments.

The thermistors detected a temperature rise of less than 1°C, conforming to SAR standards. This result confirmed the SAR simulation result shown in Section 3.2.2.1. The highest SAR value of 0.08 W/kg was well below the FCC recommended limit of 2 W/kg for 10 grams of tissue mass with an antenna excitation power of 1 mW. The highest power (10 mW) used was still well below the maximum power allowed in terms of SAR restrictions.

For more accurate PER and BER results, longer tests would have to be performed to resemble the time a capsule needs to travel through the body.

Post-mortem results differed from those for the live pigs, but still showed valid and useful outcomes. Temperature measurements for the euthanised pigs showed the relative speed at which the body cools, which could lead to the wrong results if SAR measurements are to be performed. The post-mortem pigs had more in common with the phantom examinations due to their lack of living functions.

7.3 CONCLUSIONS

All capsules demonstrated a satisfactory performance at a data rate of 16 kbps in *in-vivo* and phantom experiments. Data transmission was achieved with low error rates ($<10^{-3}$) and a temperature increase of less than 1°C was detected for the tissue surrounding the antenna.

RSSI as low as -54 dBm with low Tx output power levels of -10 dBm still offer a low PER and BER irrespective of the location of the capsule within the small bowel. The CC1110 receiver exhibits a sensitivity of -95 dBm, which provides us with a wider margin for varying operation conditions.

The signal strength of the inserted capsules varies with insertion depth and orientation to the receiver and with tissue surrounding the capsules as well as insertion depth.

The *in-vivo* results successfully demonstrate the concept of placing a conformal antenna on the outside of an ingestible capsule and the ability of transmitting data wirelessly from an ingestible medical device from within a patient's body, without causing harmful temperature effects to the human body tissue.

7.3.1 Polarisation and radiation pattern

The polarisation of the transmitting antenna should ideally be circular. The designed antenna displays an elliptical polarisation with major axis of polarisation in the

horizontal direction, using Kraus' approach [90]. The potential mismatch is however offset by the almost omnidirectional radiation of the transmitter. However, the data transmission results show that this mismatch is overcome reasonably. Additionally, the tissue surrounding the antenna will affect the polarisation of the transmitter. The communication link still returns however good results.

The antenna surrounded by tissue offers an almost omnidirectional radiation pattern. The radiation modes of the capsule helix antenna are highly likely to be a combination of normal and axial modes as can be deduced from [69]. This can also be attributed due to the probable presence of both normal and axial transmission modes and can also be to the fact that the array effect is minimal due to the spacing between the turns of helix. Thus, it does not represent a perfect 3D sphere, as there is a minimal attenuation visible along the z-axis. Although it is not fully omnidirectional, the communication link has only been minimally affected.

CHAPTER 8 CONCLUSIONS AND FUTURE WORK

Capsule endoscopy offers a good alternative to traditional scope-based endoscopy. It is a painless, straightforward procedure, causing patients minimal discomfort. Previously developed wireless capsule endoscopes incorporated internal antennas which took up a large part of the available internal capsule space, reducing the chances of embedding more modalities.

The work performed within this thesis involved the design, manufacture, characterization and testing *in-silico*, *in-vitro* and *in-vivo*, of a conformal antenna for wireless transmission of information from inside the body. Taking into account a wide range of technical, and health and safety concerns, the focus was on the antenna, one of the most challenging elements of an ingestible data telemetry device, and the accompanying embedded electronic system. As well as the common antenna design challenges, such as miniaturisation, frequency tuning and decreased radiation efficiency, particular attention was paid to the coupling of the EM field with the biological lossy tissues in terms of SAR and biocompatibility. The functionality, safety and reliability of the wireless communications were experimentally assessed via *in-vitro* tests and *in-vivo* trials.

Wireless communication for the prototypes across biological tissues of up to 80 cm was tested. This is usually sufficient to exchange data between an ingested device inside the human body and the receiving element nearby.

The investigations performed improved understanding of the performance characteristics of capsule antennas and their requirements and challenges. The developed capsule telemetry system required the study of several aspects, such as antenna optimisation within lossy human tissue environments, packaging considerations and maintaining patient safety, and the next section analyses the outcome of this thesis.

8.1 CONCLUSIONS

Chapters 2 and 3 summarise the available applications for capsule endoscopy and discuss the influence of the human body on radiation characteristics. This analysis of antennas in lossy materials was important for identifying the challenges of the design of ingestible antenna devices. Focusing on the more complex, dispersive and lossy characteristics for EM propagation of the human body, different human body model

options were reviewed to form a basis for the further simulations and physical measurements. This review created a better understanding of the subject for designing antennas surrounded by lossy biological materials.

The antenna design and simulation processes are described in Chapter 4. The design strategy mentioned in Chapter 3 was applied and different aspects, including miniaturisation techniques, antenna tuning and SAR investigations, were analysed. The initial conformal meander design approach offered a quick and easy method to analyse the prototype in free space and to compare simulation to the measurement results. A human tissue model was investigated to be able to test the antenna device within a body tissue environment. Following the meander analysis within free space, an additional helical antenna design was added to compare both antenna performances. Both antennas were further optimised to radiate at the required frequency range of 433 MHz and a SMA cable was attached, replacing the initial SMA connector. The simulation and measurements showed good agreement and displayed wide fractional bandwidths of 51.3% (Meander) and 20.8% (Helix). During the simulations and measurements the results were influenced by the connected cable, resulting in frequency shifts, but the future devices will be wireless and not affected by connected tethers. In the final step, the SMA cable was removed and the helix antenna was optimised during the simulation process, including the internal GND plane and connection to the antenna. The final antenna design is radiating at 433 MHz within muscle-like tissue and is displaying a bandwidth of 20 MHz and an almost omnidirectional radiation pattern. According to the simulations, the SAR of the designed antenna stayed below the recommended values.

Chapter 5 includes the integration, packaging and assembly of all the components of the final prototype, including the manufacturing of the capsules and their integration with the necessary electronic components, the RF transceiver, PCBs and thermistors. The prototypes were connected to tether bundle that provided the power for the MCU, a way to retrieve the capsule from the pigs during the *in-vivo* experiments and facilitate the temperature data transmission. The chosen RF transceiver unit from TI (CC1310) offers a data rate of up to 4 Mbps, which had to be reduced to 16 Kbps, due to the available receiver set-up and firmware. Six capsule devices were manufactured and assembled and thermistors were embedded into each capsule shell, to be able to record any temperature increase during the experiments. The coating process of the biocompatible insulation layer over the full length of the capsule was described in detail and the data transmission programs were established. The capsule prototypes were programmed to

send data packets composed of a message header, a package counter, a time stamp and the Received Signal Strength Indicator (RSSI), with a maximum data payload of 255 bytes per packet. The six fabricated capsules were divided into two groups of three, only differing in their programmed data transmission modes. One group transferred data packages at a constant power level of 0 dBm and the other group was programmed to transmit at multiple power levels of -10, 0, 6 and 10 dBm.

The *in-vitro* characterisation of the full capsule telemetry system is detailed in Chapter 6. All six prototypes were embedded into the prepared body phantom material with dielectric muscle tissue properties and their radiation and data transmission properties were evaluated. The two programmed capsule groups underwent three different measurements: (1) Continuous data transfer, (2) data transfer with increasing separation of Tx and Rx and (3) radiation pattern measurements. All capsules showed a promising performance during each experiment. All packets transmitted and received resulted in a PER of less than 10^{-3} and a BER of less than 10^{-5} , sufficient for a low-error data transfer with this length and number of data packets. During the increasing separation measurements, signal attenuation was observed, as expected. The radiation pattern measurements identified a large drop in signal strength of up to -18 dBm, originating from the connected tether bundle and the antenna connection to the internal PCB. The thermistor data was recorded throughout the measurements, but no temperature increase was observed. The link budget was established and the estimated path loss resulted in -70 dBm. The phantom measurements provided an effective evaluation method for testing the antenna performance before the *in-vivo* experiments described in Chapter 7. The *in-vitro* experiments captured the known problems of measuring small antennas fed by coaxial cables, and the results were taken into account during the *in-vivo* measurements. The performance of the capsule prototypes was examined using *in-vivo* porcine models to validate the functionality of the telemetry system under real tissue conditions. The experiments were performed on three pigs, living and euthanised. The capsule prototypes were inserted through a stoma 60 cm deep and the data packets were received by the TI receiver set-up placed on a nearby trolley. All capsules demonstrated a satisfactory performance at a data rate of 16 Kbps in the *in-vivo* experiments. Data transmission was achieved with low error rates ($<10^{-3}$) and a temperature increase of less than 1°C was detected for the tissue surrounding the antenna. A low signal strength of only -54 dBm still provided an effective data transfer, irrespective of the capsule's location or orientation.

8.2 NOVEL CONTRIBUTIONS

1. A proof-of-concept device for wireless data transmission in capsule endoscopy was developed. The design, manufacture and performance characterisation of a helical antenna conformally placed outside a 3D printed endoscopic capsule was introduced, and the goal of reducing internal space constraints achieved. The antenna shape offers an easy way of altering its dimensions to change carrier frequency and improve its performance. This thesis combines different subareas, such as electromagnetics, electronic design and medical health and safety challenges.
2. *In-silico*, *in-vitro* and *in-vivo* characterisation of the full ingestible telemetry system using pigs was performed, successfully demonstrating the feasibility of the system. Previously designed conformal antennas covered either most of the capsule surface, representing larger dimensions due to the greater size of the capsule or radiating at higher frequencies [6-8, 57, 65, 77, 145]. Liu *et al.* and Das *et al.* present conformal antennas radiating at 2.4 GHz and 915 MHz and demonstrated their performance in simple body models made up of a liquid mixture and minced pork respectively [9, 77]. None of the state-of-the-art conformal ingestible antennas has yet been investigated completely *in-vivo* together with a data transmission chip and temperature/SAR measurements. Figure 8.1 visualises the internal space saved (25%) when using a conformal antenna design, providing a big advantage for future wireless capsule telemetry developments.

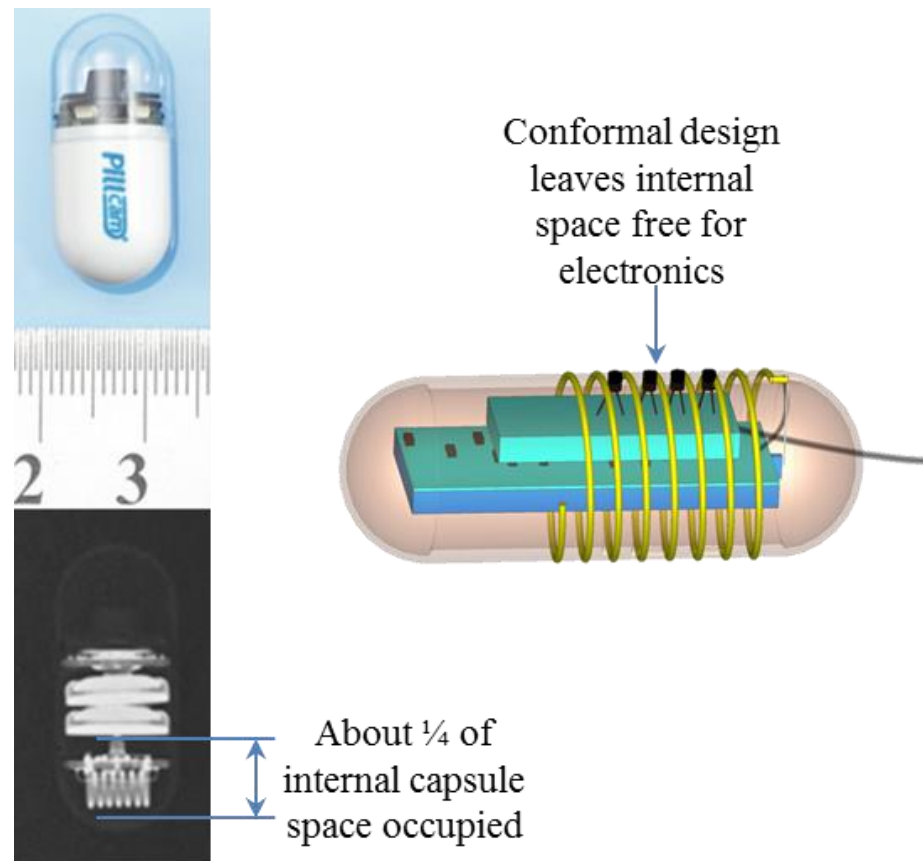


Figure 8.1: Comparison of volume used by internal PillCam® antenna [41] compared to the, in this thesis, developed conformal antenna design, showing the gained internal space

3. As part of the entire system, thermistors served as temperature monitors to maintain the system safety. This solution provided an initial facility for measuring temperature increase to determine the SAR when using conformal antennas.
4. Safe and reliable data communication was established from different parts of the small bowel in dead and live pigs, with values of transmission power complying with safety regulations.
5. The lack of localised tissue heating in conjunction with low power transmission shows that conformal antennas are a viable technology for ingestible and short-term implantable medical devices such as capsule endoscopes.
6. To protect the antenna from the surrounding tissue and maintain biocompatibility, a moulding process to add an insulating layer made of epoxy was proposed. This can be used for future prototypes of capsule endoscopic

devices. A layer of Parylene-C was additionally deposited, as this is commonly used as biocompatible and bio-stable coating material for biomedical devices.

These results add to the development of novel and miniaturised capsule endoscopy devices, and constitute a step towards improved healthcare and wireless capsule endoscopy. The current antenna system was developed as a proof-of-concept to validate the useful and efficient use of the shell as a support for the antenna. Different (more complex) designs can be incorporated at a later stage.

Batteries were not considered in this thesis, since their influence on signal transmission has previously been discussed at length elsewhere, including in Das *et al.* and Izdebski *et al.* [57, 65]. However, the wireless data transmission part of the power consumption of the system is not expected to exceed 10 mW.

This thesis does not just show the functioning of easily manufactured conformal antennas in conjunction with commercially available transceiver modules. It also offers valuable clues as to the differences between living and euthanised pigs, and the influence of the physiological condition of the gut on trial experiments which test data transfer capsules in the future. Using dead pigs becomes more and more difficult the more time has elapsed since death. Temperature measurements taken on euthanised pigs show their bodies cool relatively quickly, potentially leading to the wrong results if SAR measurements are to be performed in the future and the lack of natural lubrication making it more difficult for capsule insertions and manoeuvrability.

8.3 FUTURE WORK

In this thesis, many aspects related to ingestible data telemetry systems have been addressed. However, more research could be considered for further investigations into the following propositions:

1. In terms of the limitations of the current design, better physical connectivity between both PCBs and the RF board to the antenna must be implemented to improve reliability and further reduce the effort required to assemble the devices. Circular substrates can be used to assemble a PCB within the capsule, as seen in [150], freeing up more battery space.

2. Different antenna designs and fabrication processes, such as the use of flexible substrates to form an antenna [161] or the printing of conductive structures onto the capsule surface [162], could be investigated for future wireless endoscopic telemetry devices.
3. The post-mortem pigs have more in common with the phantom examinations due to their lack of living functions. This case needs to be investigated in further trials. In future investigations, running the data transfer experiments for longer could give more information about signal attenuation after death. Will it decrease more with time and if it does, linearly or logarithmically? Regarding future SONOPILL applications, interference tests with ultrasound devices need to be targeted, investigating any potential issues when combining RF data transmission with ultrasonic imaging techniques.
4. Future work will aim to implement different communication protocols and carrier frequencies. The chosen TI transceiver chip offers a data rate of up to 4 Mbps. Improving the receiver and firmware will help to exploit the full capacity of the system. Additionally, the thermistors can be connected to the microcontroller to send the recorded temperature data wirelessly to the receiver, instead of using tethers.
5. Future applications will be completely wireless and unaffected by a tether; hence the measured radiation pattern will be more likely to represent the simulated device's almost omnidirectional radiation. For applications which do use a tether, an alternative data transmission mode with the data transmission cables in the tether can be used if necessary, if there is any directional loss of data.

APPENDIX

A1: LINK-BUDGET ANALYSIS

The link budget analysis gives us an initial idea of the communications capacity of the proposed antenna and external Rx, as well as a better insight into the in-to-out-body signal propagation. Figure 6.9 visualises the communication link in terms of transmission, propagation and reception.

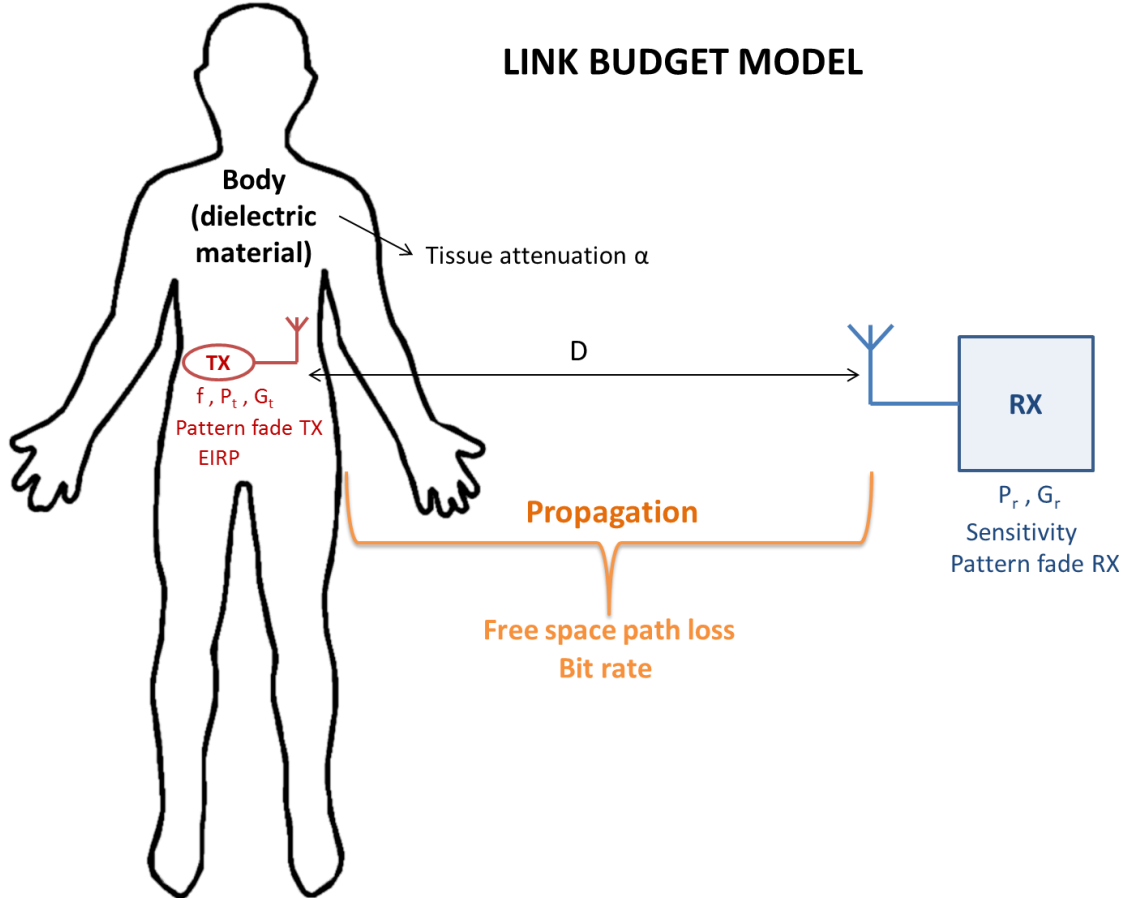


Figure A.1: Link-budget model for a CE system

In the real human body the different tissue layers cause variations in signal propagation, due to the reflection and attenuation of the waves caused by the lossy properties and the interfaces of layers [59]. This leads to a variable path loss values in the case of ingestible capsules. Because of the complexity of the human body, only the homogenous phantom material and a steady distance of 0.6 m are used in this thesis to obtain an estimated link budget result. Table 6.2 summarises the parameters, as well as the calculated values of the link budget calculation.

TABLE A.1: Link budget analysis between the Tx and the Rx

Tx		Rx	
Frequency, f (MHz)	433	Rx Antenna Gain, G_r (dBi)	0
Tx Power, P_t (dBm)	10	Distance to Tx, D (m)	0.6
Tx Antenna Gain, G_t (dBi) free space	-12	Temperature (K)	310
Tx Antenna Gain, G_t (dBi) phantom	-35	Boltzmann constant, k	1.38×10^{-23}
Wavelength in free space, λ (m)	0.7	Noise power density, N_0 (dB/Hz)	-203
Wavelength in phantom, λ (m)	0.087	Polarisation Loss, L_p (dB)	0.65
		Pattern Fade, PF (dB)	6
Propagation		Signal Quality	
EIRP (dBW)	-54.9	Bit Error Rate, BER	10^{-5}
Free Space Path Loss, FSPL (dB)	32.74	Bit Rate kBytes/s	2.04
Path Loss (dBm)	-70	C/N ratio (dB/Hz)	105.67
Tissue Attenuation, A (dB)	1.68		

The total gain values of the Tx antenna were retrieved from the CST simulation results and the wavelengths were calculated using equations (20) and (21). The Rx antenna totgain was specified in the TI CC1110 data sheet. The temperature and Boltzmann constant are fixed values and were used to calculate N_0 using equation (31). Based on [57] the polarization loss and pattern fade was estimated to the values given in Table 6.2. The EIRP was calculated using (26), but first converting the gain to mW, to be able to better convert it to dBW. The FSPL is calculated using (23) and inserting all necessary parameters. The tissue attenuation A is calculated using (25). The BER was recorded during the experiments.

The maximum available power (dBm) for the free-space link can be calculated using the Friis formula [99]:

$$P_r = P_t \frac{G_t G_r \lambda^2}{(4\pi D)^2} \quad [W] \quad (22)$$

where P_t is the transmitting power, G_t and G_r the Tx and Rx gain, λ the wavelength and D the distance between Tx and Rx.

The Free Space Path Loss (FSPL) describes the signal attenuation at a given frequency between a transmitting and a receiving antenna as a function of propagation distance in free space.

$$FSPL = 20 \log_{10}(D) + 20 \log_{10}(f) - 27.55 \quad [dB] \quad (23)$$

where D is specified in meters and f in MHz. To evaluate the effects of human body tissue on the wave attenuation, the theoretical path loss model can be used. The path

loss from an ingestible radiator to the receiver comprises the free space path loss, attenuation loss, polarisation loss, pattern fade and loss due to reflections from the boundaries between the different tissue layers [158].

The absorption coefficient for the E-field for each tissue:

$$A_{\alpha} = \exp(-\alpha D) \quad (24)$$

The absorption coefficient for the power for each tissue:

$$A_{\alpha} = \exp(2\alpha D) \quad (25)$$

The Effective Isotropic Radiated Power (EIRP) is given by:

$$EIRP = P_t G_t \quad (26)$$

The reflection coefficient is given by:

$$\Gamma = \frac{\eta_2 - \eta_1}{\eta_2 + \eta_1} \quad (27)$$

with the intrinsic impedance of the medium being:

$$\eta = \sqrt{\frac{\mu}{\varepsilon}} \text{ or } \eta = \sqrt{\frac{j\omega\mu}{\sigma + j\omega\varepsilon}} \quad (28)$$

which leads to the reflection loss:

$$L_r = 20 \log(\Gamma) \quad (29)$$

The carrier C to noise N ratio model is defined as:

$$\frac{C}{N} = PL - N_0 - L_p - A \quad \left[\frac{dB}{Hz} \right] \quad (30)$$

Where L_p is the polarisation loss, A the tissue attenuation and N_0 the noise power density defined by:

$$N_0 = 10 \log_{10}(k) + \log_{10}(T_i) \quad \left[\frac{dB}{Hz} \right] \quad (31)$$

with k as the Boltzmann constant (1.38×10^{-23}). T_i is the transmission coefficient and defined by:

$$T_i = T_0(NF - 1) \quad [K] \quad (32)$$

where T_0 is the ambient temperature of 310 K and NF the noise figure of the receiver.

More detailed path loss models established by Das *et al.*, Kurup *et al.*, Rajagopalan *et al.*, and Chrysikos *et al.* can be found in [57-59, 110, 159].

The path loss (PL) for this signal propagation model can be calculated using equation (33) [56, 57].

$$PL(dB) = P_t + G_t + G_r - FSPL - PF * 2 \quad (33)$$

The PL for this particular propagation model is -70 dBm with a link margin of 25 dBm, due to a Rx sensitivity of -95 dBm.

REFERENCES

- [1] G. Iddan, G. Meron, A. Glukhovsky, and P. Swain, "Wireless capsule endoscopy," *Nature*, 10.1038/35013140 vol. 405, no. 6785, pp. 417-417, 05/25/print 2000.
- [2] V. K. Sharma, "The Future Is Wireless: Advances in Wireless Diagnostic and Therapeutic Technologies in Gastroenterology," *Gastroenterology*, vol. 137, no. 2, pp. 434-439, 8// 2009.
- [3] A. Koulaouzidis, D. K. Iakovidis, A. Karargyris, and E. Rondonotti, "Wireless endoscopy in 2020: Will it still be a capsule?," *World Journal of Gastroenterology : WJG*, vol. 21, no. 17, pp. 5119-5130, 2015.
- [4] Sonopill. (2016, 05/02/). *Sonopill - Future of Capsule Endoscopy*. Available: <http://sonopill.dundee.ac.uk/>
- [5] J. L. Toennies, G. Tortora, M. Simi, P. Valdastrì, and R. J. Webster, "Swallowable medical devices for diagnosis and surgery: the state of the art," *Proceedings of the Institution of Mechanical Engineers Part C-Journal of Mechanical Engineering Science*, vol. 224, no. C7, pp. 1397-1414, 2010.
- [6] L. Sang Heun *et al.*, "A Wideband Spiral Antenna for Ingestible Capsule Endoscope Systems: Experimental Results in a Human Phantom and a Pig," *Biomedical Engineering, IEEE Transactions on*, vol. 58, no. 6, pp. 1734-1741, 2011.
- [7] R. Alrawashdeh, Y. Huang, P. Cao, E. Lim, and Ieee, "A New Small Conformal Antenna for Capsule Endoscopy," in *2013 7th European Conference on Antennas and Propagation*(Proceedings of the European Conference on Antennas and Propagation, New York: Ieee, 2013, pp. 220-223.
- [8] Y. Sumin, K. Kihyun, and N. Sangwook, "Outer-Wall Loop Antenna for Ultrawideband Capsule Endoscope System," *Antennas and Wireless Propagation Letters, IEEE*, vol. 9, pp. 1135-1138, 2010.
- [9] F. Merli, B. Fuchs, and A. K. Skrivervik, "Influence of insulation for implanted antennas," in *Antennas and Propagation, 2009. EuCAP 2009. 3rd European Conference on*, 2009, pp. 196-199.
- [10] A. K. Skrivervik, "Implantable antennas: The challenge of efficiency," in *Antennas and Propagation (EuCAP), 2013 7th European Conference on*, 2013, pp. 3627-3631.
- [11] P. Izdebski, H. Rajagopalan, and Y. Rahmat-Samii, "Ingestible capsule antenna for bio-telemetry," in *iWAT 2009. IEEE International Workshop on Antenna Technology, 2009*, 2009, pp. 1-4.
- [12] A. Kiourti, K. A. Psathas, and K. S. Nikita, "Implantable and Ingestible Medical Devices With Wireless Telemetry Functionalities: A Review of Current Status and Challenges," (in English), *Bioelectromagnetics*, Review vol. 35, no. 1, pp. 1-15, Jan 2014.
- [13] "Guidelines for limiting exposure to time-varying electric, magnetic, and electromagnetic fields (up to 300 GHz). International Commission on Non-Ionizing Radiation Protection," (in eng), *Health Phys*, vol. 74, no. 4, pp. 494-522, Apr 1998.
- [14] "IEEE Standard for Safety Levels with Respect to Human Exposure to Radio Frequency Electromagnetic Fields, 3 kHz to 300 GHz," *IEEE Std C95.1-2005 (Revision of IEEE Std C95.1-1991)*, pp. 1-238, 2006.
- [15] E. G. Lim, Z. Wang, J. H. Chen, T. Tillo, and K. L. Man, "Electromagnetic wave propagation of wireless capsule endoscopy in human body," (in English),

Journal of Central South University, Article vol. 20, no. 10, pp. 2650-2656, Oct 2013.

- [16] A. Moglia, A. Mencias, P. Dario, and A. Cuschieri, "Capsule endoscopy: progress update and challenges ahead," (in eng), *Nat Rev Gastroenterol Hepatol*, vol. 6, no. 6, pp. 353-62, Jun 2009.
- [17] M. R. Basar, F. Malek, K. M. Juni, M. S. Idris, and M. I. M. Saleh, "Ingestible Wireless Capsule Technology: A Review of Development and Future Indication," *International Journal of Antennas and Propagation*, vol. 2012, p. 14, 2012, Art. no. 807165.
- [18] M. K. Goenka, S. Majumder, and U. Goenka, "Capsule endoscopy: Present status and future expectation," *World Journal of Gastroenterology : WJG*, vol. 20, no. 29, pp. 10024-10037, 2014.
- [19] H. F. McAlindon M. E. , Fleischer D. E., "Fields of Application," in *Video Capsule Endoscopy: A Reference Guide and Atlas* H. F. Keuchel M., Tajiri H., Ed.: Springer Berlin Heidelberg, 2015.
- [20] Z. Li *et al.*, "The Current Main Types of Capsule Endoscopy," in *Handbook of Capsule Endoscopy*, Z. Li, Z. Liao, and M. McAlindon, Eds. Dordrecht: Springer Netherlands, 2014, pp. 5-45.
- [21] G. Ciuti *et al.*, "Frontiers of robotic endoscopic capsules: a review," *Journal of Micro-Bio Robotics*, vol. 11, no. 1, pp. 1-18, 2016// 2016.
- [22] P. Swain, "The future of wireless capsule endoscopy," *World Journal of Gastroenterology : WJG*, vol. 14, no. 26, pp. 4142-4145, 2008.
- [23] A. Wang *et al.*, "Wireless capsule endoscopy," *Gastrointestinal Endoscopy*, vol. 78, no. 6, pp. 805-815, 12// 2013.
- [24] B. A. Whitmer*, R. Michael, and W. Bradley, "Video Capsule Endoscopy: The Past, Present, and Future," vol. - 0, no. - 0, pp. -, 2012.
- [25] D. Bandorski *et al.*, "Contraindications for video capsule endoscopy," *World Journal of Gastroenterology*, vol. 22, no. 45, pp. 9898-9908, 2016.
- [26] J. Thoné, S. Radiom, D. Turgis, R. Carta, G. Gielen, and R. Puers, "Design of a 2 Mbps FSK near-field transmitter for wireless capsule endoscopy," *Sensors and Actuators A: Physical*, vol. 156, no. 1, pp. 43-48, 11// 2009.
- [27] A. Mencias, G. Ciuti, and C. Cavallotti, "Future Developments of Video Capsule Endoscopy: Hardware," in *Video Capsule Endoscopy: A Reference Guide and Atlas*, M. Keuchel, F. Hagenmüller, and H. Tajiri, Eds. Berlin, Heidelberg: Springer Berlin Heidelberg, 2014, pp. 543-556.
- [28] D. Turgis and R. Puers, "Image compression in video radio transmission for capsule endoscopy," *Sensors and Actuators A: Physical*, vol. 123-124, pp. 129-136, 9/23/ 2005.
- [29] T. H. Khan and K. A. Wahid, "Low Power and Low Complexity Compressor for Video Capsule Endoscopy," *IEEE Transactions on Circuits and Systems for Video Technology*, vol. 21, no. 10, pp. 1534-1546, 2011.
- [30] D. Schneider, "New camera chip captures only what it needs," *IEEE Spectrum*, vol. 50, no. 3, pp. 13-14, 2013.
- [31] I. I. Wilding, P. Hirst, and A. Connor, "Development of a new engineering-based capsule for human drug absorption studies," (in eng), *Pharm Sci Technolo Today*, vol. 3, no. 11, pp. 385-392, Nov 01 2000.
- [32] Z. Liao *et al.*, "Feasibility and safety of magnetic-controlled capsule endoscopy system in examination of human stomach: a pilot study in healthy volunteers," *J Interv Gastroenterol*, vol. 2, no. 4, pp. 155-160, 2012.
- [33] P. Valdastris *et al.*, "Wireless therapeutic endoscopic capsule: in vivo experiment," *Endoscopy*, vol. 40, no. 12, p. 979, 2008.

- [34] G. Tortora *et al.*, "Propeller-based wireless device for active capsular endoscopy in the gastric district," (in eng), *Minim Invasive Ther Allied Technol*, vol. 18, no. 5, pp. 280-90, 2009.
- [35] (08 September). Available: <http://www.vector-project.com/>
- [36] D. Fischer, R. Schreiber, D. Levi, and R. Eliakim, "Capsule endoscopy: the localization system," (in eng), *Gastrointest Endosc Clin N Am*, vol. 14, no. 1, pp. 25-31, Jan 2004.
- [37] P. Valdastrì *et al.*, "An implantable ZigBee ready telemetric platform for in vivo monitoring of physiological parameters," *Sensors and Actuators A: Physical*, vol. 142, no. 1, pp. 369-378, 3/10/ 2008.
- [38] P. Valdastrì, A. Menciassi, and P. Dario, "Transmission power requirements for novel ZigBee implants in the gastrointestinal tract," (in eng), *IEEE Trans Biomed Eng*, vol. 55, no. 6, pp. 1705-10, Jun 2008.
- [39] S. Bang *et al.*, "First clinical trial of the "MiRo" capsule endoscope by using a novel transmission technology: electric-field propagation," (in eng), *Gastrointest Endosc*, vol. 69, no. 2, pp. 253-9, Feb 2009.
- [40] A. Koulaouzidis, "Upper oesophageal images and Z-line detection with 2 different small-bowel capsule systems," *World Journal of Gastroenterology : WJG*, vol. 18, no. 41, pp. 6003-6004, 2012.
- [41] N. Kurniawan and M. Keuchel, "Technology," in *Video Capsule Endoscopy: A Reference Guide and Atlas*, M. Keuchel, F. Hagenmüller, and H. Tajiri, Eds. Berlin, Heidelberg: Springer Berlin Heidelberg, 2014, pp. 15-20.
- [42] P. J. Bevelacqua. (2009-2014, August 2014). <http://www.antenna-theory.com/definitions/permittivity.php>. Available: <http://www.antenna-theory.com/>
- [43] A. Kiourti and K. S. Nikita, "A Review of In-Body Biotelemetry Devices: Implantables, Ingestibles, and Injectables," *IEEE Transactions on Biomedical Engineering*, vol. PP, no. 99, pp. 1-1, 2017.
- [44] F. Merli, "Implantable Antennas for Biomedical Applications," EPFL, 2011.
- [45] "IEEE Standard for Local and metropolitan area networks - Part 15.6: Wireless Body Area Networks," *IEEE Std 802.15.6-2012*, pp. 1-271, 2012.
- [46] A. S. Y. Poon, S. O'Driscoll, and T. H. Meng, "Optimal Frequency for Wireless Power Transmission Into Dispersive Tissue," *Antennas and Propagation, IEEE Transactions on*, vol. 58, no. 5, pp. 1739-1750, 2010.
- [47] L. C. Chirwa, P. A. Hammond, S. Roy, and D. R. S. Cumming, "Electromagnetic radiation from ingested sources in the human intestine between 150 MHz and 1.2 GHz," *Biomedical Engineering, IEEE Transactions on*, vol. 50, no. 4, pp. 484-492, 2003.
- [48] M. R. Basar *et al.*, "A novel, high-speed image transmitter for wireless capsule endoscopy," (in English), *Progress in Electromagnetics Research-Pier*, Article vol. 137, pp. 129-147, 2013.
- [49] L. Xu, M. Q. H. Meng, H. Ren, and Y. Chan, "Radiation Characteristics of Ingestible Wireless Devices in Human Intestine Following Radio Frequency Exposure at 430, 800, 1200, and 2400 MHz," *IEEE Transactions on Antennas and Propagation*, vol. 57, no. 8, pp. 2418-2428, 2009.
- [50] M. Keuchel, F. Hagenmüller, and H. Tajiri, *Video Capsule Endoscopy: A Reference Guide and Atlas*. Springer Berlin Heidelberg, 2015.
- [51] T.-S. Kim *et al.*, "Method and apparatus for communication between inside and outside of transmission medium using transmission medium as communication line," ed: Google Patents, 2007.

- [52] M. w. Shen, C. y. Lee, and J. c. Bor, "A 4.0-mW 2-Mbps Programmable BFSK Transmitter For Capsule Endoscope Applications," in *2005 IEEE Asian Solid-State Circuits Conference*, 2005, pp. 245-248.
- [53] Y. Gao *et al.*, "Low-Power Ultrawideband Wireless Telemetry Transceiver for Medical Sensor Applications," *IEEE Transactions on Biomedical Engineering*, vol. 58, no. 3, pp. 768-772, 2011.
- [54] K. Kim, S. Yun, S. Lee, S. Nam, Y. J. Yoon, and C. Cheon, "A design of a high-speed and high-efficiency capsule endoscopy system," (in eng), *IEEE Trans Biomed Eng*, vol. 59, no. 4, pp. 1005-11, Apr 2012.
- [55] W. Xia, K. Saito, M. Takahashi, and K. Ito, "Performances of an Implanted Cavity Slot Antenna Embedded in the Human Arm," *IEEE Transactions on Antennas and Propagation*, vol. 57, no. 4, pp. 894-899, 2009.
- [56] A. Kiourti and K. S. Nikita, "Miniature Scalp-Implantable Antennas for Telemetry in the MICS and ISM Bands: Design, Safety Considerations and Link Budget Analysis," *IEEE Transactions on Antennas and Propagation*, vol. 60, no. 8, pp. 3568-3575, 2012.
- [57] R. Das and H. Yoo, "A Wideband Circularly Polarized Conformal Endoscopic Antenna System for High-Speed Data Transfer," *IEEE Transactions on Antennas and Propagation*, vol. PP, no. 99, pp. 1-1, 2017.
- [58] H. Rajagopalan and Y. Rahmat-Samii, "Link budget analysis and characterization for ingestible capsule antenna," in *Antenna Technology (iWAT), 2010 International Workshop on*, 2010, pp. 1-4.
- [59] D. Kurup, G. Vermeeren, E. Tanghe, W. Joseph, and L. Martens, "In-to-Out Body Antenna-Independent Path Loss Model for Multilayered Tissues and Heterogeneous Medium," *Sensors (Basel, Switzerland)*, vol. 15, no. 1, pp. 408-421, 2015.
- [60] E. R. Committee, "ERC recommendation 70-03 relating to the use of short range devices," ed, 2002.
- [61] A. Kiourti and K. Nikita, "Implantable Antennas: A Tutorial on Design, Fabrication, and In Vitro/In Vivo Testing," *Microwave Magazine, IEEE*, vol. 15, no. 4, pp. 77-91, 2014.
- [62] M. R. Yuce and T. Dissanayake, "Easy-to-Swallow Antenna and Propagation," (in English), *Ieee Microwave Magazine*, Article vol. 14, no. 4, pp. 74-82, Jun 2013.
- [63] K. Kyeol, S. Wonbum, L. Soonyong, and C. Jaehoon, "Design of an antenna for an ingestible capsule endoscope system," in *Network Infrastructure and Digital Content (IC-NIDC), 2012 3rd IEEE International Conference on*, 2012, pp. 62-65.
- [64] F. Merli, L. Bolomey, J. Zurcher, G. Corradini, E. Meurville, and A. K. Skriverviky, "Design, Realization and Measurements of a Miniature Antenna for Implantable Wireless Communication Systems," *Antennas and Propagation, IEEE Transactions on*, vol. 59, no. 10, pp. 3544-3555, 2011.
- [65] P. M. Izdebski, H. Rajagopalan, and Y. Rahmat-Samii, "Conformal Ingestible Capsule Antenna: A Novel Chandelier Meandered Design," *Antennas and Propagation, IEEE Transactions on*, vol. 57, no. 4, pp. 900-909, 2009.
- [66] X. Cheng, D. E. Senior, C. Kim, and Y. K. Yoon, "A Compact Omnidirectional Self-Packaged Patch Antenna With Complementary Split-Ring Resonator Loading for Wireless Endoscope Applications," *IEEE Antennas and Wireless Propagation Letters*, vol. 10, pp. 1532-1535, 2011.

- [67] X. Cheng, J. Wu, R. Blank, D. E. Senior, and Y. K. Yoon, "An Omnidirectional Wrappable Compact Patch Antenna for Wireless Endoscope Applications," *IEEE Antennas and Wireless Propagation Letters*, vol. 11, pp. 1667-1670, 2012.
- [68] Q. Wang, K. Wolf, and D. Plettemeier, "An UWB capsule endoscope antenna design for biomedical communications," in *2010 3rd International Symposium on Applied Sciences in Biomedical and Communication Technologies (ISABEL 2010)*, 2010, pp. 1-6.
- [69] C. A. Balanis, *Antenna Theory - Analysis and Design*. John Wiley & Sons, Inc, 1997.
- [70] E. Marcelli, F. Scalambra, L. Cercenelli, and G. Plicchi, "A new hermetic antenna for wireless transmission systems of implantable medical devices," *Medical Engineering & Physics*, vol. 29, no. 1, pp. 140-147, 1// 2007.
- [71] R. S. Alrawashdeh, Y. Huag, M. Kod, and A. A. B. Sajak, "A Broadband Flexible Implantable Loop Antenna With Complementary Split Ring Resonators," *IEEE Antennas and Wireless Propagation Letters*, vol. 14, pp. 1506-1509, 2015.
- [72] M. M. Suzan, K. Haneda, C. Icheln, A. Khatun, and K. i. Takizawa, "An ultrawideband conformal loop antenna for ingestible capsule endoscope system," in *2016 10th European Conference on Antennas and Propagation (EuCAP)*, 2016, pp. 1-5.
- [73] S. I. Kwak, K. Chang, and Y. J. Yoon, "Small spiral antenna for wideband capsule endoscope system," *Electronics Letters*, vol. 42, no. 23, pp. 1328-1329, 2006.
- [74] S. H. Lee and Y. J. Yoon, "A dual spiral antenna for Ultra-wideband capsule endoscope system," in *2008 International Workshop on Antenna Technology: Small Antennas and Novel Metamaterials*, 2008, pp. 227-230.
- [75] S. H. Lee and Y. J. Yoon, "Fat arm spiral antenna for wideband capsule endoscope systems," in *2010 IEEE Radio and Wireless Symposium (RWS)*, 2010, pp. 579-582.
- [76] L. Sang Heun, C. Kihun, K. Ki Joon, and Y. Young Joong, "A conical spiral antenna for wideband capsule endoscope system," in *2008 IEEE Antennas and Propagation Society International Symposium*, 2008, pp. 1-4.
- [77] C. Liu, Y. X. Guo, and S. Xiao, "Circularly Polarized Helical Antenna for ISM-Band Ingestible Capsule Endoscope Systems," *IEEE Transactions on Antennas and Propagation*, vol. 62, no. 12, pp. 6027-6039, 2014.
- [78] Y. P. Zhang and D. Liu, "Antenna-on-Chip and Antenna-in-Package Solutions to Highly Integrated Millimeter-Wave Devices for Wireless Communications," *IEEE Transactions on Antennas and Propagation*, vol. 57, no. 10, pp. 2830-2841, 2009.
- [79] K. Okabe, W. Lee, Y. Harada, and M. Ishida, "Silicon based on-chip antenna using an LC resonator for near-field RF systems," *Solid-State Electronics*, vol. 67, no. 1, pp. 100-104, 1// 2012.
- [80] B.-J. Gu, W.-H. Lee, K. Sawada, and M. Ishida, "Wireless smart sensor with small spiral antenna on Si-substrate," *Microelectronics Journal*, vol. 42, no. 9, pp. 1066-1073, 9// 2011.
- [81] D.-Y. Shin, Y. Lee, and C. H. Kim, "Performance characterization of screen printed radio frequency identification antennas with silver nanopaste," *Thin Solid Films*, vol. 517, no. 21, pp. 6112-6118, 9/1/ 2009.
- [82] J. Jiang *et al.*, "Fabrication of Transparent Multilayer Circuits by Inkjet Printing," *Advanced Materials*, vol. 28, no. 7, pp. 1420-1426, 2016.

- [83] M. Kubo *et al.*, "Stretchable microfluidic radiofrequency antennas," (in eng), *Adv Mater*, vol. 22, no. 25, pp. 2749-52, Jul 06 2010.
- [84] J. J. Adams *et al.*, "Conformal printing of electrically small antennas on three-dimensional surfaces," (in eng), *Adv Mater*, vol. 23, no. 11, pp. 1335-40, Mar 18 2011.
- [85] S. R. Best, "The radiation properties of electrically small folded spherical helix antennas," *Antennas and Propagation, IEEE Transactions on*, vol. 52, no. 4, pp. 953-960, 2004.
- [86] H. Y. Huang, K. Nieman, P. Y. Chen, M. Ferrari, Y. Hu, and D. Akinwande, "Properties and Applications of Electrically Small Folded Ellipsoidal Helix Antenna," *Ieee Antennas and Wireless Propagation Letters*, vol. 11, pp. 678-681, 2012.
- [87] H. A. Wheeler, "Fundamental Limitations of Small Antennas," *Proceedings of the IRE*, vol. 35, no. 12, pp. 1479-1484, 1947.
- [88] C. Pfeiffer, A. Grbic, X. Xin, and S. R. Forrest, "Novel methods to analyze and fabricate electrically small antennas," in *Antennas and Propagation (APSURSI), 2011 IEEE International Symposium on*, 2011, pp. 761-764.
- [89] W. G. Whittow *et al.*, "Inkjet-Printed Microstrip Patch Antennas Realized on Textile for Wearable Applications," *IEEE Antennas and Wireless Propagation Letters*, vol. 13, pp. 71-74, 2014.
- [90] J. D. Kraus, "The Helical Antenna," *Proceedings of the IRE*, vol. 37, no. 3, pp. 263-272, 1949.
- [91] A. Vander Vorst, A. Rosen, and Y. Kotsuka, *RF / Microwave Interaction with Biological Tissues*. Wiley, 2006.
- [92] C. Gabriel, S. Gabriel, and E. Corthout, "The dielectric properties of biological tissues: I. Literature survey," (in eng), *Phys Med Biol*, vol. 41, no. 11, pp. 2231-49, Nov 1996.
- [93] S. Gabriel, R. W. Lau, and C. Gabriel, "The dielectric properties of biological tissues: II. Measurements in the frequency range 10 Hz to 20 GHz," (in eng), *Phys Med Biol*, vol. 41, no. 11, pp. 2251-69, Nov 1996.
- [94] S. Gabriel, R. W. Lau, and C. Gabriel, "The dielectric properties of biological tissues: III. Parametric models for the dielectric spectrum of tissues," (in eng), *Phys Med Biol*, vol. 41, no. 11, pp. 2271-93, Nov 1996.
- [95] Y. Feldman, A. Puzenko, and Y. Ryabov, "Dielectric Relaxation Phenomena in Complex Materials," 2006.
- [96] A. Kiourti and K. S. Nikita, "A Review of Implantable Patch Antennas for Biomedical Telemetry: Challenges and Solutions [Wireless Corner]," *Antennas and Propagation Magazine, IEEE*, vol. 54, no. 3, pp. 210-228, 2012.
- [97] G. C. R. Melia, *Electromagnetic Absorption by the Human Body from 1-15 GHz*. University of York, 2013.
- [98] E. A. Kaur, E. H. Malik, E. V. Tanwar, and D. V. K. Lamba, "Effect of Permittivity and Conductivity of Tissue on Specific Absorption Rate of Electromagnetic Radiations," *International Journal of Innovative Technology and Exploring Engineering*, 2012.
- [99] D. M. Pozar, *Microwave engineering*, 2nd ed. Wiley, 1998.
- [100] R. Alrawashdeh, "Implantable Antennas for Biomedical Applications," PhD, University of Liverpool, 2015.
- [101] K. Jaehoon and Y. Rahmat-Samii, "Implanted antennas inside a human body: simulations, designs, and characterizations," *IEEE Transactions on Microwave Theory and Techniques*, vol. 52, no. 8, pp. 1934-1943, 2004.

- [102] R. W. P. King and G. S. Smith, *Antennas in matter : fundamentals, theory and applications*. MIT Press, 1981.
- [103] S. M. Mikki and Y. M. M. Antar, "A Theory of Antenna Electromagnetic Near Field—Part I," *Antennas and Propagation, IEEE Transactions on*, vol. 59, no. 12, pp. 4691-4705, 2011.
- [104] S. M. Mikki and Y. M. M. Antar, "A Theory of Antenna Electromagnetic Near Field—Part II," *Antennas and Propagation, IEEE Transactions on*, vol. 59, no. 12, pp. 4706-4724, 2011.
- [105] Y. El-Saboni, M. K. Magill, G. A. Conway, and W. G. Scanlon, "Assessing the RF Performance of Medical Implant Antennas," 2016.
- [106] M. K. Magill, G. Conway, and W. Scanlon, "Tissue-Independent Implantable Antenna for In-Body Communications at 2.36 - 2.5 GHz," *IEEE Transactions on Antennas and Propagation*, vol. PP, no. 99, pp. 1-1, 2017.
- [107] F. Merli, B. Fuchs, J. R. Mosig, and A. K. Skrivervik, "The Effect of Insulating Layers on the Performance of Implanted Antennas," *Antennas and Propagation, IEEE Transactions on*, vol. 59, no. 1, pp. 21-31, 2011.
- [108] A. Christ, M. Douglas, J. Nadakuduti, and N. Kuster, "Assessing Human Exposure to Electromagnetic Fields From Wireless Power Transmission Systems," *Proceedings of the IEEE*, vol. 101, no. 6, pp. 1482-1493, 2013.
- [109] J. S. Seybold. Introduction to RF Propagation [Online]. Available: ISBN 978-0-471-65596-1
- [110] T. Chrysikos, I. Zisi, and S. Kotsopoulos, "Channel modeling and path loss characterization for in-body propagation at MICS and ISM bands," in *2016 Wireless Telecommunications Symposium (WTS)*, 2016, pp. 1-7.
- [111] R. K. Moore, "Effects of a surrounding conducting medium on antenna analysis," *Antennas and Propagation, IEEE Transactions on*, vol. 11, no. 3, pp. 216-225, 1963.
- [112] M. R. Basar *et al.*, "The use of a human body model to determine the variation of path losses in the human body channel in wireless capsule endoscopy," *Progress in Electromagnetics Research*, Article vol. 133, pp. 495-513, 2013 2013.
- [113] E. Topsakal, "Antennas for medical applications: Ongoing research and future challenges," in *Electromagnetics in Advanced Applications, 2009. ICEAA '09. International Conference on*, 2009, pp. 890-893.
- [114] W. Wei and F. Qiang, "Design and simulation of printed spiral coil used in wireless power transmission systems for implant medical devices," in *Engineering in Medicine and Biology Society, EMBC, 2011 Annual International Conference of the IEEE*, 2011, pp. 4018-4021.
- [115] N. Kuster and Q. Balzano, "Energy absorption mechanism by biological bodies in the near field of dipole antennas above 300 MHz," *Vehicular Technology, IEEE Transactions on*, vol. 41, no. 1, pp. 17-23, 1992.
- [116] "IEEE Standard for Safety Levels with Respect to Human Exposure to Radio Frequency Electromagnetic Fields, 3 kHz to 300 GHz," *IEEE Std C95.1, 1999 Edition*, pp. 1-83, 1999.
- [117] P. R. Wainwright, "The relationship of temperature rise to specific absorption rate and current in the human leg for exposure to electromagnetic radiation in the high frequency band," *Physics in Medicine & Biology*, vol. 48, no. 19, p. 3143, 2003.
- [118] "IEEE Standard for Safety Levels With Respect to Human Exposure to Radio Frequency Electromagnetic Fields, 3 kHz to 300 GHz," *IEEE Std C95.1-1991*, p. 1, 1992.

- [119] U. S. N. C. o. R. Protection and Measurements, "Biological Effects and Exposure Criteria for Radiofrequency Electromagnetic Fields," 1986: National Council on Radiation Protection and Measurements.
- [120] H. Wheeler, "Fundamental limitaions of a small VLF antenna for submarines," *IRE Transactions on Antennas and Propagation*, vol. 6, no. 1, pp. 123-125, 1958.
- [121] D. Kurup, W. Joseph, G. Vermeeren, and L. Martens, "In-body Path Loss Model for Homogeneous Human Tissues," *IEEE Transactions on Electromagnetic Compatibility*, vol. 54, no. 3, pp. 556-564, 2012.
- [122] J. Uei-Ming and M. Ghovanloo, "Design and Optimization of Printed Spiral Coils for Efficient Transcutaneous Inductive Power Transmission," *Biomedical Circuits and Systems, IEEE Transactions on*, vol. 1, no. 3, pp. 193-202, 2007.
- [123] J. Uei-Ming and M. Ghovanloo, "Modeling and Optimization of Printed Spiral Coils in Air, Saline, and Muscle Tissue Environments," *Biomedical Circuits and Systems, IEEE Transactions on*, vol. 3, no. 5, pp. 339-347, 2009.
- [124] L. J. Chu, "Physical Limitations of Omni-Directional Antennas," *Journal of Applied Physics*, vol. 19, no. 12, pp. 1163-1175, 1948.
- [125] J. S. McLean, "A re-examination of the fundamental limits on the radiation Q of electrically small antennas," *Antennas and Propagation, IEEE Transactions on*, vol. 44, no. 5, p. 672, 1996.
- [126] H. A. Wheeler, "Useful radiation from an underground antenna," *J. Res. NBS*, vol. 65, pp. 89-91, 1961.
- [127] A. K. Skrivervik, J. F. Zurcher, O. Staub, and J. R. Mosig, "PCS antenna design: the challenge of miniaturization," *IEEE Antennas and Propagation Magazine*, vol. 43, no. 4, pp. 12-27, 2001.
- [128] F. Merli and A. K. Skrivervik, "Design and measurement considerations for implantable antennas for telemetry applications," in *Proceedings of the Fourth European Conference on Antennas and Propagation*, 2010, pp. 1-5.
- [129] T. Onishi *et al.*, "Biological tissue-equivalent agar-based solid phantoms and SAR estimation using the thermographic method in the range of 3-6 GHz," (in English), *Ieice Transactions on Communications*, Article vol. E88B, no. 9, pp. 3733-3741, Sep 2005.
- [130] J. Faerber, G. Cummins, and M. P. Y. Desmulliez, "Design of conformai wideband antennas for capsule endoscopy within a body tissue environment," in *2016 46th European Microwave Conference (EuMC)*, 2016, pp. 1223-1226.
- [131] W. Whittow, "Specific absorption rate perturbations in the eyes and head by metallic spectacles at personal radio communication frequencies," University of Sheffield, 2004.
- [132] J. Keshvari, R. Keshvari, and S. Lang, "The effect of increase in dielectric values on specific absorption rate (SAR) in eye and head tissues following 900, 1800 and 2450 MHz radio frequency (RF) exposure," (in eng), *Phys Med Biol*, vol. 51, no. 6, pp. 1463-77, Mar 21 2006.
- [133] K. Shiba and N. Higaki, "Analysis of SAR and Current Density in Human Tissue Surrounding an Energy Transmitting Coil for a Wireless Capsule Endoscope," in *2009 20th International Zurich Symposium on Electromagnetic Compatibility*, 2009, pp. 321-324.
- [134] F. Soler, "Radiation effects of wearable antenna in human body tissues," Master Master thesis, University of Colorado Springs, Escola Tècnica Superior d'Enginyeria de Telecomunicació de Barcelona - Enginyeria Electrònica, 2014.

- [135] K. Ito, "Human Body Phantoms for Evaluation of Wearable and Implantable Antennas," in *The Second European Conference on Antennas and Propagation, EuCAP 2007*, 2007, pp. 1-6.
- [136] I. I. Foundation. (16/06/). *Human body models*.
- [137] R. Jegadeesan, G. Yong Xin, and J. Minkyu, "Electric near-field coupling for wireless power transfer in biomedical applications," in *Microwave Workshop Series on RF and Wireless Technologies for Biomedical and Healthcare Applications (IMWS-BIO), 2013 IEEE MTT-S International*, 2013, pp. 1-3.
- [138] D. Nikolayev, M. Zhadobov, P. Karban, and R. Sauleau, "Increasing the radiation efficiency and matching stability of in-body capsule antennas," in *2016 10th European Conference on Antennas and Propagation (EuCAP)*, 2016, pp. 1-5.
- [139] T. Dissanayake, K. P. Esselle, and M. R. Yuce, "Dielectric Loaded Impedance Matching for Wideband Implanted Antennas," *Microwave Theory and Techniques, IEEE Transactions on*, vol. 57, no. 10, pp. 2480-2487, 2009.
- [140] S. Symeonidis, W. G. Whittow, and C. Panagamuwa, "Characterisation of an antenna system implanted into a limb phantom for monitoring of bone fracture healing," in *2016 Loughborough Antennas & Propagation Conference (LAPC)*, 2016, pp. 1-4.
- [141] N. Vidal, A. Garcia-Miquel, J. M. Lopez-Villegas, J. J. Sieiro, and F. M. Ramos, "Influence of phantom models on implantable antenna performance for biomedical applications," in *Antennas and Propagation (EuCAP), 2015 9th European Conference on*, 2015, pp. 1-4.
- [142] S. Nishizawa and O. Hashimoto, "Effectiveness analysis of lossy dielectric shields for a three-layered human model," *IEEE Transactions on Microwave Theory and Techniques*, vol. 47, no. 3, pp. 277-283, 1999.
- [143] J. Gemio, J. Parron, and J. Soler, "Human body effects on implantable antennas for ISM bands applications: Models comparison and propagation losses study," *Progress In Electromagnetics Research*, vol. 110, pp. 437-452, 2010.
- [144] P. Soontornpipit, C. M. Furse, and C. You Chung, "Design of implantable microstrip antenna for communication with medical implants," *Microwave Theory and Techniques, IEEE Transactions on*, vol. 52, no. 8, pp. 1944-1951, 2004.
- [145] M. Je *et al.*, "Wireless sensor microsystems for emerging biomedical applications (Invited)," in *2015 IEEE International Symposium on Radio-Frequency Integration Technology (RFIT)*, 2015, pp. 139-141.
- [146] A. P. Gregory and R. N. Clarke, "Dielectric metrology with coaxial sensors," *Measurement Science and Technology*, vol. 18, no. 5, p. 1372, 2007.
- [147] T. Castel *et al.*, "Improved Reception of In-Body Signals by Means of a Wearable Multi-Antenna System," *International Journal of Antennas and Propagation*, vol. 2013, p. 9, 2013, Art. no. 328375.
- [148] L. D. Blake. (2017). *Tuning Your Antenna*. Available: <http://hamuniverse.com/testingswr.html>
- [149] X. Lisheng, M. Q. H. Meng, C. Yawen, H. Chao, and W. Haibin, "Influence of animal body on ingested wireless device before and after death," in *2008 IEEE/ASME International Conference on Advanced Intelligent Mechatronics*, 2008, pp. 176-181.
- [150] M. Beccani, E. Susilo, C. Di Natali, and P. Valdastri, "SMAC - A Modular Open Source Architecture for Medical Capsule Robots," (in English), *International Journal of Advanced Robotic Systems*, Article vol. 11, p. 16, Nov 2014, Art. no. 188.

- [151] T. S. Kim, S. Y. Song, H. Jung, J. Kim, and E. S. Yoon, "Micro Capsule Endoscope for Gastro Intestinal Tract," in *2007 29th Annual International Conference of the IEEE Engineering in Medicine and Biology Society*, 2007, pp. 2823-2826.
- [152] T. Instruments, "CC1310 SimpleLink™ Ultralow Power Sub-1-GHz Wireless MCU," in *SWRS181B datasheet*, ed, Sept. 2015 [revised Oct. 2016].
- [153] U. D. o. Health and H. Services, "Toxicological profile for ammonia," *Public Health Service, Agency for Toxic Substances and Disease Registry (ATSDR)*, editor, 2004.
- [154] J. Faerber *et al.*, "In Vivo Characterization of a Wireless Telemetry Module for a Capsule Endoscopy System Utilizing a Conformal Antenna," *IEEE Transactions on Biomedical Circuits and Systems*, vol. PP, no. 99, pp. 1-11, 2017.
- [155] W. Lei *et al.*, "A programmable microsystem using system-on-chip for real-time biotelemetry," *IEEE Transactions on Biomedical Engineering*, vol. 52, no. 7, pp. 1251-1260, 2005.
- [156] S. Kim *et al.*, "Evaluation of a 433 MHz band body sensor network for biomedical applications," (in eng), *Sensors (Basel)*, vol. 13, no. 1, pp. 898-917, Jan 14 2013.
- [157] K. M. S. Thotahewa, J. M. Redoute, and M. R. Yuce, "A UWB wireless capsule endoscopy device," in *Engineering in Medicine and Biology Society (EMBC), 2014 36th Annual International Conference of the IEEE*, 2014, pp. 6977-6980.
- [158] P. Zakavi, N. C. Karmakar, and I. Griggs, "Wireless Orthopedic Pin for Bone Healing and Growth: Antenna Development," *IEEE Transactions on Antennas and Propagation*, vol. 58, no. 12, pp. 4069-4074, 2010.
- [159] H. Rajagopalan and Y. Rahmat-Samii, "Wireless Medical Telemetry Characterization for Ingestible Capsule Antenna Designs," *Antennas and Wireless Propagation Letters, IEEE*, vol. 11, pp. 1679-1682, 2012.
- [160] M. Rezapour, C. Amadi, and L. B. Gerson, "Retention associated with video capsule endoscopy: systematic review and meta-analysis," (in eng), *Gastrointest Endosc*, vol. 85, no. 6, pp. 1157-1168.e2, Jun 2017.
- [161] J. Marques Hueso *et al.*, "A rapid photopatterning method for selective plating of 2D and 3D micro-circuitry on polyetherimide," 2017.
- [162] D. E. Watson, J. H.-G. Ng, K. E. Aasmundtveit, and M. P. Desmulliez, "In-situ silver nanoparticle formation on surface-modified polyetherimide films," *IEEE Transactions on Nanotechnology*, vol. 13, no. 4, pp. 736-742, 2014.